Lawrence Berkeley National Laboratory

Title
Science Impacts of the SPHEREx All-Sky Optical to Near-Infrared Spectral Survey: Report of a Community Workshop Examining Extragalactic, Galactic, Stellar and Planetary Science

Permalink
https://escholarship.org/uc/item/6t24x5h2

Authors
Doré, Olivier
Werner, Michael W
Ashby, Matt
et al.

Publication Date
2016-06-22

Peer reviewed

Science Impacts of the SPHEREx All-Sky Optical to Near-Infrared Spectral Survey:

Report of a Community Workshop Examining Extragalactic, Galactic, Stellar and Planetary Science

Olivier Doré[1,21], Michael W. Werner[1,21], Matt Ashby[26], Pancha Banerjee[23], Nick Battaglia[16], James Bauer[1], Robert A. Benjamin[34], Lindsey E. Bleem[36,37], Jamie Bock[21], Adwin Boogert[2], Philip Bull[1,21], Peter Capak[8], Tzu-Ching Chang[3], Jean Chiar[38], Seth H. Cohen[30], Asantha Cooray[28], Brendan Crill[1,21], Michael Cushing[4], Roland de Putter[21], Simon P. Driver[32], Tim Eifler[21], Chang Feng[28], Simone Ferraro[19], Douglas Finkbeiner[31], B. Scott Gaudi[18], Tom Greene[5], Lynne Hillenbrand[21], Peter A. Höflich[6], Eric Hsiao[6], Kevin Huffenberger[6], Rolf A. Jansen[30], Woong-Seob Jeong[7], Bhavin Joshi[30], Duho Kim[30], Minjin Kim[7], J.Davy Kirkpatrick[8], Phil Korngut[21], Elisabeth Krause[9], Mariska Kriek[25], Boris Leistedt[10], Aigen Li[40], Carey M. Lisse[11], Phil Mauskopf[30], Matt Mechtley[30], Gary Melnick[26], Joseph Mohr[35,41], Jeremiah Murphy[6], Abraham Neben[13], David Neufeld[24], Hien Nguyen[1,21], Elena Pierpaoli[23], Jeonghyun Pyo[7], Jason Rhodes[1,21], Karin Sandstrom[15], Emmanuel Schaan[16], Kevin C. Schlaufman[22], John Silverman[12], Kate Su[33], Keivan Stassun[17], Daniel Stevens[18], Michael A. Strauss[16], Xander Tielens[39], Chao-Wei Tsai[20], Volker Tolls[26], Stephen Unwin[1], Marco Viero[9], Rogier A. Windhorst[30], Michael Zemcov[27,1]

Editors and corresponding authors: Olivier Doré[1,21], Michael Werner[1,21] (olivier.dore@caltech.edu, michael.w.werner@jpl.nasa.gov)

[1]Jet Propulsion Laboratory, 4800 Oak Grove Drive, Pasadena, CA 91109, USA

[2]Universities Space Research Association, Stratospheric Observatory for Infrared Astronomy, NASA Ames Research Center, MS 232-11, Moffett Field, CA 94035, USA

[3]ASIAA, AS/NTU, 1 Roosevelt Rd Sec 4, Taipei, 10617, Taiwan

[4]Department of Physics and Astronomy, University of Toledo, 2801 W. Bancroft St., Toledo, OH 43606, USA

[5]NASA Ames Research Center, MS 245-6, Moffett Field, CA 94035, USA

[6]Department of Physics, Florida State University, PO Box 3064350, Tallahassee, Florida 32306-4350, USA

[7]Korea Astronomy and Space Science Institute, Daejeon, 34055, Korea

[8]IPAC, Caltech, 770 S. Wilson Ave, Pasadena, CA 91125, USA

[9]Kavli Institute for Particle Astrophysics & Cosmology, P. O. Box 2450, Stanford University, Stanford, CA 94305, USA

[10]Center for Cosmology and Particle Physics, Department of Physics, New York University, New York, NY 10003, USA

[11]JHU-APL, SES/SRE, Bldg 200/E206, 11100 Johns Hopkins Road, Laurel, MD 20723, USA

[12]Kavli Institute for the Physics and Mathematics of the Universe (Kavli IPMU),The University of Tokyo, 5-1-5 Kashiwanoha Kashiwa, 277-8583, Japan

[13]Massachusetts Institute of Technology, Department of Physics, 70 Vassar Street, Bldg. 37-656, Cambridge, MA 02139, USA

[14]Dept. of Physics and Astronomy, Johns Hopkins University, 3400 N. Charles St., Baltimore, MD 21218, USA

[15]University of California, 9500 Gilman Drive, San Diego, La Jolla, CA 92093, USA

[16]Department of Astrophysical Sciences, Peyton Hall, Princeton University, Princeton, NJ 08544, USA

[17]Physics & Astronomy Department, Vanderbilt University, Nashville, TN 37235, USA

[18]Department of Astronomy, The Ohio State University, 140 W. 18th Avenue, Columbus, OH 43210 USA

[19]Berkeley Center for Cosmological Physics and Department of Astronomy, University of California, Berkeley, CA 94720, USA

[20]Department of Physics and Astronomy, UCLA, Los Angeles, CA 90095-1547, USA

[21]California Institute of Technology, 1200 E. California Blvd, Pasadena, CA 91125, USA

[22]Observatories of the Carnegie Institution for Science, 813 Santa Barbara St., Pasadena, CA 91101

[23]Department of Physics and Astronomy, University of Southern California, 3620 McClintock Avenue, Los Angeles, CA 90089, USA

[24]Dept. of Physics and Astronomy, Johns Hopkins University, 3400 N. Charles St., Baltimore, MD 21218, USA

[25]Department of Astronomy, University of California, Berkeley, CA 94720, USA

[26] Harvard Smithsonian CfA, 60 Garden St., Cambridge, MA 02138, USA

[27] Rochester Institute of Technology, College of Science, 74 Lomb Memorial Drive, Rochester, NY 14623, USA

[28]University of California Irvine, 4186 Frederick Reines Hall, Irvine, CA 92697, USA

[30]Arizona State University, Department of Physics, P.O. Box 871504, Tempe, AZ 85287, USA

[31] Harvard-Smithsonian, Center for Astrophysics, 60 Garden St. Cambridge, MA 02138, USA

[32] ICRAR M468, The University of Western Australia, 35 Stirling Hwy, Crawley, Western Australia, 6009, Australia

[33] Steward Observatory, University of Arizona, Tucson, AZ 85721, USA

[34] University of Wisconsin - Whitewater, Whitewater, WI 53190, USA

[35] Faculty of Physics, Ludwig-Maximilians-Universitaet, Scheinerstrasse 1, 81679 Munich, Germany

[36] Argonne National Laboratory, High-Energy Physics Division, 9700 S. Cass Avenue, Argonne, IL 60439, USA

[37] Kavli Institute for Cosmological Physics, University of Chicago, 5640 South Ellis Avenue, Chicago, IL 60637, USA

[38] SETI Institute, Carl Sagan Center, 189 Bernardo Avenue, Mountain View, CA 94043, USA

[39] Leiden Observatory, Leiden University, PO Box 9513, NL-2300RA Leiden, The Netherlands

[40] Department of Physics and Astronomy, University of Missouri, Columbia, MO 65211, USA

[41] Max Planck Institute for Extraterrestrial Physics, Giessenbachstrasse 1, 85478 Garching, Germany

Abstract. SPHEREx, the Spectro-Photometer for the History of the Universe, Epoch of Reionization, and Ices Explorer, is a proposed SMEX mission selected for Phase A study pointing to a

downselect in early CY2017, leading to launch in CY2021. SPHEREx will carry out the first all-sky spectral survey at wavelengths between 0.75 and 4.18 μm [with spectral resolution R$\sim$41.4] and 4.18 and 5.00 μm [with R$\sim$135]. At the end of its two year mission, SPHEREx will provide 0.75-to-5.00 μm spectra of every 6.2$\times$6.2 arcsec pixel on the sky. SPHEREx will easily obtain spectra with S/N > 50 per frequency element of all sources in the 2MASS catalog and spectra with S/N >5 per frequency element of the faintest sources detected by WISE in its short wavelength channels at 3.4 and 4.8 μm. More details concerning SPHEREx are available at http://spherex.caltech.edu. The SPHEREx team has proposed three specific science investigations to be carried out with this unique data set: cosmic inflation, interstellar and circumstellar ices, and the extra-galactic background light.

It is readily apparent, however, that many other questions in both astrophysics and planetary sciences could be addressed with the SPHEREx data. The SPHEREx team convened a community workshop in February 2016, with the intent of enlisting the aid of a larger group of scientists in defining these questions, and this paper summarizes the results of that workshop http://spherex.caltech.edu/Workshop.html. A rich and varied menu of investigations was laid out, including studies of the composition of main belt and Trojan/Greek asteroids; mapping the zodiacal light with higher spatial and spectral resolution than has been done previously; identifying and studying very low-metallicity stars; improving stellar parameters in order to better characterize transiting exoplanets; studying aliphatic and aromatic carbon-bearing molecules in the interstellar medium; mapping star formation rates in nearby galaxies; determining the redshift of clusters of galaxies; identifying high redshift quasars over the full sky; and providing a NIR spectrum for all eROSITA X-ray sources. All of these investigations, and others not listed here, can be carried out with the all-sky spectra to be produced by SPHEREx; none of them imposes any additional observational requirements or operating modes. In addition, the workshop defined enhanced data products and user tools which would facilitate some of these scientific studies. Finally, the workshop noted the high degrees of synergy between SPHEREx and a number of other current or forthcoming programs, including JWST, WFIRST, Euclid, GAIA, K2/Kepler, TESS, eROSITA and LSST.

# Contents

1 SPHEREx and the Decade of the Surveys

SPHEREx, the Spectro-Photometer for the History of the Universe, Epoch of Reionization, and Ices Explorer is a proposed SMEX mission selected for Phase A study pointing to a downselect in early CY2017, leading to launch in CY2020. The Principal Investigator is Professor Jamie Bock of Caltech. SPHEREx will carry out the first all-sky spectral survey at wavelengths between 0.75 and 4.18 μm [with spectral resolution R$\sim$41.4] and 4.18 and 5.00 μm [with R$\sim$135]. At the end of its two year mission, SPHEREx will obtain 0.75-to-5μm spectra of every 6.2$\times$6.2 arcsec pixel on the sky, with a 5-sigma sensitivity AB$\simeq$18-19 per spectral/spatial resolution element (see Fig. 1). SPHEREx thus will easily obtain spectra with S/N $>$ 50 per frequency element of all sources in the 2MASS catalog and spectra with S/N $>$ 5 of the faintest sources detected by WISE in its short wavelength channels at 3.4 and 4.8 μm. Such a rich archival spectral database will support numerous scientific investigations (e.g., Table 1) of great interest to the wider scientific community. We outline below a few examples.

The SPHEREx mission and its core science objectives are described in detail on this website http://spherex.caltech.edu and in [1]. The proposing team defined three high priority science investigations on which to focus its efforts, which in turn relate to the three major astrophysics themes of the NASA Science Plan:

1. Test models of inflation by mapping the 3D distribution of galaxies to measure primordial non-Gaussianity, to probe the running of the primordial power spectrum spectral index, and to search for departures from geometric flatness [NASA Science Plan Theme: Probe the origin and destiny of the universe]; and

2. Investigate the connection between ices in interstellar clouds, in planet-forming disks, and in our own Solar System [NASA Science Plan Theme: Explore whether planets around other stars could harbor life]; and

3. Determine the origin of the large-scale cosmic infrared background fluctuations, and constrain the history of its production [NASA Science Plan Theme: Explore the origin and evolution of galaxies].

As important as these three investigations are, they represent only a fraction of the science which would be enabled by SPHEREx' unique all-sky spectroscopic data base as illustrated in Table 1 extracted from [1]. From 24 to 26 February 2016, the SPHEREx team convened a workshop held at the Keck Center on the Caltech campus. Experts in a wide range of astrophysical and planetary science disciplines attended to discuss other scientific areas in which the SPHEREx data would have a great impact, and to define software tools and ancillary data sets which would enable the exploitation of the data in order to address these other questions. Agenda and presentations can be found here http://spherex.caltech.edu/Workshop.html. This white paper, based in large part on contributions from workshop participants, describes how the SPHEREx data could be used to advance our understanding of key questions in more than a dozen areas identified during the workshop. Many of these ideas will be presented as part of a Science Enhancement Option (SEO) to be included in the SPHEREx study report which will be evaluated by NASA in the process of selecting a mission for flight. In addition, the white paper addresses the synergyism between SPHEREx and other current and future NASA and ground-based programs.

During the workshop, Michael Strauss of Princeton referred to the 2020s as the decade of the surveys. He had in mind such programs as WFIRST, Euclid, and LSST, each of which will survey large areas of the sky and produce rich data sets which are synergistic with SPHEREx, as discussed further below.
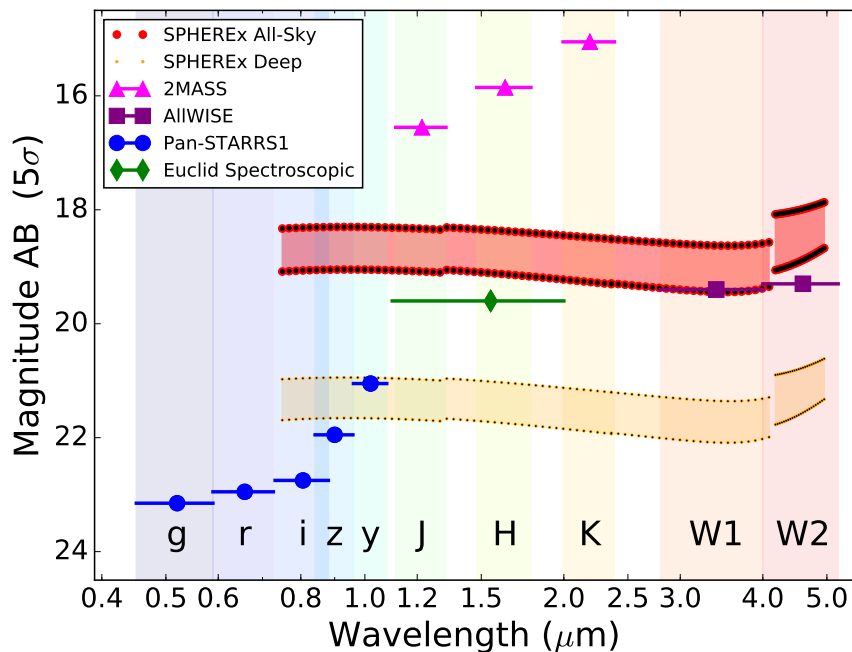
Figure 1. Sensitivity of SPHEREx and current surveys (all at 5σ). The SPHEREX sensitivity is quoted for each $\lambda/\Delta\lambda = 41.4$ spectral channel for $0.75 < z < 4.18$ μm and in each $\lambda/\Delta\lambda = 135$ spectral channel for $4.18 < z < 5.0$ μm. The bottom red curve corresponds to the current best estimate sensitivity over the whole sky while the top curve corresponds to the instrument sensitivity based on specifications that each sub-system can meet with contingency over the whole sky. The orange dots correspond to the analogous sensitivity curves over the deep regions. The statistical sensitivity does not include the effects of astrophysical source confusion, which is significant at the deep survey depth.

SPHEREx would be the latest in a series of all-sky surveys to be carried out under NASA's Explorer program; previous surveys include IRAS, COBE, WMAP, GALEX, and WISE. 2MASS is an additional important survey, not carried out from space but supported in part by NASA funds. SPHEREx, based on its orbit and wavelength coverage, might be thought of as a spectroscopic version of WISE or 2MASS. Like those missions, SPHEREx will produce a treasure trove of well-characterized, uniformly calibrated data which will be used by the scientific community for years to come. In addition, based on its exploration of a previously unexplored region of scientific phase space, SPHEREx, like the predecessor surveys, has the potential to discover new and exciting phenomena as it extends our understanding of the astronomical Universe.

Object	# Sources	Legacy Science	Reference

Detected galaxies	1.4 billion	Properties of distant and heavily obscured galaxies	Simulation based on COSMOS and Pan-STARRS
Galaxies with $\sigma(z)/(1+z) < 0.1$	301 million	Study large scale clustering of galaxies	Simulation based on COSMOS and Pan-STARRS
Galaxies with $\sigma(z)/(1+z) < 0.03$	120 million	Study (Hα, Hβ, CO, OII, OIII, SII, H$_2$O) line and PAH emission by galaxy type. Explore galaxy and AGN life cycle	Simulation based on COSMOS and Pan-STARRS
Galaxies with $\sigma(z)/(1+z) < 0.003$	9.8 million	Cross check of Euclid photo-z. Measure dynamics of groups and map filaments. Cosmological galaxy clustering, BAO, RSD.	Simulation based on COSMOS and Pan-STARRS
QSOs	> 1.5 million	Understand QSO lifecycle, environment, and taxonomy	[2] plus simulations
QSOs at $z > 7$	1-300	Determine if early QSOs exist. Follow-up spectroscopy probes EOR through Lyα forest	[2] plus simulations
Clusters with ≥ 5 members	25,000	Redshifts for all eRosita clusters. Viral masses and merger dynamics	[3]
Main sequence stars	> 100 million	Fundamental parameters (mass, radius and effective temperature) of a large sample of stars. Test the uniformity of the Galactic stellar mass function as input to extragalactic studies	2MASS catalogs
Mass-losing, dust forming stars	Over 10,000 of all types	Spectra of M supergiants, OH/IR stars, Carbon stars. Stellar atmospheres, dust return rates, and composition of dust	Astrophysical Quantities, 4th edition [ed. A.Cox] p. 527
Brown dwarfs	>400, incl. >40 of types T and Y	Atmospheric structure and composition; search for hazes. Informs studies of giant exoplanets	dwarfarchives.org and J.D. Kirkpatrick, priv. comm.
Stars with hot dust	>1000	Discover rare dust clouds produced by cataclysmic events like the collision which produced the Earths moon	Kennedy & Wyatt (2013)

Young Stars with Accretion Disks	Over 20,000 of all types	Probe strong accretion/outflow signatures, star/disk atmospheres, extinction	C2D and related 2MASS+Spitzer/WISE surveys
Diffuse ISM	Map of the Galactic plane	Study diffuse emission from interstellar clouds and nebulae; hydro-carbon emission in the 3μm region	GLIMPSE survey (Churchwell et al. 2009)

Table 1: SPHEREx spectral database populations (extract from [1]).

2   Extra-galactic Science

2.1   Mapping Star Formation Rates in Nearby Galaxies

Star formation is one of the fundamental drivers of galaxy evolution. Mapping the distribution of the current star formation rate (SFR) in galaxies is central to many observational studies, however it is subject to major systematic uncertainties. Two of the key systematic uncertainties are 1) the timescale over which a tracer is produced (i.e. hydrogen recombination lines have timescales < 10 Myr while far-UV emission has timescales of ~ 100 Myr) and 2) how to correct for extinction. The latter issue has been the major impetus for "hybrid" star formation rate tracers which combine Hα or far-UV with mid-IR dust emission, representing the obscured portion of the SF [4]. The "hybrid" tracers are typically calibrated with near-IR hydrogen recombination line emission such as Paschen-α, since it is mostly insensitive to extinction and dominated by recent < 10Myr star formation. Unfortunately, the inclusion of mid-IR emission into these tracers opens up a host of additional issues related to how much of the IR emission is powered by star formation rather than the radiation field generated by older stars [a.k.a. the "cirrus" correction 5–9].

SPHEREx observations will allow a major step forward in studying star formation in nearby galaxies by making 6 arcsec maps of the Paschen-α and Brackett-α lines over the entire sky. The sensitivity of the line observations is well matched to cover the main star forming area of nearby galaxies, detecting the near-IR recombination lines in most regions where molecular gas dominates the ISM gas content. In addition, the stellar continuum observed by SPHEREx will provide a gold standard stellar mass map, avoiding issues with contamination by hot dust and PAH emission at 3.3 μm [10, 11]. Combining this information, SPHEREx will provide resolved maps of the specific star formation rate in the full local galaxy population, giving the definitive account of where $z = 0$ galaxies are forming stars. SPHEREx observations of near-IR hydrogen recombination lines will also be the premier dataset for calibrating other SFR tracers for use in samples of more distant galaxies.

2.2   Star-Forming and Early-Type Galaxies with SPHEREx at z$\lesssim$0.5

Fig. 2 left shows the rest-frame (U–B) color vs. stellar mass for all galaxies to AB$\lesssim$25 mag from the HST ACS "PEARS" grism survey [12]. The galaxy stellar mass estimates and spectroscopic redshifts ($0.6\lesssim$z$\lesssim$1.2) come from 3D-HST [13], and were analyzed in a 5×5 color-mass grid as described in Joshi et al.2016 (in preparation). The large "blue cloud" and the much smaller "red cloud", as well

as the "green valley" in between are visible, and each are sampled by several grid boxes. Fig. 2 right shows the clipped-average rest-frame spectra for each of the $(U–B)_{rest}$ color and stellar mass bins in Fig. 2 left. Some of the low-mass star-forming (blue-cloud) galaxies show a Balmer 3648 Å break and a weak $H\beta$ 4861 + O III 5007 line in their averaged grism spectra, while the more massive, early-type (red-cloud) galaxies show a clear 4000Å break and Mg 5175Å in absorption (for details, see Joshi et al.2016, in preparation). HST PEARS has done this spectral averaging for ~1000 galaxies to AB≲25 mag at 0.6≲z≲1.2 in 40 arcmin^2. *SPHEREx will do this spectral averaging for $\gtrsim 10^8$ galaxies across the sky to AB≲19 mag to z≲0.5* (see Fig. 12 of [14] and Fig. 2 here). The spectral stacks from the SPHEREx 0.75–5.0 μm bands will cover restframe ~0.45-3.0 μm (see Fig. 25 and 4). That is, SPHEREx will study the average low-resolution spectra of millions of galaxies per bin in a very fine color-mass grid, tracing average spectral features like Mg 5175, Na 5895, the $H\alpha$ 6563 line (and for a higher-redshift subset also the $H\beta$ 4861 + O III 5007 line), the Calcium triplet (8500, 8544, 8665), and the near-IR break at 2.33 μm, all as a function of galaxy mass, color (*i.e.*, current SFR or SED age), metallicity, and dust extinction (A_V). Monte Carlo tests with accurate spectroscopic galaxy templates from SDSS, GAMA and WIGGLEz plus SED models [15] will be used to help calibrate the observed average absorption features in the SPHEREx data. With very careful attention to systematics (see the object confusion discussion in Sec. 6.1.1), the resulting average SPHEREx spectra, averaged over ~10^6 galaxies per color-mass bin will outline how galaxy mass assembly, gas accumulation (from emission lines, including those from SDSS, GAMA and WIGGLEz), metal build-up, and extinction build-up have taken place in the last 5 billion years.

2.3   The Galaxy Population at $z \sim 1$ with SPHEREx

Our understanding of the galaxy population at z~1 has grown tremendously in the past decade. Photometric surveys have constrained the overall mass growth, while spectroscopic surveys provided insights into the physical processes governing galaxy growth. However, both approaches have their limitations; while photometric surveys lack the spectroscopic information needed to derive redshifts and physical properties, spectroscopic surveys result in small and biased galaxy samples. To compromise between these two techniques, slitless low-resolution spectroscopic and photometric surveys at near-IR (e.g., rest-frame optical) wavelengths have become increasingly more popular (see e.g., PRIMUS [16], COSMOS [17], NMBS [18], SHARDS [19]). SPHEREx will build upon the success of such programs, and will provide a unique view to the galaxy population at $z \sim 1$.

While previous low-resolution surveys obtained deep spectra on relatively small fields, the power of SPHEREx is in its large area. Studies of individual galaxies will be limited to the brightest systems. Based on previous surveys, we estimate that in the SPHEREx-DEEP survey, spectral features will be detected for ~10,000 individual galaxies at $0.7 < z < 1.45$ per patch. These observations allow us to better constrain the massive end of the galaxy distribution at these redshifts.

However, much of the power of SPHEREx in studying $z \sim 1$ galaxies comes from stacking techniques. Deep optical photometry from LSST and other optical surveys will allow us to stack galaxies in bins of stellar mass or color-color space and accordingly study their infrared counterparts. The downside of such methods is that intrinsically different spectral types will be combined, and thus information will get lost.

To retain the diversity of the galaxy population at $z \sim 1$ and study galaxy properties during all possible evolutionary phases, more clever matching techniques should be applied. For example,
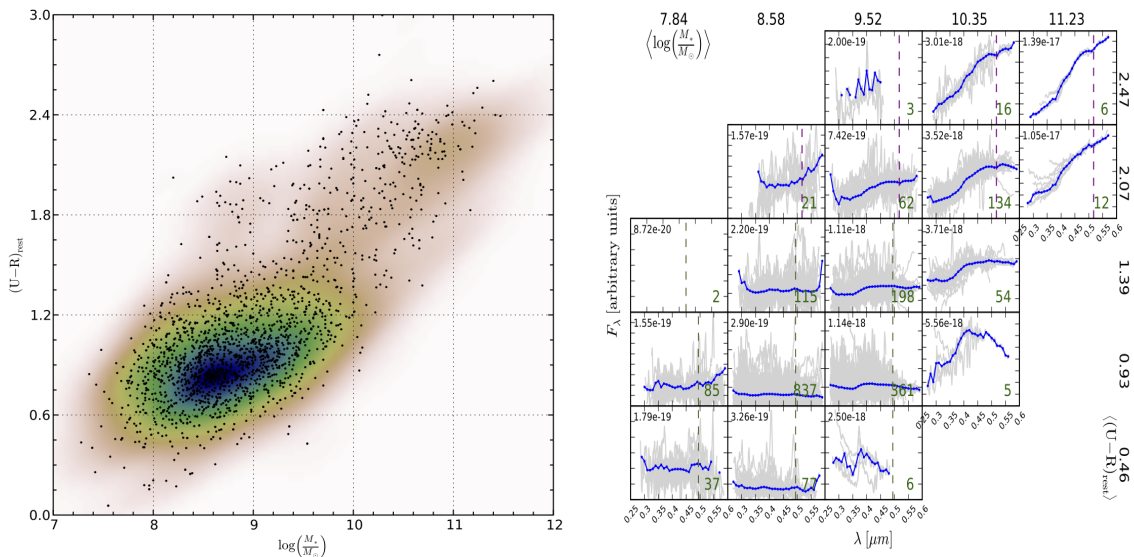
Figure 2. *Left:* Rest-frame $(U–B)_{rest}$ color vs. stellar mass $(M^* / M_\odot)$ for all galaxies to $AB \lesssim 25$ mag from the HST ACS "PEARS" G800L grism survey [12], as analyzed in a 5×5 color-mass grid by (Joshi et al. 2016, in preparation) which samples the "blue cloud", "green valley" and the narrower "red cloud". *Right:* Clipped-average rest-frame spectra for each of the $(U–B)_{rest}$ color and stellar mass bins $[\log(M_{stellar})]$ in the left panel. Green numbers indicate the number of similar rest-frame spectra averaged in each bin, the vertical green dashed line the location of the combined $H\beta\ 4861 + OIII\ 5007\text{Å}$ lines, and the vertical purple line the location of the Mg 5175 Å absorption feature. SPHEREx spectra averaged over $\sim 10^6$ galaxies per color-mass bin will outline how galaxy mass assembly, gas accumulation, metal build-up, and extinction build-up have taken place in the last 5 billion years.

by matching galaxies using their combined LSST-SPHEREx rest-frame spectral energy distributions (SEDs), we can group them by their full spectral type (see [20]). For each spectral type, we can stack the SEDs. This technique will enable the measurement of spectroscopic features which can not be measured for individual galaxies, such as rest-frame optical emission lines, metal absorption lines, or molecular bands.

This technique opens up a whole range of science applications. Most importantly, it will give a census of the star formation rate and ages for the complete galaxy population at z∼1. Furthermore, the wide wavelength coverage provides additional unique science cases. For example, for post-starburst galaxies it will allow us to constrain the thermally-pulsing asymptotic giant branch phase, and for star-forming galaxies we can access the rest-frame near-infrared emission lines. Finally, the width of the spectral features will provide a direct constraint on the accuracy of the used spectroscopic redshifts that are used.

2.4 Environmental Dependence of Galaxy Evolution

SPHEREx will independently identify tens of thousands of mostly low-redshift galaxy clusters spanning a large range of masses and about 75% of the sky (not at low galactic latitudes). These identifications will facilitate the study of galaxy properties such as stellar mass and galaxy spectral type (also measurable by SPHEREx) in the densest environments.

SPHEREx will also be able to reconstruct the galaxy density field even into low-density environments. High precision $(\sigma_z/(1 + z) < 0.005)$ spectroscopic redshifts can be used to measure projected densities with sufficient accuracy to rival spectroscopic surveys [21]. SPHEREx will measure redshifts at this precision or better for over 9 million galaxies. This represents a doubling of the SDSS spectroscopic sample over the SDSS footprint. Combining the two data sets will allow for high quality measurements of the density field [22–24]. This will allow the study of the joint galaxy mass and star formation rate functions as a function of environment for environments that span the range from clusters to filaments to very low density regions. These are key measurements for disentangling mass and environmental star formation quenching, and for making precise measurements of galaxy conformity, the relationship between the star formation occurring in central galaxies within a dark matter halo and their satellite galaxies [25].

In addition, the wavelength range covered by SPHEREx will include the Paschen-α line at 1.8 micron. Given a 5σ detection limit of 18.5 AB mag, SPHEREx will measure Paschen-α lines corresponding to star formation rates of about 10 M_{sun}/year at $z = 0.1$. This will allow the identification of the most extreme line emitters across the entire sky. Such galaxies are sometimes thought to be forming their first generation of stars, and are useful analogs for high redshift galaxies.

2.5 AGN Science

According to the unified theory of active galactic nuclei (AGN), the central part of AGN is composed of an accretion disk around a supermassive black hole (SMBH), a broad line region (BLR), and a dusty torus (Fig. 3). The accretion disk, the BLR, and the torus are the energy sources powering a UV/optical continuum (the big blue bump), broad emission lines (e.g., hydrogen recombination lines), and an IR continuum, respectively. To investigate the detailed structure of the central structure of AGNs it is crucial to better understand the various aspects of AGNs. Thanks to its wide wavelength coverage, SPHEREx will uniquely lead to a better understanding of the AGN structure and also of the coevolution of BHs and its host galaxies. SPHEREx will also provide a powerful data set for optical identification and follow-up of AGNs selected from other surveys.

2.5.1 IR and Optical Reverberation Mapping of Bright AGNs

Using time lags in variability between the UV/optical continuum, broad emission lines, and NIR/MIR continuum, one is able to estimate the sizes of broad line regions and tori in AGN, the technique called the "reverberation mapping method" (Fig. 3). Reverberation mapping has been applied for a limited number (~ 100) of nearby (less luminous) type 1 AGNs, since it requires a significant amount of telescope time to obtain multi-epoch data. In addition, investigating the time lag between the UV/optical continuum and NIR continuum is even more difficult to do with ground-based telescopes because of the high sky background and low atmospheric transparency. Having access to multiple passes over the deep survey regions in the mid-IR, allows us to detect AGN varying in the rest-frame optical/UV at redshift higher than 6. SPHEREx will certainly increase the statistics of the few objects currently having reberberation mapping data between NIR and optical.

The spectral information provided by SPHEREx from optical to NIR, will give us not only the fluxes of the Balmer and Paschen hydrogen recombination lines but also the brightness of the IR continuum simultaneously. Moreover, variation of the shape of the IR continuum will give us crucial information about the clumpiness of the dusty torus. In SPHEREx' ecliptic polar regions,

multi-epoch data, for 2 years will be available, which will enable us to calibrate the time lags in conjunction with complementary ground-based UV/optical data. The density of the type 1 AGNs from SDSS shows that there will be approximately 200 QSOs ($i < 18$ mag) in the polar regions, for which we can obtain high enough S/N data for the reverberation mapping of both broad emission lines and IR continuum. We can increase S/N of the data by applying spectral binning so that, we can make use of fainter QSOs ($i \sim 19$ mag) at least for the IR reverberation mapping.

Additional multi-epoch UV/optical imaging data from ground-based telescopes is crucial for the time lag measurements. This is possible using several small class (0.5-1.6m) telescopes mostly operated by the Korean community but also the Las Cumbres facility. There is possibility that the time lags can be larger than the operation time of SPHEREx (2 years) especially for the most luminous and distant QSOs. In order to account for this extreme cases, we plan to collect ground-based data at least 1-2 years prior to the launch of SPHEREx. The spectral resolution of SPHEREx is not high enough to measure the width of emission lines. Thus, we also plan to obtain the spectra of target AGNs using several mid-class ground-based telescopes (e.g., MMT).

2.5.2 Systematic Study of Optically Selected Type 2 QSOs

AGNs are commonly classified in two types (type 1 and 2), based on the presence of UV/optical featureless continuum and broad emission lines. The conventional model for AGN unification suggests that the type of AGNs is be simply determined by the line-of-sight relative to the dusty torus. However, recent observational studies show that the fraction of type 2 to type 1 strongly depends on AGN luminosity, suggesting that the conventional AGN unification might be over-simplified and that the torus structure depends on the AGN brightness (e.g., receding torus model). However, these studies are mainly based on IR/X-ray selection methods because it is extremely hard to search for type 2 AGNs using optical data due to the faintness of the optical counterpart. For example, SDSS discovered more than 400,000 type 1 QSOs, but only a few thousand type 2 QSOs. Thanks to the infrared spectral information, SPHEREx will be an ideal tool for a unbiased search for type 2 QSOs. The whole sky survey data will enable us to discover at least $\sim 3,000$ distant ($z > 0.8$) type 2 QSOs, assuming a conservative 10% type 2 fraction at high luminousity.

2.5.3 Star Formation Activity in Bright AGNs

Supermassive black holes are ubiquitous in the center of massive galaxies, and that their mass is strongly correlated with the mass of the host galaxy [e.g. 26]. This indicates that SMBH and galaxies are closely linked in their evolution, although the detailed mechanism of the coevolution is still under debate. One way to address this issue is to investigate how BH growth and galaxy growth evolve with cosmic time. As such, it is worthwhile measuring both the BH accretion rate and the star formation rate in AGNs, where the BH is actively growing in mass. This is challenging because most SFR indicators are also very prominent in AGNs. There are a few exceptions, such as [O II], PAH emission, and FIR continuum. Based on the existing SDSS QSO catalogue, we expect to detect the flux of PAH $3.3\mu m$ emissions for ~ 1000 QSOs. In addition, the WISE AGN selection can significantly increase the sample size by at least by a factor of 10, which will enable us to pursue the statistical study of the correlation between SFR and BH growth rate in nearby AGNs.
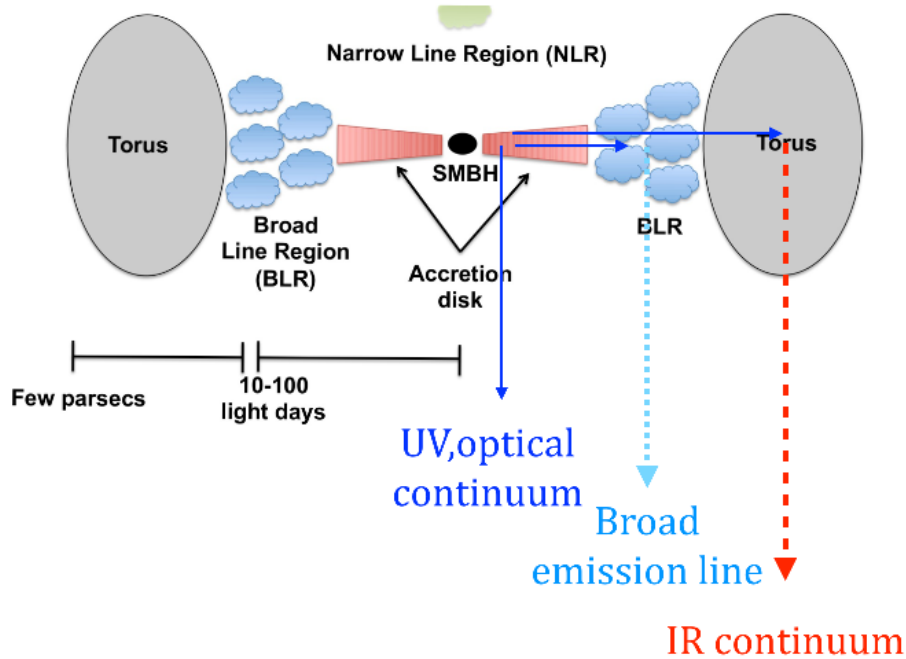
Figure 3. Schematic diagram of the central structure of an AGN. Using the time lags among the light in different wavelengths, we will be able to estimate the physical size of each component (Image credit : Claudio Ricci)

2.5.4 Synergies with eROSITA

eROSITA (extended ROentgen Survey with an Imaging Telescope Array) will be the primary instrument on the Russian Spektrum-Roentgen-Gamma (SRG) mission. eROSITA will provide an all-sky Xray survey, which will go $\sim$ 30 times deeper than ROSAT [27, 28] in the soft band (0.5-2 keV) and the first ever all-sky survey in the hard band (2-10 keV). It is expected to detect 10^5 clusters of galaxies up to redshift $\sim$ 1, about 3 million AGN to z$\sim$6, and about 500,000 stars.

The design of eROSITA is driven by effiiency in area coverage, which comes at the cost of resolution, with a half energy width (HEW) of 16" for pointed observations and about 26" in survey mode. Hence complete and deep multi-wavelength coverage of the sky is essential to identify the correct counterparts to the point-like X-ray sources like AGN and stars detected with eROSITA. SPHEREx will be crucial for the following reasons.

- SPHEREx will cover the entire sky, and provide full-sky object catalogs with higher angular resolution than eROSITA and homogeneous selection. Such homogeneity is fundamental for selecting the counterpart to the X-ray sources in a probabilistic way, using for example Maximum Likelihood Ratio [29] or Bayesian approaches [e.g. 30], in which the likelihood of an optically selected object being the correct counterpart to an eROSITA detection is tested against the likelihood of it being an unassociated source.

- SPHEREx will cover the longer optical wavelengths, NIR and MIR. At these wavelengths, AGNs will be easily identified: either due to their intrinsic SED [e.g. 31], or due to the redshifting of the strong UV emission of high-redshift AGNs into the SPHEREx bands. Additionally, the number of field sources decreases towards at longer wavelengths, which improves the success rate of counterpart identification methods.

- eROSITA and SPHEREx will both be deeper at the ecliptic poles. Here SPHEREx will reach a depth of ∼21 mag AB which will allow the identification of the faintest eROSITA sources. Currently, there are no suitable multi-wavelength data sets at the poles. In particular, at the SEP there are still a few thousand square degrees of areas where only WISE/GALEX is available for AGN identification; these are reliable but are too shallow for eROSITA.

- SPHEREx will continuously revisit the sky with a six month cadence (at a given position and given wavelength element; and 30 times more frequently at the ecliptic poles). This multi-epoch data set will contribute to understanding the physics regulating the activity of black hole, and provides valuable additional information on X-ray sources with ambiguous optical associations: between 2 sources with the same magnitude/colors, the one varying in time is more likely the AGN.

- SPHEREx will allow reliable spectroscopic redshift determination for X-ray sources. It is well established that intermediate and narrow band surveys are ideal for photometric redshifts [32] and many surveys are build with this in mind at optical wavelengths (COMBO-17 [33], COSMOS-21 [34], SHARDS [19]). This method relies on the capability for unambiguous identification emission and absorption lines. In particular for AGN, the emission lines from the host and from the vicinity of the central BH, combined with proper SEDs, will allow the determination of accurate spectroscopic redshifts [35–39]. It will bring much improvement on, for example, the X-ray AGN Luminosity Function, which is still very uncertain at z>3 [40–42].

2.6 Galaxy Groups with SPHEREx at z≲0.5

Fig. 4 shows a comparison of spectroscopically confirmed galaxy groups at z≲0.2 from SDSS [43] to galaxy groups at z≲0.45 from the Galaxy And Mass Assembly (GAMA) survey [44]. Compared to Sloan, GAMA finds galaxy groups much further out, sampling a depth and distance that is more comparable to the SPHEREx all-sky depth of AB≲19 mag. GAMA covered ∼300 deg^2, and identified more than 24,000 groups from a total of 360,000 GAMA galaxy redshifts [45], including 2400 reliable groups with at least N=5 reliable spectroscopic redshifts to AB≲19.8 mag, resulting in unbiased *dynamical* group and cluster mass-estimates [44]. WIGGLEz has provided about 100,000 redshifts to z≲1 [46]. SPHEREx will cover more than 100× the GAMA area to similar depths at 0.75–5.0 μm. Hence, SPHEREx will be able to estimate the *stellar* masses of about 3×10^4 Local Group Analogs (LGAs) to z≲0.1, and about 2×10^5 galaxy groups, ∼7×10^4 poor clusters and 3×10^4 rich clusters out to z≲0.5. For all 5080 SDSS groups at z≲0.2 and all 2400 GAMA groups to z≲0.45 — each with accurate dynamical masses from high resolution spectroscopy — SPHEREx will estimate reliable total stellar luminosities and total stellar masses, constraining the mass-to-light (M/L) ratios and dark matter properties for galaxy groups and clusters as a function of their
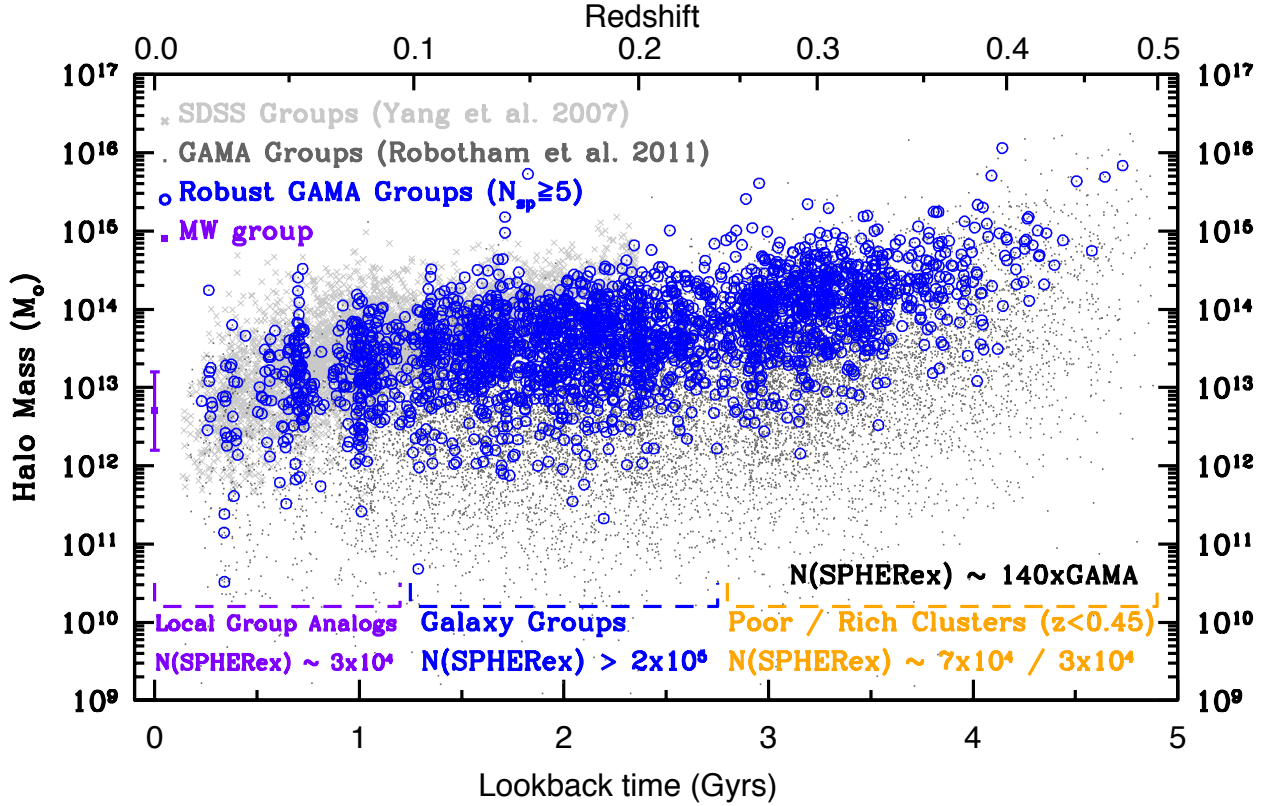
Figure 4. Comparison of spectroscopically confirmed galaxy groups at $z \lesssim 0.2$ from SDSS [43] (light grey crosses) to galaxy groups at $z \lesssim 0.45$ from the GAMA survey [44]; black dots and blue open circles). The purple data point is our Local Group. SPHEREx will cover more than $100\times$ the GAMA area to similar depths at 0.7–5.0 μm. Hence, SPHEREx will be able to estimate the stellar masses of about 3×10^4 Local Group Analogs (LGAs) to $z \leq 0.1$, about 2×10^5 galaxy groups, $\sim7\times10^4$ poor clusters and 3×10^4 rich clusters out to $z \leq 0.5$.

environment. That is, SPHEREx will complete the stellar mass census for the best spectroscopically studied regions in the sky where the dark-matter halo mass is known dynamically (*e.g.*, from SDSS, GAMA and WIGGLEz).

SPHEREx will measure groups like our own Milky Way + M31 group out to the Coma distance ($z \simeq 0.023$), detecting its LMC-like dwarf galaxies (*i.e.*, $M_{AB} \simeq -15$ mag) about ~6 mag below $M^\star$. Fig. 4 shows that in total SPHEREx will detect about 3×10^4 slightly more massive Local Group Analogs (LGA) to twice the Coma distance ($z \lesssim 0.05$), where dwarf galaxies surrounding Milky Way type L^* galaxies can be detected to $M_{AB} \simeq -16.5$ mag. The spectroscopic redshift of individual companion dwarf galaxies to $AB \lesssim 19$ mag will still be accurate enough to statistically constrain the number of dwarf galaxies around each L^* galaxy in the universe at $z \lesssim 0.05$, about 4–6 mag below M^* for 3×10^4 nearly Local Group Analogs. This will immediately constrain ΛCDM models, where the number of dwarf galaxies is predicted to be an order of magnitude higher than observed. Hence,

SPHEREx has the potential to directly address a key remaining uncertainty that the ΛCDM model has left unresolved in the local universe.

2.7 SPHEREx Galaxy Cluster Selection and Redshift Measurements for Clusters Selected in the X-ray, Sunyaev-Zel'dovich Effect and Optical

SPHEREx will see numerous clusters of galaxies in its all-sky survey. We first look at the clusters SPHEREx will detect on its own. We calculate the number of clusters SPHEREx will independently detect over the all-sky survey by extrapolating from two cluster catalogs built on SDSS DR8: The RedMapper catalog from [47], and the AMF catalog from Banerjee et al (in prep). These catalogs, restricted to the 10400 square degrees DR8 area, contain 26000 galaxy clusters (redMaPPer) and about 43,000 (AMF).

We apply the SPHEREx flux limit of $z_{AB} \lesssim 18.5$ mag to the potential galaxy clusters. For the reMaPPer catalog, we identify 9800 clusters with 5 or more cluster members brighter than this flux limit and with probability, p_{member}, of belonging to the cluster greater than 70%. Extrapolating this to the 75% of the sky gives an estimate of over 29,000 galaxy clusters that will be independently detected with SPHEREx and have high-precision redshift measurements. The median redshift of these clusters is $z_{med} \simeq 0.2$.

The AMF catalog, when restricting cluster membership to the 10 galaxies that mostly contribute to the overall likelihood, finds 18,700 clusters. Out of the clusters that are found in AMF and not in RedMaPPer, about half are also found in the WHL [48] catalog. The AMF finding would imply that SPHEREx will detect over 75%of the sky about 56,000 galaxy clusters and groups. Therefore we overall expect SPHEREx to detect at least 30,000 galaxy clusters and groups, and perhaps substantially more.

But while SPHEREx can be used to select tens of thousands of clusters, another exciting use of its data will be to estimate and/or improve redshift measurements for clusters discovered in other surveys. In particular, upcoming millimeter-wave cluster surveys (such as SPT-3G and AdvACTpol) and the eROSITA X-ray mission will discover 10,000-100,000 systems [49–51] and, as the intracluster medium-based observables in these surveys contain limited-to-no redshift information, auxiliary data is required to obtain robust redshifts.

The sheer number of clusters necessitates that the bulk of these redshifts be obtained from other wide area surveys (rather than pointed observations), and data from current and next generation optical imaging surveys such as the Dark Energy Survey, Pan-STARRS, and LSST will naturally fill this role [52–54]. In such surveys, clusters are identified as significant over-densities in photometric redshift space [e.g., 48] or as concentrations of red-sequence galaxies [e.g., 55–58], and modern optical cluster catalogs have excellent redshift performance ($\sigma_z/(1 + z) \sim 0.01$ -0.02).

In Fig. 5 we demonstrate how SPHEREx can further improve cluster redshift estimates in the presence of such imaging data. This simulated SPHEREx cluster data was created using photometric source, photo-z, and the redMaPPer cluster catalogs from the recent Science Verification release of the Dark Energy survey [58, 59] and full details will be provided in Bleem (in prep). These simulations suggest that the precision of cluster redshifts from SPHEREx should equal or exceed that of current generation optical surveys to $z \lesssim 0.6$ and remain $\sigma_z/(1 + z) < 0.03$ to $z \sim 0.9$. As the fits shown here were conducted only using data $1\mu m < \lambda < 4.1\mu m$ (though restricted to galaxies whose optical colors indicate high probability of cluster membership), these constraints can be further
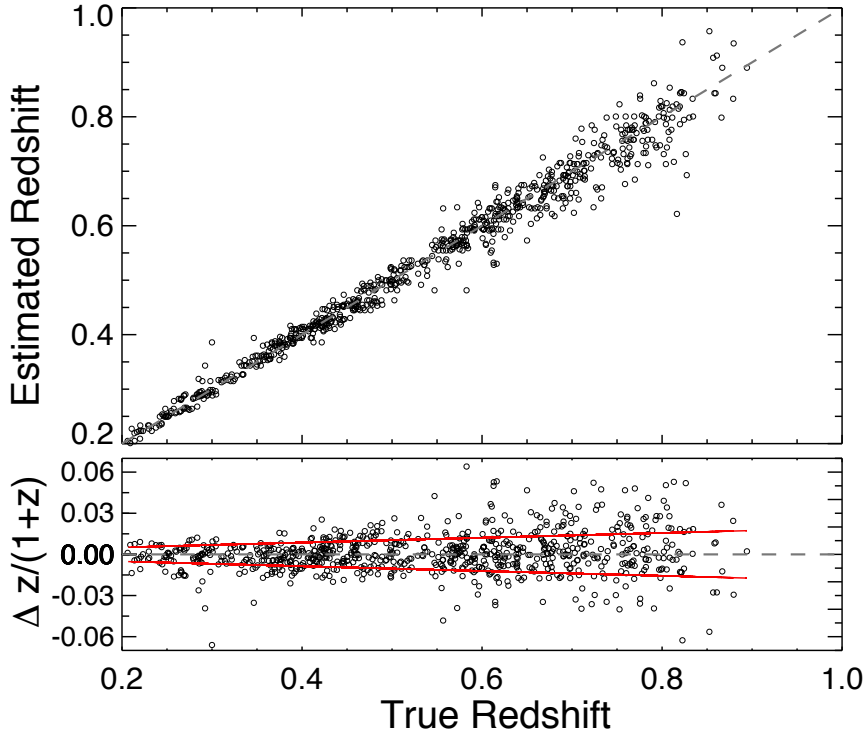
Figure 5. Simulation of cluster redshift recovery using SPHEREx data. *Top:* Recovered versus input cluster redshift for simulated SPHEREx observations of ∼800 clusters selected with the redMaPPer cluster identification algorithm in Dark Energy Survey data ($M_{500c} \geq 10^{14} M_{\odot}$, see [58]). *Bottom:* Similar to above, now plotting the difference between input and recovered redshifts scaled by $1/(1+z)$. Redshifts were estimated using SPHEREx spectra of galaxies identified in DES data as having high probability of cluster membership (interlopers can be present). The precision of the simulated SPHEREx redshift estimates exceeds that of current generation optical surveys at $z \lesssim 0.6$ and remains excellent ($\sigma_z/(1+z) < 0.03$) to $z \sim 0.9$, the highest redshift of clusters in this sample.

combined with the optical measurements to improve the precision. But these results indicate that by itself, SPHEREx could become a unique redshift machine for surveys such as SPT-3G, AdvACTpol and eROSITA. Perhaps more importantly for future cosmological constraints, however, SPHEREx data provides a useful cross-check of the redshifts—especially for clusters at redshifts near where the 4000Å break transitions between optical filters—as the smooth shifting of the 1.6 μm feature through the SPHEREx bands should not suffer similar discontinuities. For future surveys, ensuring low bias in redshifts (rather than improving the already excellent precision) will be important [60, 61].

Furthermore, using the cluster redshifts obtained by SPHEREx in combination with the next generation of CMB experiments allows for the tomographic reconstruction of the tSZ signal from these clusters [62]. A 3-dimensional tSZ map would enable us to study the evolution of the thermal properties of the intracluster medium (ICM), hence furthering our understanding of the thermo-dynamic processes involved in galaxy formation. Additionally, a 3D map such as this can be used to constrain cosmological parameters directly [63], or in combinations with other statistical mea-surements of the tSZ like the power spectrum e.g., [64–66], bispectrum or skewness [67, 68], and

the temperature histogram [69] all which are limited by the astrophysical uncertainties in the ICM modeling [70–72].

2.8 Synergy with future CMB experiments

2.8.1 kSZ signal for next CMB experiments

The amount of ionized gas observed in galaxies and clusters falls short of the cosmological abundance [73], especially for group-sized halos or smaller. The resulting uncertainty in the baryon profile of M^* halos will be a limiting systematic effect for future weak lensing experiments, such as Euclid, LSST and WFIRST [74, 75]. A large fraction of the gas is thought to reside in the outskirts of the halo, in a form that is too diffuse and too cold to be effectively imaged with X-ray or thermal Sunyaev-Zel'dovich (tSZ) observations. SPHEREx in conjunction with the next generation of CMB experiments will greatly increase our ability to measure this gas component via the kinematic Sunyaev-Zel'dovich effect.

The kinematic Sunyaev-Zel'dovich effect, which is the Doppler boosting of CMB photons scattering off electrons with a non-zero peculiar velocity, is a unique probe of low density and low temperature regions, its amplitude being directly proportional to the electron number density, and independent of the electron temperature. It is thus an unbiased probe of the total electron abundance associated with the halo, as well as of the gas profile.

In temperature units, the shift $\Delta T^{\mathrm{kSZ}}(\hat{\boldsymbol{n}})$ produced by the kSZ effect is sourced by the free electron *momentum field* $n_e \boldsymbol{v}_e$, and is given by [76, 77]

$$\frac{\Delta T^{\mathrm{kSZ}}(\hat{\boldsymbol{n}})}{T_{\mathrm{CMB}}} = -\sigma_T \int \frac{d\chi}{1+z} e^{-\tau(\chi)} n_e(\chi\hat{\boldsymbol{n}}, \chi) \, \frac{\boldsymbol{v}_e}{c} \cdot \hat{\boldsymbol{n}}, \tag{2.1}$$

where σ_T is the Thomson scattering cross section, $\chi(z)$ is the comoving distance to redshift z, τ is the optical depth to Thomson scattering, n_e and $\boldsymbol{v}_e$ are the *free* electron physical number density and peculiar velocity, and $\hat{\boldsymbol{n}}$ is the line-of-sight direction.

Since the kSZ signal at a galaxy location is proportional to the galaxy peculiar velocity, which is equally likely to be positive or negative, a simple cross correlation (or stacking) between the tracer position and a CMB temperature map will vanish. To remedy this, a number of estimators have been proposed in the literature [78–82], typically requiring either spectroscopic redshifts or very accurate photometric redshifts (say $\sigma(z) \lesssim 0.01$).

The signal to noise ratio S/N of the kSZ signal is very sensitive to both the actual electron profile, which is uncertain for low mass galaxy groups, and to the noise in the CMB temperature maps. For current and upcoming ground-based CMB experiments, the atmospheric noise gives an important contribution on top of the usual white noise. Therefore, the most realistic and conservative forecast for SPHEREx is obtained by rescaling existing measurements. We use the recent ACTPol measurement on CMASS galaxies [83] and use the following scaling:

$$S/N \propto \sqrt{\mathrm{Volume}} \, \sqrt{\frac{b^2 P(k_*)}{b^2 P(k_*) + 1/\bar{n}}} \propto \sqrt{N b^2 P(k_*)} \tag{2.2}$$

Here $\bar{n}$ is the mean number density, N is the total number of objects and b is the mean bias of the sample. Here $k_* \sim \ell_{\mathrm{kSZ}}/\chi(\bar{z}) \sim 3.5 \ h/\mathrm{Mpc}$, where we have assumed that most of the kSZ signal

comes from $\ell_{\mathrm{kSZ}} \sim 3000$ or larger. Note that the second equality in Eq. 2.2 holds in the shot-noise dominated regime, which is the case for both CMASS and SPHEREx galaxies at the scales of interest[1].

With the velocity reconstruction method, we require very good redshift determination, and therefore we include only the two highest redshift accuracy samples from [84]. For this population, we find $b \approx 1.1$ and $\bar{z} \approx 0.3$, with a total number of galaxies on half of the sky $N \approx 24.5$ million. With the simple rescaling described above, we forecast $S/N \sim 55$ on half of the sky, assuming a CMB map noise of 14 μK-arcmin. Note that the S/N will also depend on the particular mass and redshift distribution of galaxies, which is not considered here. Future CMB experiments are expected to have smaller map noise and should allow an even higher S/N detection, even though the amplitude of the noise from fluctuations in the atmosphere is still uncertain. For other recent detections using ACT, Planck and SPT data, see [85–87].

Because of the stringent requirement on redshift errors, in our forecast so far we have only used a small fraction of objects in the SPHEREx catalog. A different technique can be used in absence of redshift information [88]. This method only requires a statistical redshift distribution and will allow the use of the full SPHEREx catalog. It has been recently used to detect the kSZ signal from WISE selected galaxies in combination with Planck CMB data [89]. The basic idea consists of cross correlating tracers with the square of an appropriately filtered CMB map. The squaring operation removes the information about the direction of the peculiar velocity and therefore allows a detection in cross-correlation. Recent work [90] suggests that a very large signal to noise ($S/N > 100$) can be achieved by combining SPHEREx with future CMB experiments. This method requires a very good frequency cleaning of the foregrounds in the CMB temperature map, so the limiting factor will likely be the ability to do component separation in CMB maps on small scales.

As we have seen, the combination of current and future CMB experiments with large scale structure surveys like SPHEREx will yield very high S/N detections of the kSZ effect. This in turn will allow precision measurement of the baryon abundance (in the ionized state), of the baryon profile out to several virial radii and of the scale dependence of the velocity correlation function, potentially a powerful probe of scale-dependent modified gravity.

The ionization fraction and baryon profile is expected to depend both on mass and redshift of the host halo and could depend on other galaxy properties such as star formation rate, color, presence of an active AGN etc. The unique spectral coverage of SPHEREx over the full sky allows for a better characterization of several galaxy properties compared to a photometric survey, and will allow us to select and compare different populations, shedding light on the effect of feedback and star formation on the gas. When combined with tSZ measurements, the temperature of the IGM as well as the amount of energy injection will be constrained.

2.8.2 Galaxy – CMB lensing cross-correlations

In this subsection we consider the cross-correlation of positions of SPHEREx galaxies, with CMB lensing convergence maps, which probes the galaxy–matter cross-power spectrum at the redshift of the galaxy sample.

The amplitude of the galaxy–CMB lensing signal is proportional to galaxy bias, and assuming a cosmological model, it provides an independent validation of the bias parameters derived in the

---

[1]Since SPHEREx is in the shot-noise dominated regime on this scale, the result is independent of the value of k_*

SPHEREx-internal cosmology analysis. The left panel of Fig. 6 shows forecasts of the fractional constraints on galaxy bias of the SPHEREx cosmology analysis galaxy samples from galaxy–CMB lensing alone, assuming $f_{sky} = 0.5$ overlap between SPHEREx and a CMB-S4-like survey. These constraints are marginalized over wCMD cosmology parameters, and the redshift uncertainty of the SPHEREx galaxies.

Alternatively, if galaxy bias is known (e.g., determined from the galaxy power spectrum analysis), the galaxy–CMB lensing signal can used to constrain an amplitude parameter A_{lens} [91]. In general relativity, we expect $A_{lens} = 1$, and a measurement deviating from this value would imply modifications of the relation between the metric potentials Φ and Ψ, termed gravitational slip [92–95](or unaccounted systematic errors, such as a mis-calibration of the galaxy redshift distribution). The right panel of Fig. 6 forecasts the uncertainty of A_{lens} measurements as a function of redshift and physical scale, assuming that galaxy bias is determined in the galaxy clustering analysis, and marginalizing over the residual uncertainty in galaxy bias and wCDM parameters. On these very large scales, the clustering measurement of SPHEREx galaxies is cosmic variance limited and the constraints on A_{lens} approach its (half-sky) cosmic variance limit.
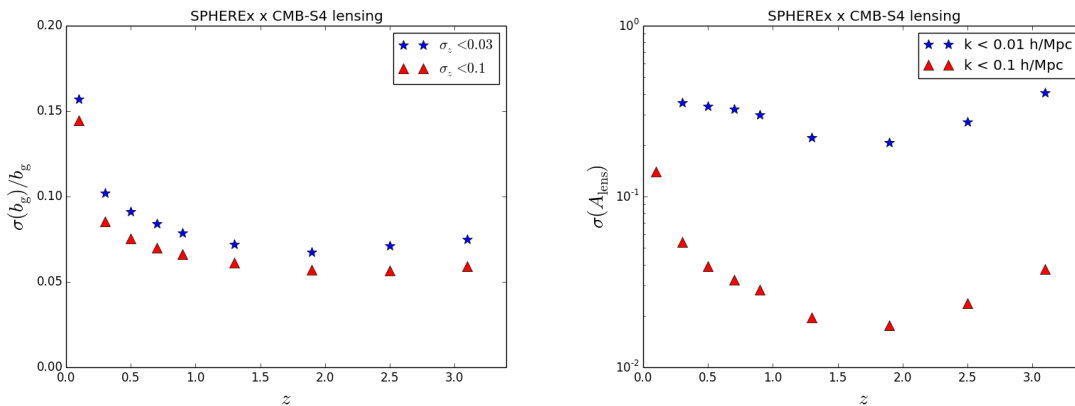
Figure 6. *Left:* Fractional constraints on galaxy bias in the nominal SPHEREx cosmology analysis redshift bins, derived by cross-correlating the SPHEREx galaxy catalog with the CMB lensing alone. The blue stars show forecasts for the $\sigma_z < 0.03(1 + z)$ galaxy sample, which is representative of galaxies in the bispectrum analysis, and the red triangles show forecasts for the $\sigma_z < 0.1(1 + z)$ galaxy sample, which is representative of galaxies in the power spectrum analysis *Right:* Constraints on the A_{lens} parameter as a function of redshift and wavenumber. The constraints shown with blue stars include only large scales, approximately $k < k_{eq}$, while the red triangles also include modes down to the quasi-linear regime.

2.9 Constraining Structure Growth with SPHEREx

The growth rate of structure is an important window on the behavior of gravity on large scales. A wide variety of alternative theories of gravity (e.g. f(R), symmetron, and massive gravity) have been developed over the last decade or so, predominantly motivated by the need to explain cosmic acceleration/dark energy [96]. In many cases, these theories can be tuned to give a cosmic expansion history that is almost identical to that of a cosmological constant-dominated universe in General
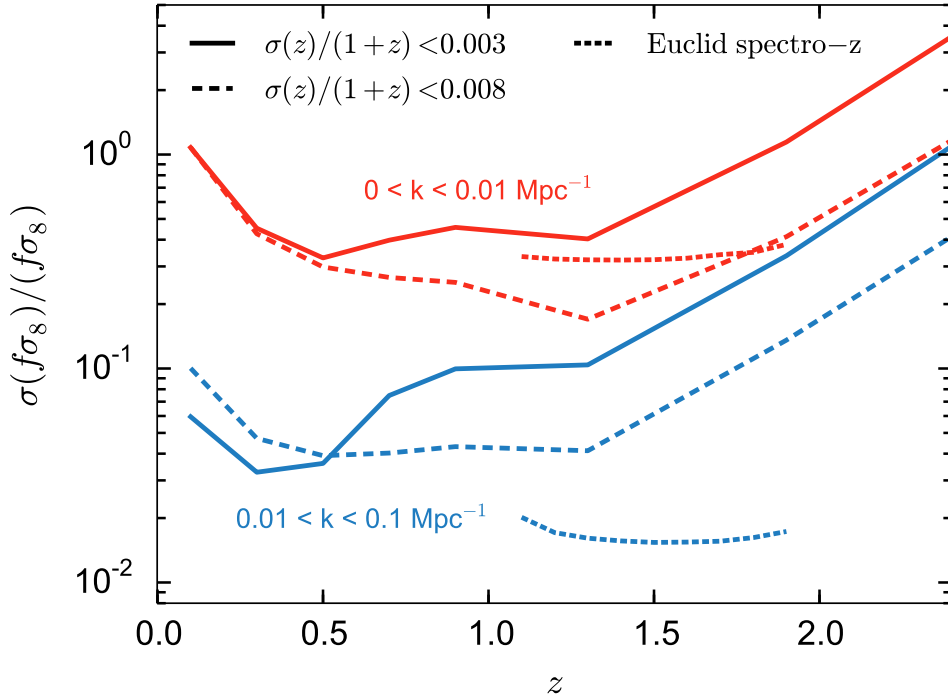
Figure 7. Fractional errors on the growth rate as a function of redshift, binned by wavenumber. The first bin (upper curves) are large scales, approximately $k < k_{\mathrm{eq}}$. The second bin (lower curves) are mostly linear scales, down to the quasi-linear regime. The solid and long-dash curves correspond to SPHEREx while the short-dash curves correspond to Euclid. The combination of SPHEREx and Euclid allows a complete measurement of the error growth rate over the redshift range when dark energy dominates.

Relativity. The growth rate, on the other hand, is often modified away from its GR behavior in an unambiguous manner, making it a highly valuable diagnostic for exotic gravitational physics [97].

The premier probe of cosmic growth is the redshift-space distortion (RSD) technique. This uses the fact that the apparent clustering pattern of galaxies is distorted due to their infall onto matter over-densities, by an amount that is proportional to the linear growth rate, $f(z)$ [98]. The RSD technique is typically applied only to spectroscopic galaxy surveys, as a loss of information in the radial direction (e.g. due to photometric errors) can easily wash out the signal. The two SPHEREx samples with the highest photometric precision will have sufficient redshift accuracy to make RSD measurements practical, however.

Fig. 7 presents Fisher forecasts for the fractional errors on the growth rate (from SPHEREx galaxy clustering), using a flat sky Fisher code, with no wide-angle or relativistic corrections, and with evolution neglected within each redshift bin. Photo-z errors and non-linear damping are included. Various nuisance parameters (including the bias in each redshift bin) have been marginalized. Similar predictions for a spectroscopic H-α galaxy survey with the Euclid satellite are included for comparison. On intermediate scales (blue lines), SPHEREx is expected to be strongly complementary to Euclid, providing ∼few percent constraints in the $z < 1$ range where the growth rate is changing most rapidly.

The full-sky coverage of SPHEREx, coupled with its high source density, will also allow "ultra-large" scales (i.e. approaching the cosmological horizon size) to be probed down to the cosmic variance limit for $z \lesssim 1$. Novel relativistic phenomena arise in this regime, comparable in size to the scale-dependent bias effect caused by primordial non-Gaussianity [99–102]. Many alternative theories of gravity deviate from GR in a scale-dependent manner, so it is possible that these effects could be drastically modified in ways that are unobservable on smaller scales [103–105]. Though precision is intrinsically limited here due to cosmic variance, SPHEREx will nevertheless offer the best constraints on growth on ultra-large scales of any individual survey.

2.10 Synergy with Future 21 cm Surveys

New low frequency interferometers such as the MWA [106], PAPER [107], LOFAR [108], and GMRT [109] are nearing sufficient sensitivity to see redshifted 21 cm emission from the Epoch of Reionization, and the next-generation HERA [110] (now under construction) will deliver SNR > 10 constraints on reionization parameters [111, 112] in the coming years. However, cross correlations with other probes will be needed to confirm any purported detection and establish a consistent picture of the astrophysics of the EOR. Of particular interest is the cross correlation between redshifted 21cm emission from the neutral IGM (between ionized bubbles) and redshifted Ly-α emission from the galaxies (inside the ionized bubbles) that SPHEREx will map.

Simulations and theory predict a negative correlation on scales of order the typical bubble size at any given redshift [113–115]. [113] self-consistently simulate 21 cm IGM emission and galactic Ly-α emission, predicting that the anti-correlation peaks at 5 Mpc (2 arcmin) scales at $z = 10$, and at 50 Mpc (20 arcmin) at $z = 7$. [114] show that this anti-correlation evolves in strength as reionization progresses, peaking near the midpoint of reionization. On much smaller scales, of order the galaxy size, the matter field overdensity that gave rise to the galaxy in the first place is dense enough to stave off reionization, thus giving rise to a local peak in 21cm emission. This latter effect should yield a positive correlation on angular scales smaller than 15 arcsec.

Beyond shedding light on the astrophysics of reionization, the 21 cm–infrared correlation is likely the only way to probe the EOR component of the near infrared background (NIRB). While early studies proposed that the angular fluctuations on few arcmin scales were sourced by these first sources [e.g., 116–118], recent observations and modeling propose alternative explanations [e.g., 119] such as intermediate redshift sources with significant intrahalo light [120, 121]. The EOR component is predicted to be a factor of roughly 50 lower in surface brightness, and can only be recovered through cross correlation with other EOR probes, such as 21 cm maps.

The main obstacle in measuring the 21 cm–infrared correlation is foregrounds. Even if low radio frequency foregrounds were perfectly uncorrelated with near infrared foregrounds, their presence in a cross correlation estimate contributes a sort of sample variance noise. This noise can only be mitigated through better foreground subtraction/masking, or using a larger sky area. A rough estimate of the SNR of a cross correlation measurement, assuming the noise is dominated by residual uncorrelated foregrounds, is given by

$$\mathrm{SNR} \sim 3 \left(\frac{P_{\mathrm{IR,cosmo}}/P_{\mathrm{IR,FG}}}{10^{-3.5}} \right)^{1/2} \left(\frac{P_{21,\mathrm{cosmo}}/P_{21,\mathrm{FG}}}{10^{-2}} \right)^{1/2} \left(\frac{\theta_{\mathrm{FOV}}}{70°} \right) \left(\frac{3'}{\theta_{\mathrm{PSF}}} \right) \tag{2.3}$$

These numbers assume 50% of the infrared pixels are masked due to point sources [121], and 99.9% of radio foregrounds are subtracted $((10\text{mK})^2/(0.1\% \times 100\text{K})^2)$. The image resolution is limited by that of the radio interferometer, typically a few arcmin for the MWA and HERA. First generation 21cm experiments are subtracting $\sim 90\%$ of foregrounds [122], and 99.9% subtraction is not far out of reach for next generation experiments. It may be possible to take advantage of the frequency dimension of 21 cm image cubes to subtract foregrounds even further.

What relevant capabilities does SPHEREx bring? Of all the current and future wide-field near infrared sky surveys (DES, Pan-STARRS, TESS, WFIRST, EUCLID, ...) SPHEREx is the most promising for this cross correlation measurement. Its 6" resolution is coarse enough to permit a survey of the whole sky, yet fine enough to mask out infrared point source foregrounds while leaving at least 50% of the sky unmasked [121]. Further, the spectral resolving power of R≃40 is equivalent to a redshift resolution of $\Delta z = 0.2$ for Ly-α, permitting studies of the evolution of the cross correlation over the course of the EOR. The frequency dependence of the cross correlation is also a check on whether a purported cross correlation is due to foregrounds. Lastly, ground-based IR surveys see a bright and variable airglow of OH lines around 1μm, and mosaics from wide field ground-based IR surveys typically combine postage stamp (10s of arcmin wide) images from many different observing conditions. This has the effect of entirely washing out diffuse structures on larger scales. SPHEREx sees only the zodiacal background, a factor of $\sim 5-10$ lower in surface brightness than airglow, and its large instantaneous field of view permits observations of $\sim 5°$ scale regions of sky under the same observing conditions.

2.11 Supernovae Investigations

During routine observations, SPHEREx will provide a unique opportunity to constrain the physics of supernovae. These stellar explosions contribute to the origin of elements, influence star formation, and are one of the main laboratories in astrophysics and cosmology. For both thermonuclear and core-collapse supernovae, SPHEREx is ideally suited to constrain overall rates, nucleosynthesis processes, and production of dust. Because classification of supernovae by late-time spectra is not time-sensitive, SPHEREx can make these measurements for free during its normal survey operations.

Thermonuclear supernovae of white dwarf stars, so called SNe Ia, have light curves powered by radioactive decay. The vast majority of them are "standardizable candles," probing the expansion history of the Universe to high precision. However, discoveries of sub-types of SNe Ia [e.g., SNe Iax, 123] and the subtle dependence of calibrated supernova luminosities on host galaxy properties [124] have highlighted the diversity of the progenitor channels and explosion mechanisms. Understanding this mix will be key to improve precision measurements of the properties of Dark Energy.

Core-collapse supernovae, on the other hand, mark the end of life of massive stars. They are very diverse and play important roles in star formation. Although the explosion mechanism is not yet fully understood, the frequency, high luminosity, and short progenitor lifetime of core-collapse supernovae make them prime candidates for future studies of the first stars during the dark ages. Key products of the nuclear burning—visible in the near- and mid-IR—can probe explosion mechanisms and the onset of dust formation, basic ingredients in the life cycle of the elements.

SPHEREx provides a unique spectral window for a large, uniformly-selected sample of local supernovae, and addresses these questions:

1. What are the local rates of supernovae of different types and sub-types? The rate measurement is a powerful tool to distinguish between progenitor channels. Comparison of rates between sub-types of supernovae provides clues to the origins of the observed diversity.

2. Are the "unusual" reddening laws seen in supernovae produced by freshly synthesized dust or by heating of dust in the circumstellar environment? Dust will reveal its formation and destruction history by the energy distribution in the mid-IR, i.e., a few microns. The existence of dust in the circumstellar medium is intricately linked to the evolution of the progenitor system leading up to the explosion.

3. Are CO and SiO able to form in all types of supernovae? These molecules play important roles in the cooling of supernovae. The timing of the onset of cooling provides constraints to the explosion physics.

4. What is the distribution of argon lines in different types of supernovae? Argon is a key indicator of the conditions that cause nuclear burning breakout from quasi-nuclear equilibrium. Argon lines are observable only in the mid-IR. Study of supernova argon lines provides insight on mixing processes during nuclear burning.
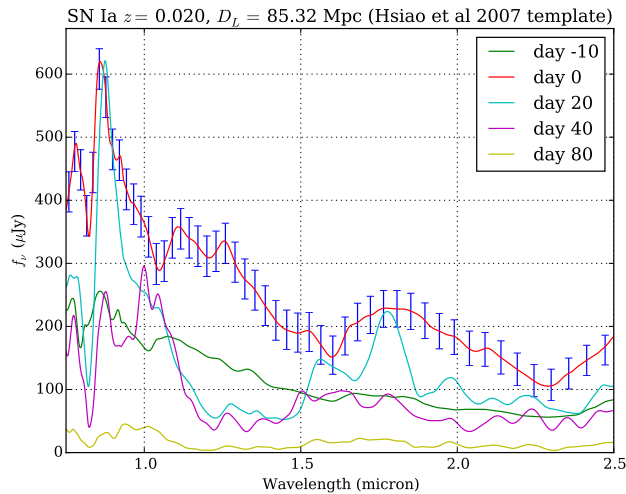
Figure 8. Demonstration of SPHEREx spectral classification for SN rate measurements. This spectral template prediction for a local SN Ia shows broad iron features at $\sim$1.6 μm, whereas a Ib/c would show a carbon-oxygen dominated spectrum, and a SN II would show strong Paschen lines. SPHEREx error bars for a survey-difference search for transients are compared to the evolution from ten days before to eighty days after maximum (optical) light.

SPHEREx will provide near- and mid-IR spectra for supernovae in larger numbers than will be feasible with Spitzer, JWST, or WFIRST. From a local SN Ia rate of $0.55^{+0.50}_{-0.29}$(stat.)$\pm$0.20(sys.) Mpc^{-3} year^{-1}[125, based on just 3 SNe], we expect $\sim$ 135 events on the sky each year brighter than the one plotted in Fig. 8, showing the template of [126] with SPHEREx error bars for a local SN Ia at $z = 0.02$. The error bars are based on a spectral difference of two surveys to look for transients. Such

nearby supernovae are relatively bright; at B-band maximum light (day 0), the SPHEREx signal-to-noise ratio is 124 for a template amplitude fit to 0.75–2.5 μm. Such a supernova may be visible and classifiable for perhaps 30 days, while nearer ones will last longer. Core-collapse supernovae are 3–4 times more common though typically dimmer. Thus SPHEREx will see many supernovae per year. Most importantly, all SPHEREx supernovae will have spectroscopic information. By contrast, for most supernova surveys the efficiency for selecting events for spectroscopic follow-up (depending on human decision-making) is low inevitably introducing a large systematic error into the rate measurements.
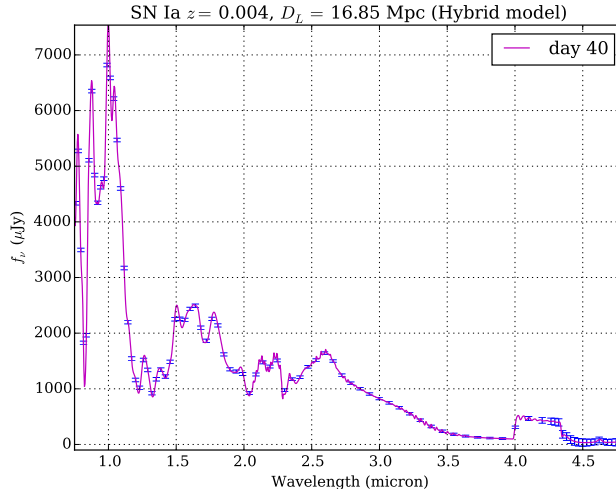
Figure 9. Onset of CO formation is more visible from the fundamental band at 4.3 μm rather than from the first overtone at 2.3 μm, which is heavily blended by strong iron group features (2.3–2.5 μm). Here we give a template spectrum at the onset of CO formation modeled at day 40 for a nearby, sub-luminous SN Ia compared to SPHEREx errors for a survey difference.

Previous detailed modeling suggests that IR supernovae spectra evolve slowly with time and homogeneous light curves [127–130]. SPHEREx can establish this similarity over a wide range of progenitors, or prove it wrong and provide a new tool to probe the variety of SNe Ia, with obvious consequences for the use of mid-IR for supernova cosmology. Detection of the dust precursor CO in molecular bands (Fig. 9) would indicate significant amounts of carbon, low temperatures, and sufficiently high densities. For both core-collapse and thermonuclear supernovae, CO also carries information about the local ionizing radiation environment, because $C+O^+ \rightarrow CO^+$ formation is significantly faster than $C+O \rightarrow CO$ [127, 131, 132]. Carbon allows us to detect specific subclasses of SNe Ia/Iax. Molecular cooling lowers the temperature in the outer regions, modifying the transparency of the outer layers and setting the stage for dust formation. Similarly, for core-collapse supernovae, CO and dust-formation have already been observed, for example in SN1987A and SN1998S. Only the much weaker, and heavily-blended, overtone of CO can be observed from the ground, giving SPHEREx—observing the fundamental—a useful capability in concert with ground-based supernova studies (e.g., $\sim$ Carnegie Supernova Project).

SNe Ia show absorption laws unusual for the ISM, in particular for cases of high redden-

ing/extinction [133–135]. SPHEREx can probe for dust in large numbers of SNe Ia. The circumstellar dust may originate from red-giant winds of a donor star or the stellar evolution of the stars of either single white dwarf or double white dwarf progenitor systems. Argon lines are excellent tools to separate different regimes of burning, namely to probe the region of incomplete Si burning. Argon lines will provide new insights and constraints on the instability and mixing of nuclear flames, off-center delayed-detonation transitions, mergers, and rotation.

Few studies of supernovae have been published for wavelengths beyond the K band at about 2 micron. Though upcoming missions (like JWST and WFIRST) will open this window, providing exquisite data for a small number of objects, SPHEREx in the normal course of operations will yield a large, uniform sample, probing the intrinsic and apparent diversity of objects key to high-precision cosmology.

3   Galactic Science

We divide the discussion of Galactic Science enabled by SPHEREx into two sections: Stars (Sec. 4) xsand Interstellar and Circumstellar Matter (this section). SPHEREx will provide low resolution spectra of millions of stars which, particularly when combined with spectrophotometric and astrometric data from Gaia, will address problems related to exoplanets, planetary systems, and Galactic structure as well as providing improved data on fundamental stellar parameters. At the same time, SPHEREx will obtain data on emission and absorption in interstellar and circumstellar space which can be used to study the energetics of interstellar shocks and outflows, to study the distribution of hydrocarbons and to search for deuterated species amongst them, and to characterize the properties of interstellar grains in a variety of environments.

3.1   Aromatic and aliphatic hydrocarbons

Polycyclic Aromatic Hydrocarbons (PAHs) play a key role in the heating, chemistry and ionization of the interstellar gas. Their emissions dominate the flux observed from the Galactic plane in the 5.8 and 8 μm bands of Spitzer/IRAC [136] and the band of WISE. PAH emissions reveal a population of bubbles associated with young stars in regions of high-mass star-formation[137]. Whereas the IRAC 8 μm band is sensitive to the C-C mode at 7.7 μm, SPHEREx can map the aromatic C-H stretch at 3.3 μm, and distinguish it from its aliphatic counterparts in the 3.40 - 3.56 μm range. The Galactic plane survey, GLIMPSE [138], performed with IRAC at Galactic latitudes $|b| \leq 1^0$, suggests that PAH emissions above the SPHEREx detection threshold will be present up to $|b| \sim 5^0$ or greater, the SPHEREx sensitivity to PAH emission being a factor ~ 2 better than GLIMPSE for extended sources. This opens the possibility of studying UV-heated PAHs much higher above the Galactic plane than in previous surveys, and of determining the ratio of aliphatic to aromatic C-H sites.

In addition, the SPHEREx bandpass covers the analogous C-D stretching modes at 4.40 μm (aromatic sites), and the 4.56 - 4.85 μm range (aliphatic sites). The latter were detected toward two photodissociation regions (the Orion Bar and M17) by [139], using ISO, implying that PAHs were deuterated at the several $\times 10\%$ level. This led to the suggestion that a significant fraction, or even the majority, of the Galactic deuterium might be sequestered on PAHs [140], providing an explanation for the surprisingly large variations (from 5 to 22 ppm) observed in the atomic D/H ratio [e.g., 141]. Models for the preferential incorporation of D into PAHs provide theoretical support

for the possibility of such a high level of deuteration [140, 142]. More recently, however, AKARI has surveyed ~ 50 HII regions for the C-D stretching mode of deuterated PAHs and obtained only six "unambiguous" detections, suggesting that high levels of deuteration are sometimes present but are not ubiquitous [142]. The large statistical power provided by the SPHEREx' all-sky survey, targeting both the C-H and C-D stretching modes, promises to resolve the question of how widespread deuterium sequestration onto PAHs is.

3.2 SPHEREx Observations of Hydrocarbon Grains
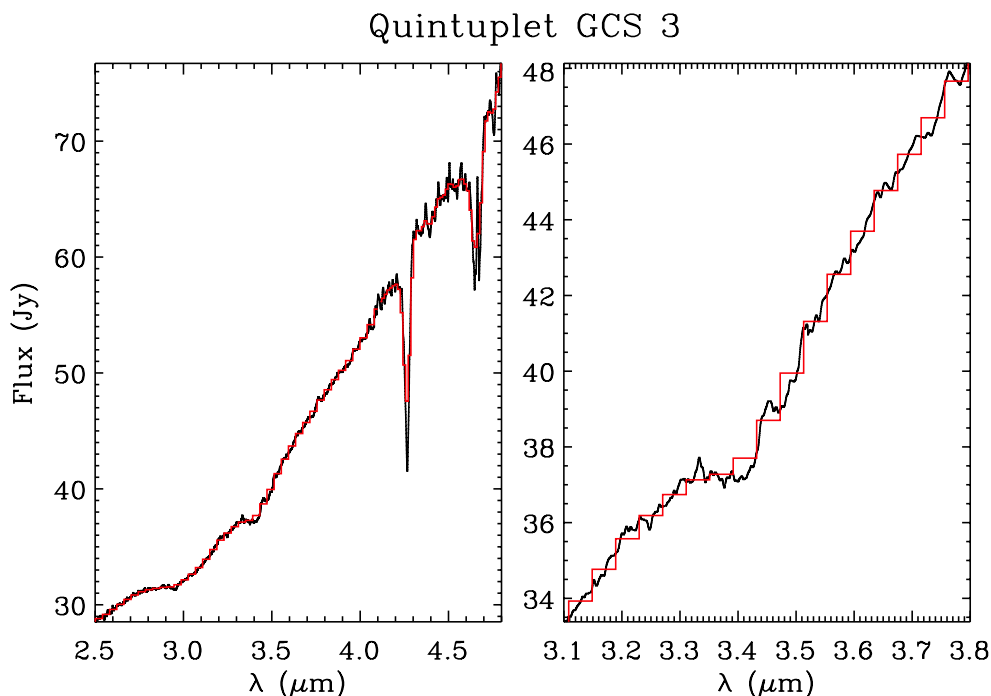
Figure 10. ISO/SWS observation of the Quintuplet cluster source GCS 3 at a resolving power of 400 (black) and convolved for a portion of the wavelength range, to the SPHEREx resolving power (red). The feature near 3.4 μm is due to hydrocarbons along the diffuse ISM sight-line, while features near 3.0, 4.3, and 4.7 μm are due to H_2O, CO_2, CO, and OCN^- ices respectively. The aliphatic group substructure will not be resolved by SPHEREx, but the overall feature is easily detectable.

The aliphatic hydrocarbon absorption features near 3.4 μm, observed in the diffuse ISM, have an abundance of a few to 10% relative to carbon in aromatic compounds (PAHs, which consume 10-20% of the cosmic carbon). To date, the aliphatics have been looked for and thus seen only along selected lines of sight, so the SPHEREx all sky survey can greatly increase our understanding of their prevalence and significance. The origin of the aliphatic hydrocarbons was initially thought to be in heavily processed ices, but this is disputed based on a lack of polarization in the observed features [143, 144]. Instead, aliphatic hydrocarbon dust might evolve from the interplay of H-atom reaction with and UV photolysis of graphite dust in the ISM. Production in carbon-rich evolved stars is also

a possibility given the detection toward the young planetary nebula CRL 618 [145]. However, these studies are based on the detection of the 3.4 μm absorption in just ∼10 lines of sight in the diffuse ISM, and in one evolved stellar envelope. A SPHEREx all-sky survey would enable a study of the hydrocarbon abundance across the Galactic Disk. For example, do aliphatic hydrocarbons evolve from PAH species driven by strong UV fields in the ISM? Are they strong near massive stars with strong UV fields? Are they preferably associated with AGB stars? Is there a gradient in strength with Galactocentric radius, related to the fraction of carbon stars among AGB stars and thus the star formation history?

Contamination with PAH emission would complicate the analysis; an all-sky survey is needed to find sight-lines suitable for aliphatic hydrocarbon study. Although at a resolving power of 40, the CH, CH_2 and CH_3 groups would not be resolved, SPHEREx is well suited to determine the total volume of aliphatic hydrocarbon dust through the 3.4 μm absorption feature (Fig. 10) and this can be compared to the total volume of dust determined from the continuum extinction. SPHEREx will enable this work to be extended to extragalactic nuclei, which often show prominent 3.4 μm bands. Extrapolating from the Galactic SPHEREx results, we will learn what this feature tells us about the physical and star formation history in external galaxies.

3.3 The Life-cycle of Interstellar Dust & the 3.3 μm PAH feature in nearby galaxies

The combination of wavelength coverage and angular resolution provided by SPHEREx opens up a wide range of exciting science questions in nearby galaxies. SPHEREx sensitivities will allow widespread detections of the 3.3 μm PAH feature as well as the near-IR H recombination lines, which provide extinction-insensitive tracers of massive star formation. At 6 arcsec resolution, SPHEREx resolves the scale of individual star forming regions and molecular clouds in all of the galaxies of the Local Group. Nearby objects like the Magellanic Clouds are highly resolved by SPHEREx into ≤ 2 pc resolution elements. For the LMC, this will mean > 10^8 individual resolution elements across the main body of the galaxy. In galaxies out to 10 Mpc, SPHEREx resolves galactic disks at hundreds of pc resolution, and can distinguish arm/interarm regions and separate nuclear regions from the disk. Beyond widespread PAH and H recombination lines, bright regions of nearby galaxies will show a wealth of near-IR lines including H_2 vibrational lines, [Fe II] 1.257 & 1.646 μm, and many others. These lines will be of great interest for diagnosing physical conditions in the gas, particularly relating to shocks and feedback from massive star formation and active galactic nuclei. Here we focus on two questions related to the 3.3 μm PAH feature and maps of star formation in nearby galaxies.

PAHs play key roles in the interstellar medium. In dense clouds they influence chemical reactions, most importantly the formation of H_2 [146–148]. Across many ISM phases, PAHs are the dominant contributor to the photoelectric heating rate [149, 150]. PAHs also radiate a significant fraction of the total infrared emission from galaxies [∼ 10 − 20% 151], making them a potentially useful tracer of star formation out to high redshift [4]. The properties of PAHs (size, charge, abundance) influence how effectively they carry out these roles. For example, the photoelectric heating rate depends on the size distribution of the grains and their charge [152]—e.g. when PAHs are more highly charged, they are less effective sources of photoelectric heating. Correlations of [CII]-to-PAH emission with PAH band ratios observed in nearby galaxies [153, 154] suggests that the physical properties of the PAHs are indeed playing a role in the heating and cooling of the ISM. The key

open question we need to answer is how and why the properties of PAHs vary between galaxies and with environmental conditions within galaxies.

The mid-IR PAH emission bands provide a suite of useful diagnostic features for the population of PAHs. Much work has been done attempting to understand how PAH properties change with environment making use of the mid-IR lines with ISO and Spitzer observations [e.g. 151, 155]. However, the mid-IR bands suffer from some degeneracies between the features tied to charge and those tied to PAH size. For example, while the 7.7/11.3 μm ratio is often used as a tracer of PAH ionization, this ratio can also vary if the size distribution of PAHs changes [see 156, for more detail]. The 3.3 μm feature is a crucial diagnostic in this regard because its emission is strongly associated with small, neutral PAHs, making it one of few mostly unambiguous tracers for the PAH population. Ratios of 3.3/11.3 μm features, for instance, are a clean tracer of size, since both 3.3 and 11.3 are from neutral PAHs. Observations of the 3.3 μm feature can therefore serve as an anchor for interpreting the other band ratios, separating the effects of PAH size and charge variation. Unfortunately, the 3.3 μm feature was not covered by Spitzer and previous and subsequent surveys (e.g., with ISO, AKARI) have had limited coverage of the local galaxy population. SPHEREx will change this.

The combination of all-sky SPHEREx mapping of the 3.3 μm feature with existing data from WISE and the Spitzer archive will enable a definitive study of the variability of PAH properties across all local galaxies. Since SPHEREx maps the whole sky, every spectral mapping observation with Spitzer-IRS will gain coverage of the 3.3 μm feature—this will give a wide ranging basis set of full PAH coverage (from 3.3 through 17.0 μm). Moving beyond the targets with direct spectroscopic PAH coverage, Spitzer mapped a large sample of nearby galaxies with the IRAC 8 μm band, which primarily samples the 7.7 μm PAH complex. With spectroscopic-to-photometric PAH calibrations [see for example 153], this provides 3.3/7.7 diagnostics for a huge number of galaxies. Likewise, in the largest possible sample, the WISE all-sky survey band 3 covers a combination of the 7.7 and 11.3 features. Combining these datasets will let us map the variation of PAH populations across all nearby galaxies and tie the resolved changes to local environment.

One specific question that needs to be addressed about PAHs is what causes their disappearance at low metallicity [156–160]. The deficit of PAHs at low metallicity is a long-standing puzzle—some combination of PAH production, destruction or ISM processing changes dramatically at $12+\log(\text{O/H})\sim 8.1$. Studies with Spitzer-IRS suggest that low metallicity PAHs have *smaller* average sizes compared to PAHs in higher metallicity galaxies, inferred from the relative weakness of the 17.0 μm feature [151]. This observation has important implications for the PAH lifecycle—larger PAHs are the most difficult to destroy, so a size distribution shifted towards smaller sizes most likely indicates a deficit in large PAH production [155]. However, ambiguities in the relative importance of size and charge in setting the ratio of 17.0 to other bands remain an obstacle. SPHEREx will observe 3.3/11.3 ratios both spectroscopically (in all Spitzer-IRS maps) and photometrically (in combination with WISE band 3) giving the definitive dataset for answering why PAHs disappear at low metallicity.

3.4 Probing the Gas Phase: Synergy with GLIMPSE and MIPSGAL

The SPHEREx results will build upon, and be enhanced by, numerous previous surveys. The GLIMPSE[2] and MIPSGAL[3] surveys of the galactic plane carried out by Spitzer provide an excellent example of this synergy. GLIMPSE surveyed the entire galactic plane, covering 360 degrees in longitude and at least $\pm$ 0.5 degree in latitude in the Spitzer bands at 3.6 and 4.5 μm [and much of the inner Galaxy at 5.8 and 8 μm and over a larger latitude range], providing a data base which might be considered an extension of 2MASS. The GLIMPSE beam size is $\simeq$ 2". The GLIMPSE data base contains tens of millions of sources, and the brightness limits of the catalog show that SPHEREx will achieve more than 5σ per spectral resolution element for GLIMPSE 3.6 and 4.5 μm point sources, even from 4.18 to 5 μm where SPHEREx's continuum sensitivity is reduced due to the higher spectral resolution. MIPSGAL, synergistic with GLIMPSE, surveyed a goodly portion of the inner galactic plane at 24 and 70 μm; although these wavelengths are far outside of the SPHEREx band, the MIPSGAL discoveries described below have been found to be bright at J, H, and K and are therefore candidates for study from SPHEREx.

A potentially exciting example of the synergy between GLIMPSE and SPHEREx comes from a class of object discovered by GLIMPSE to show extended regions of excess 4.5 μm emission. Dubbed "Extended Green Objects (EGOs)" by [161, hereafter C08] – "green" because the 4.5 μm band has traditionally been displayed as the green channel in false-color images – many of these objects show a clear association with massive young stellar objects (MYSOs). The association of 4.5 μm emission with MYSOs suggests the influence of shock waves. Shock waves are widespread in the ISM, and are often associated with supernova remnants and supersonic protostellar outflows. They may compress, heat and ionize the interstellar gas through which they propagate. Slow shocks propagating in molecular gas radiate strongly in rovibrational and pure rotational transitions of molecular hydrogen, many of which lie within the SPHEREx wavelength range: the S(9) pure rotational transition at 4.69 μm is expected to be particularly strong. C08 posited line emissions from outflow-driven shock waves as the origin of the observed IRAC 4.5 μm excess, suggesting H_2 pure rotational lines (the S(9), S(10) and S(11) transitions accessible to SPHEREx) as dominant contributors to the 4.5 μm flux. Subsequently, [162] conducted a near-IR search for H_2 vibrational emissions from EGOs; roughly one-third of the targeted sources showed detectable H_2 vibrational emissions, although in many cases the H_2 line emission showed a morphology differing from that of the IRAC 4.5 μm emission. This led [162] to argue that scattered continuum emission might contribute significantly to the 4.5 μm fluxes measured in many EGOs (although the effects of differential dust extinction between 2.1 and 4.5 μm might provide an alternative explanation for at least part of the observed morphological differences.)

A catalog of roughly 300 EGOs detected in the GLIMPSE survey has been presented by C08. For this sample, the median solid angle subtended by the sources was 114 sq. arcsec, corresponding to $\sim$ 3 SPHEREx pixels and suggesting that the *typical* source will only be marginally resolved at the angular resolution of SPHEREx, but sources as large as 1767 sq. arcsec ($\sim$ 50 SPHEREx pixels) were catalogued. For the larger EGOs in which the diffuse emission can be resolved spatially from the associated MYSOs, SPHEREx has the sensitivity to readily detect line-dominated sources in

---

[2]http://www.astro.wisc.edu/glimpse/
[3]http://mipsgal.ipac.caltech.edu/

the C08 catalog, and will potentially add a large number of additional sources at higher latitudes ($|b| > 1^0$). Results from SPHEREx will have the potential of (1) revealing the relative contribution of H_2 line emission to the IRAC-detected 4.5 μm excesses, and thus resolving an outstanding question about their nature; (2) expanding the sample of MYSOs, and (3) yielding H_2 line ratios that could constrain the physical conditions in the emitting gas.

In addition to the pure rotational lines of H_2 that fall within the SPHEREx wavelength range, several other spectral signatures of warm, shocked-heated gas may be detected. These include several H_2 rovibrational lines, the strongest being the $v = 1 - 0$ S(1) line at 2.12 μm, and two near-IR [FeII] lines at 1.26 μm and 1.64 μm. Because the latter two lines are optically thin and originate in the same upper state of Fe^+, their intrinsic ratio is a constant determined by atomic physics: the observed line ratio is therefore a useful probe of extinction. Line maps obtained by SPHEREx will complement smaller ground-based surveys (UWISH2 and UWIFE) of the 2.12 μm H_2 and 1.64 μm [FeII] lines that have revealed a large sample of PDRs, jet outflow regions, planetary nebulae, and supernova remnants [163, 164].

The combined GLIMPSE and MIPSGAL surveys have identified other potentially interesting classes of objects. One group is known as Yellowballs due to their appearance in a false-color presentation of GLIMPSE+MIPSGAL data; another is the more prosaically named MIPSGAL bubbles [165]. The MIPS bubbles have been studied spectroscopically from the ground and searched for in other catalogs and found to be a heterogeneous group [e.g., 166]. They include planetary nebulae, shells around massive, mass-losing-stars such as Wolf-Rayet stars and Luminous Blue Variables, and shocked-excited nebulae powered by winds ad outflows from high mass young stellar objects. The Yellowballs are a more recent discovery; circumstantially they are identified as a previously unknown stage in massive star formation [167], but extensive ground-based spectroscopy has yet not been reported.

The remarkable characteristic of SPHEREx is that it will return spectra of most or all of these nebulae and of the EGOs, well over one thousand spectra in all. In addition to the shock diagnostics discussed above, the SPHEREx wavelength range encompasses Paschen and Brackett lines diagnostic of gas ionized by embedded massive stars; helium emission lines which might arise from hydrogen poor planetary nebulae or Wolf-Rayet stars; and PAH emission at 3.3 μm which could arise at the interface between a nebula and adjacent neutral material. Thus we can anticipate a treasure trove of nebular spectra from SPHEREx observations of these families of compact nebulae, spectra which for one object, might bolster and refine a identification, but, for another, demonstrate a highly unusual or perhaps previously unknown type of nebula in the galaxy.

3.5 Mapping Dust Variations

Many galactic and extragalactic astrophysical objects and processes are affected by dust. It is thus important to know the composition of dust, the shape and size distribution of dust grains, and the physical and chemical processes that form, modify and destroy dust. Much of the dust is formed in the ejecta of evolved stars: AGB stars and supernovae. The type of dust produced is set by the conditions and composition of the ejecta. Carbon-rich shells produce graphite, and aliphatic and aromatic soot-like materials, while silicate dust is formed in oxygen-rich shells. After ejection into the diffuse ISM, a hydrogen-rich surface layer may be formed, balanced by hydrogen detachment by UV photons. In dense clouds, grain surfaces catalyze the formation of hydrogen-rich molecules (H_2,

H$_2$O, CH$_4$, et cetera), forming icy mantles. Here, grain growth is likely accelerated by coagulation of the sticky, icy grains. Subsequently, as the grains are cycled back into the diffuse ISM or before they are incorporated into comets and planets, their icy mantles might be processed by energetic particles and radiation to form carbonaceous dust. Exploration of questions related to ice formation and evolution forms one of the central themes of SPHEREx science program; here we show that SPHEREx will address other issues related to the properties of interstellar grains.

It is evident that as a result of all the physical and chemical processes involved, dust properties should vary in space and time. The SPHEREx all-sky spectroscopic survey (0.75-5.0 μm) will enable studies of specific dust property variations across environments, for example:

- variations of the infrared continuum extinction curve

- variations in the infrared spectral characteristics of interstellar dust (due to, e.g., variations in the abundance of aliphatic carbon dust)

With these SPHEREx observations, a number of science questions can be uniquely addressed:

- is there progressive grain growth from diffuse, to dense, to protostellar environments? SPHEREx is able to trace much higher extinctions ($A_{\rm V} > 70$ mag) than is possible in the optical and UV.

- what is the origin and evolution of hydrocarbon grains and what are the processes that drive this evolution? (this question is addressed in Sec. 3.1)

The SPHEREx all sky map of extinction due to interstellar dust can be very usefully combined with the work of [168], who have produced a three-dimensional picture of the distribution of dust within ∼3 kpc of the Earth. Combining the two data sets will allow determination, for example, of whether an anomaly seen by SPHEREx in the grain properties along a particular line of sight coincides with a particular feature of the galactic geography, such as a young cluster or a supernova remnant.

3.5.1 Resolving Extinction Curves with SPHEREx

The continuous coverage of the 0.75-5.0 μm wavelength range will enable the determination of spectrally resolved extinction curves (Fig. 11) for every star in the sky, limited by brightness and by the ability to correct for the intrinsic stellar spectrum.

These empirical extinction curves enable a separation of continuum and feature extinction, which, in dense clouds, are in particular the ice absorption bands at 3 (H$_2$O), 4.3 (CO$_2$), and 4.7 μm (CO), the major focus of SPHEREx' Ice investigation, and the aliphatic features at 3.4 μm in diffuse clouds. In broad band measurements, feature and continuum extinction are combined. Also, for broad band measurements, correction for the stellar photosphere often relies on typical spectral types in the field, limiting the spatial resolution to arcminute scales, while with SPHEREx it can be done for individual stars, whose spectral type is determined by SPHEREx itself. This matters, for example, across cloud boundaries where dust modification may well take place. Previous ground-based work on spectrally resolved extinction curve measurements in this wavelength range rely on stitching together data in different atmospheric bands. The gap around 2.8 μm limits the H$_2$O ice band analysis. Ground-based observations above 4.1 μm have poor sensitivity. Broad band
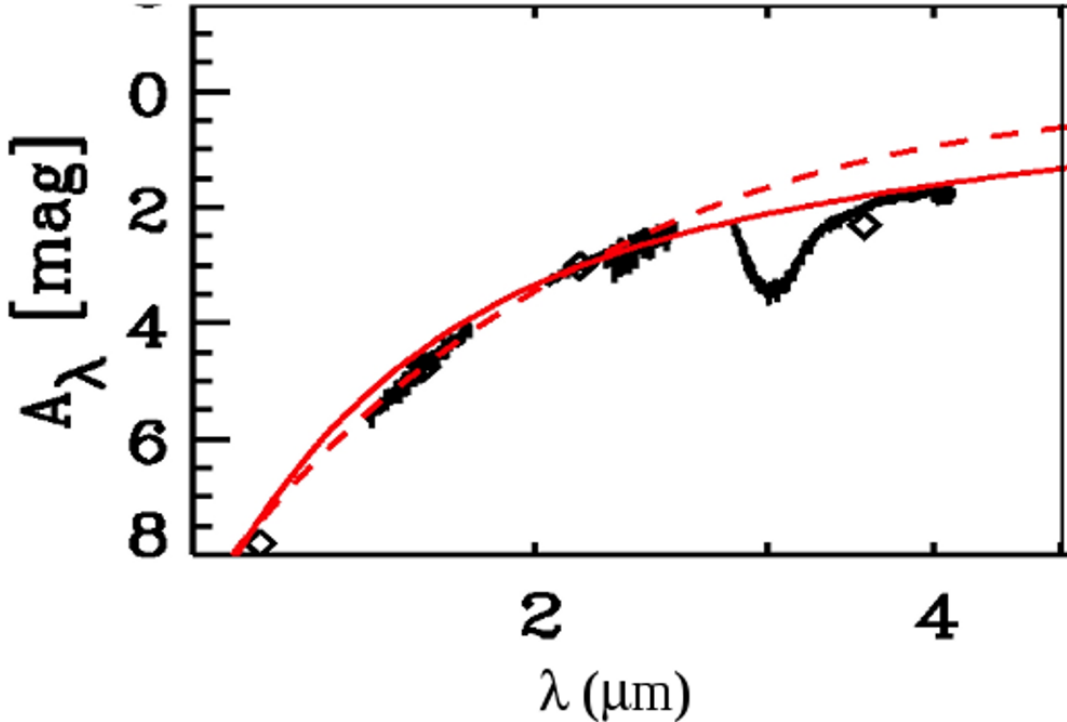
Figure 11. A spectrally resolved infrared extinction curve derived from ground-based observations of the dense core background star 2MASS J21240517+4959100 [169, in black] compared to models of [170] with R_V=3.1 [dashed red], and R_V=5.5 [solid red]. The wavelength range covered by SPHEREx is shown. This particular background star has a broad-band extinction A_K = 3.1 mag ($A_V \sim$ 28). The spectral type determined from the 2.25-2.6 μm CO overtone band head is M1 III. It has a K-band flux of 122 mJy. SPHEREx will be able to survey such objects at S/N≥100 up to $A_K \sim$ 8 mag ($A_V \sim$ 72), i.e., trace dust much deeper into the cloud core, without atmospheric gaps and uncertainties due to scaling spectra observed in different atmospheric bands.

measurements show large variations in derived extinction curves (Fig. 12), and it is unclear what the origin of these variations is, if real. It is important to note that the divergence between the curves is around 3 μm, central in the SPHEREx wavelength coverage.

3.5.2 SPHEREx Observations of Large Grain Signatures

The flattening of the extinction curve above 3 μm (Figs. 11 and 12) is a signature of a population of large (>1 μm) grains. Dust in the diffuse ISM (A_V < 1 mag) is well characterized by R_V=3.1 models [170] but that does not fit these data through dense cloud sight-lines well. Grain models characterized by much larger sizes [R_V=5.5 170, 172] or grain models including large ice grains [173] do much better. They would add 4-16% to the dust mass. Large dust grains in dense environments are also evident from the so-called coreshine [bright reflected light from dense cloud cores 174]. It has been long thought that grains grow extensively in size in dense clouds through coagulation or through ice mantle formation or both. SPHEREx can address such important questions as: how does the grain growth depend on the cloud environment, including column density, volume density,
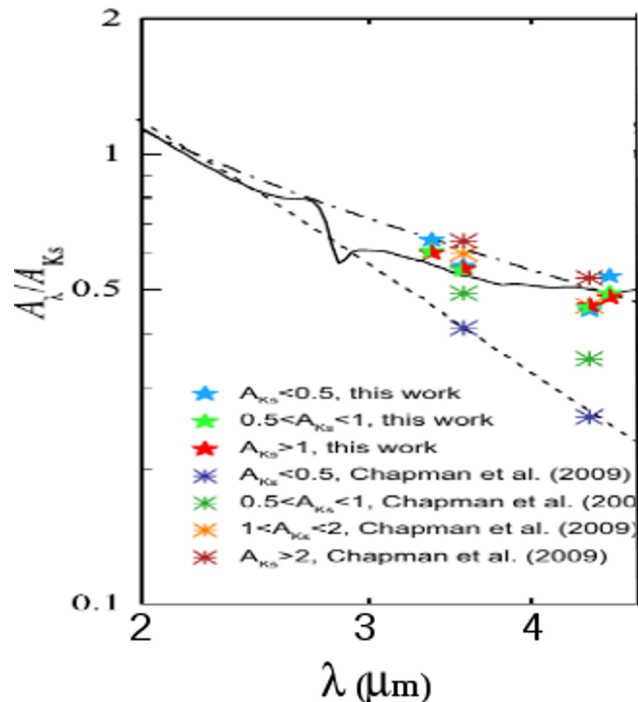
Figure 12. Broad band extinction curves from different studies and in different sight-lines (asterisks), showing much variation. The wavelength range starts at 2 μm, while SPHEREx will cover down to 0.75 μm as well. Note that SPHEREx covers the range where the different curves diverge. The solid line is a model including 4 μm-sized H_2O ice rich grains. The dotted and dash-dotted curves are for R_V=3.1 and 5.5 models [170], respectively. Adapted from [171].

and depth of the star or the line of sight within the cloud? Are the grain size and ice mantle volume (traced by the 3 μm ice band) related? Are these large grains destroyed in the environment of supernova remnants or inside HII regions?

Observationally, the presence of H_2O-rich μm-sized large grains could be distinguished by a feature in the extinction curve near 2.7 μm, caused by scattering (Fig. 12). In addition, towards reflection nebulae surrounding young stellar objects this feature appears in absorption as a wing on the short-wavelength side of the 3.0 μm ice absorption feature. It is produced by grains larger than 0.2 μm in radius and is thus diagnostic of grain growth. So far this has been observed only in a 25 arcsec beam toward Orion Molecular Cloud 2 using the Kuiper Airborne Observatory [175, 176]. All-sky spectral maps by SPHEREx offer a unique tracer of such large icy grains. SPHEREx will allow us to probe the growth of dust and the formation of ice mantles on a global scale in regions of star formation.

3.5.3 Conclusions

A SPHEREx all-sky 0.75-5.0 μm survey has the unique capability to address a number of fundamental questions about the origin and evolution of interstellar dust: is there progressive grain growth from diffuse, to dense, to protostellar environments? what is the distribution and origin of

hydrocarbon grains? SPHEREx' full coverage of the wavelength range, unhindered by the Earth's atmosphere, its spectroscopic resolution and sensitivity, and in particular its all-sky survey are unparalleled by past and other future missions.

4 Stellar Science

4.1 Normal Stars

SPHEREx will enable exquisite characterization of fundamental stellar parameters for the approximately two million Tycho stars with $V < 13$ mag. SPHEREx's VIS-near-IR spectrophotometry between $0.75 - 5.0\mu$m will cover the Rayleigh-Jeans tail of stellar spectral energy distributions (SEDs) for all observed stars as well as the SED peak for stars with $T_{eff} \lesssim 4000$ K, which corresponds to mid-K and later spectral types. These cool stars are the ones for which the models are most uncertain and which are of particular interest as exoplanet host stars (see Sec. 6.4).

Adding other databases to SPHEREx fluxes, including *Gaia's* overlapping low-resolution spectrophotometry between 330nm and 1050nm, and broad-band fluxes as blue as GALEX and as red as WISE, will yield comprehensively-measured SEDs for hundreds of thousands of stars, with bright, nearby stars benefitting from the most precise measurements. The combined data base will capture the blackbody peak for stars with $T_{eff} \lesssim 8750$ K, corresponding to spectral type mid-A and later spectral types. For bright (e.g. $V < 13$ mag) stars, which also have broad-band flux measurements from the UV (e.g., GALEX) through the near-IR (WISE), such blanket coverage will directly measure nearly all of the flux: for the late F dwarf KELT-3 [177], literature broad-band fluxes directly measure about 80% of the fitted flux, while adding SPHEREx and Gaia spectrophotometry increases the measured flux to about 98% (cf. Fig. 13). Thus, the stellar SED is exceptionally well-constrained by the data, and the best-fit effective temperatures, surface gravities, and [Fe/H] can be determined to percent or sub-percent precision. When Gaia astrometry is included, the end result will be a large catalog of stars with $V \leq 13$ and well-determined distances, bolometric luminosities, proper motions, radii, effective temperatures, metallicities, surface gravities, and extinctions. In particular, the combination of the precise distance determination from Gaia and the other well-determined parameters will yield stellar radii measured to around one percent. This is approximately the precision achieved on interferometric radii of bright, nearby stars [178], but this "spectrophotometric interferometry" method works for stars hundreds of parsecs away, versus tens of parsecs for interferometry.

Additionally, while extinction negligibly affects the SED normalization for nearby stars, moderate extinction ($A_V = 1.0$) can reduce the peak flux for hot stars by an order of magnitude (Fig. 13). Since the shape and slope of the Rayleigh-Jeans tail is relatively insensitive to changes in interstellar extinction – particularly towards SPHEREx's 5μm upper wavelength limit – SPHEREx's spectrophotometric coverage of this wavelength range enables one to measure directly the extinction in bluer bands and better constrain the bolometric flux and effective temperature for stars with $T_{eff} \gtrsim 4600$ K; hotter stars can be studied by the addition of Gaia. A very important by-product of the improved stellar parameters derived as described above is a consequence of the fact that our knowledge of the masses, radii, and densities of exoplanets discovered via the transit and radial velocity methods is no better than our knowledge of the masses and radii of the host stars. This is addressed further in the discussion below concerning synergy between Spitzer and TESS.

Finally, the overlap in coverage between SPHEREx and *Gaia* spectrophotometry provides a handle on the systematic uncertainties affecting each data set's flux measurements. With overlapping flux measurements in the 750 –1050 nm range, systematic uncertainties in the SPHEREx and *Gaia* data should introduce relative offsets in the flux measurements across this range, enabling us to quantify and correct for these systematics.
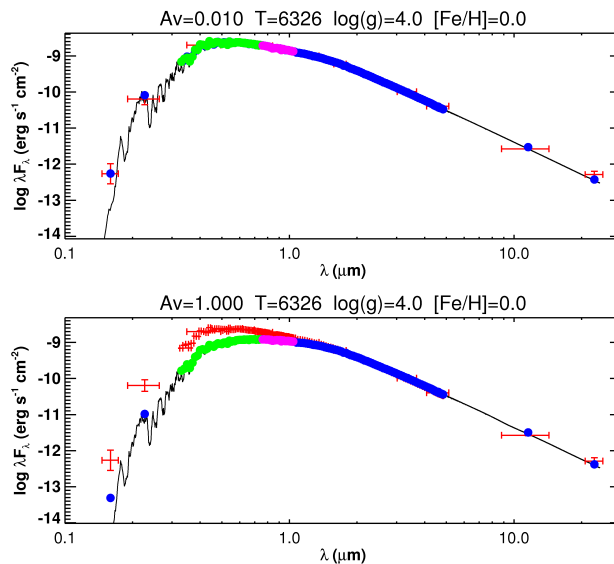
Figure 13. Best-fit model spectral energy distribution of KELT-3, adapted from [177]. The black line shows the model SED, while the red crosses show the literature broad-band flux measurements, the blue crosses show the estimated SPHEREx spectrophotometry, and the green crosses show the estimated *Gaia* spectrophotometric flux coverage; the SPHEREx-*Gaia* overlap is shown in magenta. The top panel assumes visual extinction of $A_V = 0.1$, while the bottom panel shows the same case in red and $A_V = 1.0$ in blue. The infrared SPHEREx measurements anchor the SED, enabling the extinction to be measured from the *Gaia* coverage of the extinction SED peak.

4.2   The Best and Brightest Metal-poor Stars with SPHEREx

The Brightest Metal-poor Stars: Extremely metal-poor (EMP) stars are very important for near-field cosmology and Galactic archaeology. They constrain the high redshift initial mass function (e.g., [179]), the nucleosynthetic yields and explosive deaths of Population III stars (e.g., [180]), the production of lithium from Big Bang nucleosynthesis (e.g., [181]), as well as the formation and galactic chemical evolution of the Milky Way (e.g., [182]).

However, current progress on the study of these ancient stars is being limited by their faint apparent magnitudes. High-resolution and high signal-to-noise spectroscopy is necessary to measure the stellar parameters and detailed abundances of EMP stars at visible wavelengths. Because most known EMP stars are faint, acquiring even a single spectrum can require hours of exposure time even with 6–10 m telescopes. These long integration times make the construction of large samples of genuine EMP stars prohibitively expensive, leaving their enormous scientific potential tantalizingly close yet just out of reach. Recently, [183] showed that infrared photometry can be used to efficiently identify candidate metal-poor stars through their lack of strong molecular absorption at 2.3 and

4.6 μm (Fig. 14). While the current generation of this infrared selection using 2MASS and WISE data is as efficient as other techniques used to identify EMP stars, more than half of the candidates it identifies are not metal-poor stars. It is also unable to identify the brightest and most easily studied metal-poor stars, as WISE saturates for targets with $W2 \lesssim 8$.

SPHEREx will address both issues with the current generation of infrared selection of EMPs. The current selection derives most of its power from $W1-W2$ color, which measures only the strength of absorption near 4.6 μm. The main false positives for the 2MASS- and WISE-based selection are young stars with infrared excesses produced by disks of hot dust, which can mask the molecular absorption present near 4.6 microns in the atmospheres of metal-rich stars. However, unlike the lack of molecular absorption characteristic of metal-poor stars, hot dust would also manifest itself as excess emission over a range of wavelength. SPHEREx would easily differentiate between the two possibilities and the SPHEREx spectrum would provide additional information (see Fig. 14). The saturation limit for SPHEREx is four magnitudes brighter than WISE, so infrared data from SPHEREx could be used to find all of the brightest undiscovered metal-poor stars in the solar neighborhood.

The Most Ancient Stars in the Milky Way: The most ancient stars in the Milky Way are thought to be the metal-poor stars in the inner Galaxy. (e.g., [184]). Already, two of the confirmed metal-poor stars from [183] with [Fe/H] $\lesssim -2.7$ are within the central 2 kpc of the bulge. One [Fe/H] $\lesssim -3.0$ star is approximately 4 kpc from the Galactic Center. These three stars are among the most metal-poor stars yet found in the bulge, and there is a 70% chance that at least one formed at $z \gtrsim 10$ [185]. Because of the significant reddening towards the bulge, infrared data is necessary to find these stars. SPHEREx will obtain spectra of hundreds of extremely metal-poor giants in the inner Galaxy, and their detailed abundances will provide the strongest constraints yet on the chemistry of the Milky Way and its progenitors at $z \gtrsim 10$. This is a good example of the power of the SPHEREx all sky data base.

The Mass of the Milky Way: The total mass of the Milky Way is one of the most important parameters to models of Galaxy formation and evolution. It is also difficult to measure. Accurate mass measurements require distant tracers of the halo, like metal-poor giant stars. Such tracers are rare and apparently faint, so blind searches are extremely inefficient. On the other hand, SPHEREx data could be used to identify distant metal-poor giants at high Galactic latitude with nearly 100% efficiency. Once those stars are known, Gaia proper motions and ground-based radial velocities would provide the necessary input for the most precise mass measurement of the Milky Way that will be possible for some time.

4.3 Nearby Cool Stars and Brown Dwarfs

SPHEREx will provide complete 0.75-5.0 μm spectra of many thousands of low-mass stars and many hundreds of brown dwarfs. For known objects, having such a complete spectral library will enable the computation of accurate bolometric luminosities and effective temperatures, the testing of model atmospheres over a wide range of wavelengths sampling different atmospheric physics, and the identification of objects with clear departures from solar C/O ratios. Although SPHEREx will clarify our understanding of known low-mass stars and brown dwarfs, its discovery aspects are equally exciting. Using spectroscopy alone, SPHEREx will enable us to identify rarer objects – low-metallicity L and T dwarfs, low-gravity (young) brown dwarfs in nearby moving groups, and
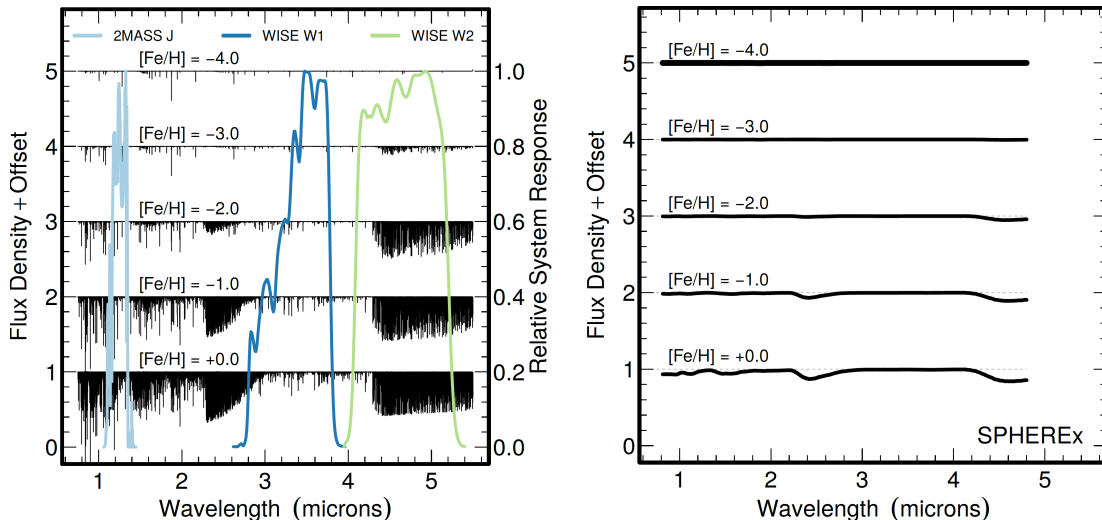
Figure 14. Illustration of the effect of metallicity on the spectra of giant stars. Metal-rich stars have strong molecular absorption at 2.3 and 4.6 microns, features that are absent in the spectrum of a metal-poor star. *Left*: the black curves are theoretical spectra with slope removed from the Gaia grid of [186] for five K stars with $T_{\rm eff}$ = 4800 K and [Fe/H] as indicated (the features are insensitive to $\log g$) along with relative system response curves (RSRs) for the 2MASS J, WISE $W1$, and WISE $W2$ bands. *Right*: the same spectra as before, now smoothed to SPHEREx resolution. While the infrared selection using only 2MASS and WISE can only make use of the 4.6 micron feature, SPHEREx would permit the use of the entire stellar SED – including the 2.3 micron feature. For that reason, SPHEREx data would enable a metal-poor star selection that is nearly 100% efficient.

perhaps even the occasional, overlooked cold Y dwarf – while not having to resort to either the color or kinematic biases present in all previous surveys for these objects.

Fig. 15 summarizes our current state of knowledge. Late-M dwarfs are dominated by bands of TiO and H_2O; L dwarfs by hydrides, H_2O, and CO; T dwarfs by CH_4, H_2O, and collision induced absorption by H_2; and Y dwarfs by NH_3, CH_4, H_2O, and H_2. SPHEREx makes available, largely for the first time, the window between 2.5 and 4.8 μm that is extremely difficult to observe from the ground. In this range, fewer than two dozen late-M dwarfs have observed spectra, and SPHEREx will provide $\sim$10,000 more. For L dwarfs, SPHEREx will increase the number from $\sim$20 to $\sim$1,000, and for T dwarfs the total will go from $\sim$10 to $\sim$200. Y dwarfs will be difficult to detect, but SPHEREx should nonetheless provide spectra of $\sim$9 of the 25 known examples, at least near their 4.5-μm peak; others may be detected by coadding spectral channels to increase the sensitivity.

SPHEREx provides complete spectra of known stars with $T <$ 4500K over the wavelength region where most of the flux emerges. Combined with *Gaia-*, *Spitzer-*, and ground-based parallaxes, these data provide an unprecedented sample with which to accurately measure absolute bolometric luminosities that, when paired with estimates of (sub)stellar radii, can be used to measure effective temperatures, providing an independent check of model atmosphere fits (e.g., [188]). These theoretical models can also be compared to SPHEREx spectra to test whether clouds best describe the emergent spectra, as has been the standard paradigm, or whether fingering convection models [189]
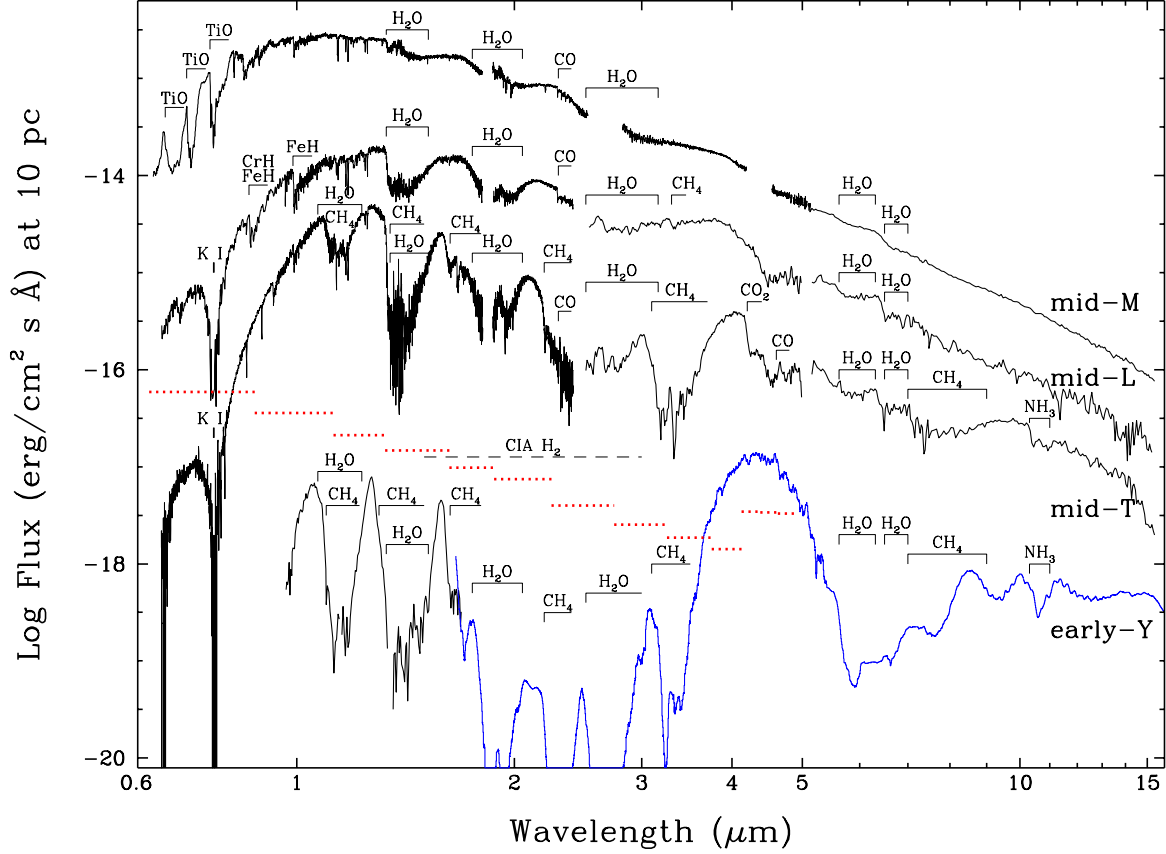
Figure 15. Representative spectra of late-M through early-Y dwarfs from 0.6 to 15 μm, adapted and updated from Figure 12 of [187]. All spectra have been scaled to a distance of 10 pc. Black spectra are actual observations taken from SDSS and Keck/LRIS for the optical, IRTF/SpeX and HST/WFC3 for the JHK bands, IRTF/SpeX and AKARI/IRC for the LM bands, and *Spitzer*/IRS for wavelengths longer than 5 μm. Blue spectra are taken from Lyon models for wavelength ranges not yet observed for the Y dwarf. Major absorption features are labeled. Shown in red are the SPHEREx 5σ detection limits at the I, J, H, K, W1, and W2 bands.

do a more adequate job. Also, these spectra can be used to check for the presence of non-equilibrium chemistry – such as the co-existence of CO and CH$_4$ – which gives insights into vertical mixing [190], and to check at a fixed spectral type for object-to-object departures from solar abundance ratios, as some of the data from AKARI have suggested [191].

SPHEREx is also capable of identifying new low-mass stars and brown dwarfs of particular interest. Low-metallicity L and T dwarfs provide excellent checks of exoplanet atmospheric theory because these atmospheres are cold yet very simple, as they lack the complex chemistry of more metal-rich objects [192, 193]. These objects can be easily selected based on their extremely blue
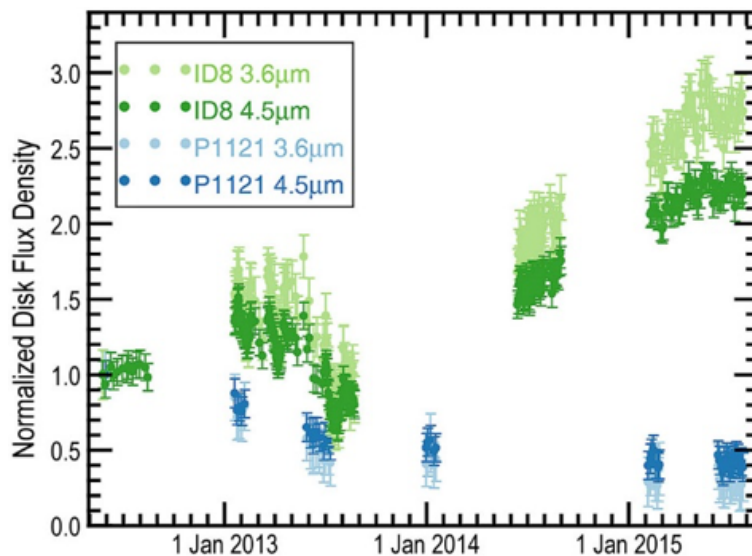
Figure 16. Spitzer data identify other planetary systems that may be undergoing collisional events similar to our Late Heavy Bombardment. Plot shows IRAC flux versus time for two of the extreme debris disk systems monitored by [196]. Both stars are members of open clusters, with ages estimated as 35 and 80 Myr.

colors across the JHK bands; the blue colors are caused by the increased relative importance of collision-induced absorption by H_2, which is strongest near 2.2 μm. Young, low-gravity L dwarfs also provide excellent checks of exoplanet models because these objects have extremely low masses and solar composition. As with the low-metallicity objects, these young objects also have unique spectral signatures because of their extremely low gravity [194]. Finally, there is also the possibility that SPHEREx will identify new, very nearby Y dwarfs that WISE has imaged but not selected due to a poorly measured W1−W2 color limit. As Fig. 15 suggests, these objects will appear in SPHEREx data only at the longest wavelengths and should be identifiable based on their unusual spectral signature combined perhaps with their motions as measured by SPHEREx or possibly from the ground.(see, e.g., the proper motion discovery of the cold Y dwarf WISE 0855−0714 with *WISE* by [195]).

4.4 Stars with circumstellar material: variability of extreme debris disks

The collisional process that creates planets leaves behind debris in the form of planetesimals and dust (extrasolar analogs of asteroids and comets on the one hand and the zodiacal and Kuiper Belt dust on the other) as illustrated in Fig. 18. Debris disks around main sequence stars were discovered by IRAS, and were immediately recognized as indicators of at least the first steps in the planet formation process, because the dust particles they contain are much larger than interstellar grains. In addition, the particles in debris disks have only finite lifetimes and must be replenished, presumably by collisions between rocky bodies and evaporation of comets orbiting the stars. Debris disks have been extensively studied by infrared space facilities and, with the prevalence of exoplanets demonstrated by Kepler, we study debris disks not only because of their intriguing properties but also because they hold clues to the nature of the exoplanetary systems which they occupy. Debris disk studies have concentrated on wavelengths longward of $\simeq 10$ μm because the disks generally

appear to contain dust no warmer than $\simeq$ 300K and because the contrast relative to the stellar photosphere increases with wavelength. However, recent Spitzer observations of extreme debris disks at 3.6 and 4.5 μm have returned striking results which SPHEREx will build upon. Extreme debris disks are systems with $L_{dust}/L_\star \simeq 0.01$, about two orders of magnitude greater than what had previously considered to be a bright debris disk. The brightness of the debris disk simply reflects the amount of dust orbiting the star, so these systems are unusual in having both a large amount of circumstellar dust and having dust warm enough to radiate significantly shortward of 5 μm. Several such disks have been identified orbiting stars younger than $\simeq$ 100 Myr, and found to have one other unusual property, which is that their infrared radiation shows marked variability (Fig. 16) on $\simeq$ 1 year time scales. At the same time, the optical radiation from the stars shows little or no variability, so the infrared variability must result from changes in the amount of dust orbiting the star, or in the visibility of the dust.

These and other extreme debris disks vary much more rapidly than predicted for evolutionary models in which the dust in debris disks result from a gradual collisional cascade. Instead, the authors postulate that the variability results from major collisions between two large bodies in which some of the colliding materials might actually be vaporized and then condense rapidly into small particles, degraded collisionally into the particles seen in the infrared, which are blown out of the system but not replenished as they would be in the case of a gradual collisional cascade (e.g., such as the silica-rich but photometrically stable HD 172555 disk system, [197, 198]). The star ID8, in the young (35 MYr old) cluster NGC2547, hosts the most dramatically variable debris disk (Fig. 16). Meng et al. estimate the mass of the disk to be at least that of a $\simeq$ 180km diameter rocky asteroid (Fig. 17).

As illustrated in Fig. 17, truly titanic collisions may be needed to produce the dust clouds required to account for the variability of the extreme debris disks. Several such collisions are thought to have taken place in the first $\simeq$ 100 Myr of our Solar System, and others may have been triggered in tandem with the Late Heavy Bombardment (LHB) which caused comets and asteroids to rain down on the terrestrial planets when the Solar System was 600 to 800 Myr old, leaving the plethora of craters seen on the Moon today (see Sec. 5.4 for more detail of the LHB). At least one disk, that surrounding the ~1.4 Gyr old F2V star Eta Corvi, is thought to have been created by an LHB [199, 200]), and the extreme Kepler lightcurve system KIC 8462852 may be just starting one, as the best explanation for the time variable spectrophotometric observations of the system remains the close passage and breakup of a > 100 km radius KBO by the primary star [201–203].

It has been suggested that such extremely dusty and perhaps variable stars may constitute up 1% of young stars in the solar neighborhood [204]. SPHEREx has the sensitivity to detect many of them and an appropriate time cadence to assess their variability. Of course, a main sequence star which shows excess emission due to dust shortward of $\simeq$5 μm will be interesting even it is not observed to vary, as the short lifetime of the dust suggests an active exoplanetary system even if it is not variable over one or two years [205]. Particularly interesting candidates could be identified for JWST follow up while SPHEREx refines our understanding of the statistics of their occurrence. The SPHEREx census will test the importance and frequency of such violent events in the early stages of the planet formation epoch and also determine whether the history of our own Solar System stands out or fits in with that of many other stars.

Figure 17. Artists conception of a collision between the Proto-Earth and a Mars-size body. It is thought that a collision like this when the Earth was only ~50 Myr old may have produced the Moon. Dust produced in collisions close to this in this scale appear to be required to account for the variability of the infrared emission from extreme debris disks.

5   Solar System Science

5.1   Executive Summary

SPHEREx has high potential for solar system science. Numerous solar system objects will be in the viewing zone during the 2 year lifetime of the survey. In fact, not only will these objects be available for scientific analysis, but many, mainly asteroids, will have to be removed from the data for SPHEREx to perform the primary astrophysical science goals of the mission. By canvassing the entire solar system for 2 years, SPHEREx has the potential not only to achieve a relatively complete sensitivity limited survey of the solar system's bodies, but also some capability to search for variation in these bodies over time. SPHEREx will also map in great temporal and spatial detail the zodiacal dust debris disk cloud that these bodies produce, providing an unprecedented level of information concerning the sources and sinks of this material.

One way to look at SPHEREx's solar system science potential is to note that its ultimate sensitivity per spectral channel is about the same as the WISE prime mission's. I.e., SPHEREx will conduct the solar system surveys "á la" WISE, but in 96 spectral channels, not 4 photometric bands. Based on the WISE results [206–213], we can expect a highly significant return for the small bodies of the solar system in terms of tens of thousands of 0.8 - 5.0 μm, R $\simeq$ 41. spectra of asteroids, of thousands of Trojan asteroids, of hundreds of comets, and of several of KBOs, Centaurs and Scattered Disk Objects (SDOs)

Another way to look at SPHEREx's solar system science potential is to realize that it will be mapping the zodiacal light over the whole sky in a sun-synchronous fashion very similar to COBE/DIRBE, but with updated detectors, a 6.2" x 6.2" pixel size (rather than 42' x 42'), and with 96 spectral channels from 0.75 - 5.0 μm rather than 4 broad photometric channels. The 2 year
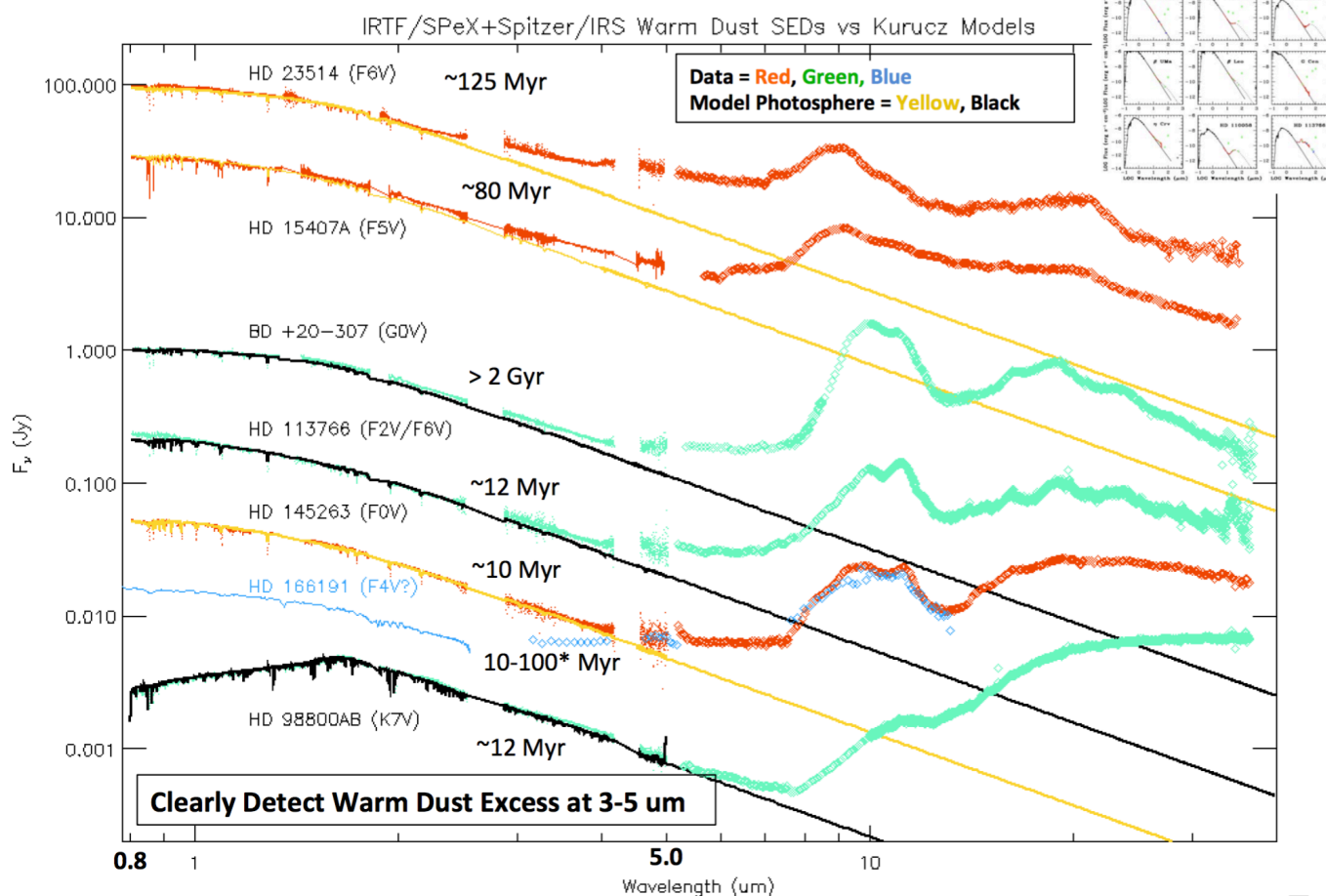
Figure 18. SPHEREx has great potential for measuring 1-5 μm spectra of debris disks. Shown are NASA/IRTF R$\sim$1000 ground based spectra of well-known disks combined with Spitzer 5-35 μm space based spectra to make combined SEDs that span wavelength ranges dominated by stellar photospheric emission, scattered light from circumstellar material, and thermal emission from circumstellar dust. SPHEREx will be able to detect excess emission due to warm or hot (T > 200 K) circumstellar dust, as seen around HD23514 and HD16191, for example, and produced by collisional grinding and giant impacts, as well as excesses due to CO (and possibly H_2O) gas found in abundance in very young systems.

survey lifetime of SPHEREx will span about the same length of time as the DIRBE cold + warm eras, but the finer spatial and spectral resolution should produce much finer maps of the cloud's structure in the asteroid belt and along comet trails and near the planets, improving on the findings of [214–216] and permitting searches for compositional signatures and variations within the zodiacal dust.

5.2 Major Solar System Science Programs

Below we list, in priority order, a number of key SPHEREx Solar System Science programs. For each program we will discuss, below the main science driver, the number of objects SPHEREx can expect to detect, and any limitations the SPHEREx survey may encounter.

1. Spectral survey of thousands of asteroids: Better reckoning of the origin and dynamical evolution of various types based on their reflectance spectra & sizes/albedos from their thermal emission. Were they formed in layered zones of the protoplanetary disk and then scattered?

2. Spectral classification of 100's of Trojan asteroids: Compare to Outer Main Belt. Were they formed with Jupiter, captured from the Outer Main Belt, or delivered in the LHB?

3. Spectral determination of cometary chemical abundances, as tracers of the composition of the proto-planetary disk. Compare KB comets vs Oort Cloud Comets. Is CO_2 the dominant molecule in carbon-ices in comets, and the fundamental carbon bearing molecule in the PPD? And by extension in all molecular clouds and hot cores? Finally, how do the comet sub-populations differ compositionally?

4. Spectral mapping of the zodiacal cloud in time and space. What produces this cloud, asteroids, comets, and/or KBOs?

5. "Follow the Water" and other key species (CO, CO_2, Organics [CH_4, C_2H_6, HCN, CH_3OH, H_2CO, PAHs], NH_3) throughout the Solar System, as critical resources for life.

5.3 SPHEREx Asteroid Spectral survey

A major question in solar system formation science today is how and where the current population of asteroids formed. In the last decade the formation of iron meteorites, remnants of planetesimal cores, have been dated to within 1 to 3 Myr after meteoritic CAI's ("Calcium Aluminum Inclusions", mineral bits composed of the stablest and most refractory metal oxides that form first out of a cooling solar abundance mixture) formed the oldest known materials in the solar system. This has been interpreted as strong evidence for a "top-down" formation of large Vesta-sized asteroidal bodies in the innermost regions of the solar system, which then underwent collisional disruption over the next 10-30 Myr to produce collections of metallic (from the core), stony-iron (from the mantle), and stony (from the crust) fragments that re-accreted into the asteroid families we see today. Many of these bodies were absorbed in the making of the terrestrial planets. Those that weren't underwent further collisional grinding, to form the smaller bodies of the asteroid families we know today. Recent spectral survey work of $\simeq$ 300 asteroids at 0.8 - 2.5 μm by [217] has shown that the asteroid belt also appears to be zoned by distance from the Sun, with the largest bodies keeping the signatures of their formation location: rockiest in the inner belt, mixed in the center regions, and most carbon and water-rich in the outer regions.

WISE performed an all-sky asteroidal survey from 2010 - 2015, detecting $\sim$ 200,000 asteroids and determining their size, albedo, and color frequency distributions. SPHEREx will be able to spectrally characterize a large number of the WISE asteroids and determine their makeup as a function of orbital location, bridging the gap between the WISE and the DeMeo surveys [217].
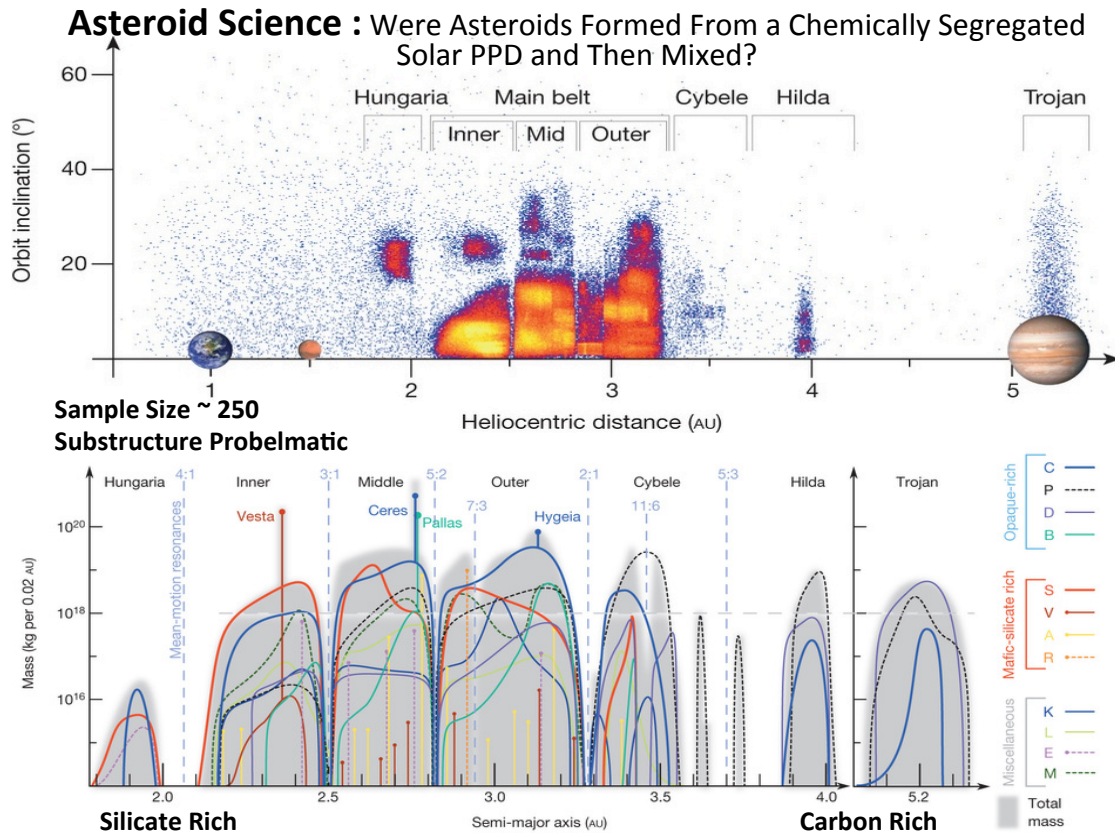
Figure 19. Relative distribution of different asteroidal compositional classes with respect to distance from the Sun according to [217]. The composition of a asteroids has been determined using 0.8 - 2.5 μm spectroscopy obtained at the NASA/IRTF observatory on Mauna Kea. Overall trends for the largest asteroids show a concentration of the most refractory rocky material closest to the Sun, with more volatile carbonaceous materials becoming more abundant in the farthest reaches of the main asteroid belt. There is an admixture of smaller bodies cutting across these general trends, though, presumably due to collisional grinding followed by impact redistribution of small fragments of the largest bodies.

SPHEREx will need to perform this asteroid survey for another reason - given the NIR brightness frequency distribution of the asteroid population and its extent across the sky, there is a few % chance in a SPHEREx observation of any given sky pixel that there will be a significant asteroidal contribution to its measured flux. To make robust measurements of extra-solar system objects, the SPHEREx team will thus have to remove any foreground asteroid contribution, naturally building up an asteroid spectral survey. Fortunately, at SPHEREx sensitivity levels most of the asteroids detected will be previously cataloged objects and asteroids would appear as unusual rogue, variable sources in SPHEREx' redundant surveys.

Even though SPHEREx can easily achieve WISE-like sensitivity levels on a fixed target, asteroids may pose challenges because of their motion and rotation in combination with the piecewise way in which SPHEREx will build up a spectrum. Thus we have conservatively estimated that
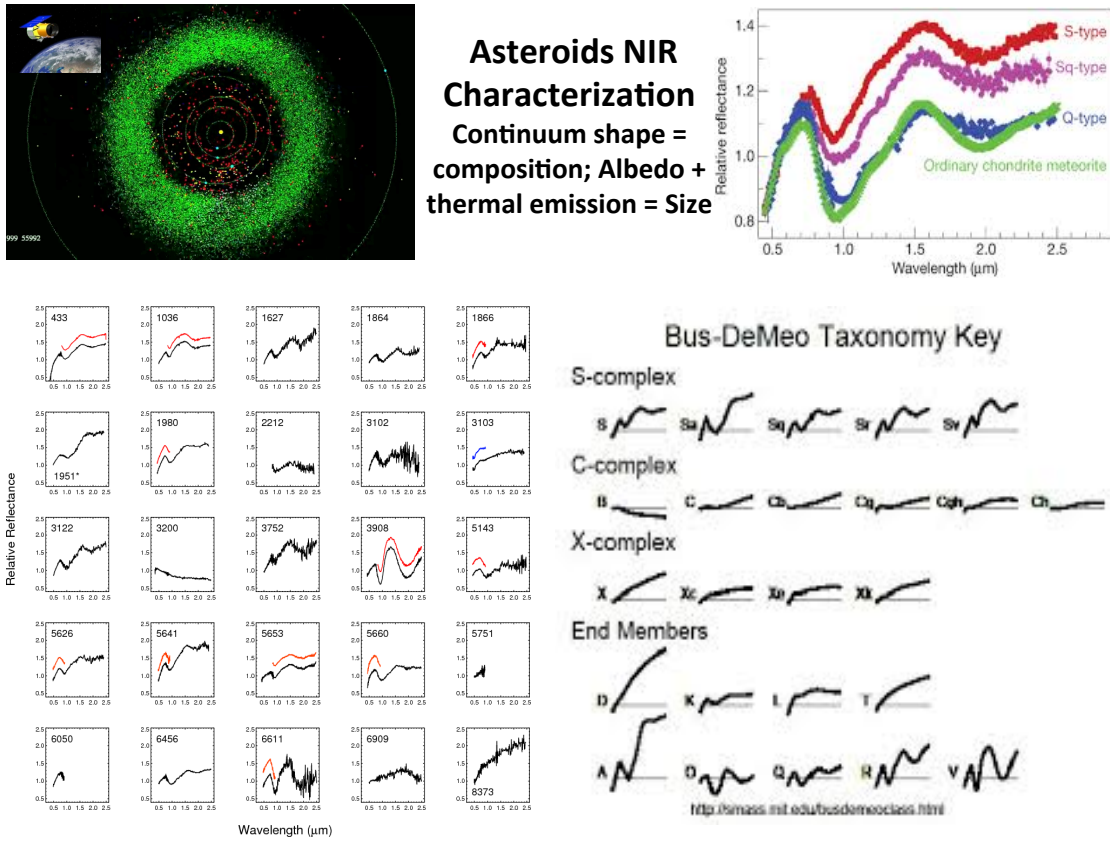
Figure 20. Illustration of how asteroids are compositionally classified using near-infrared reflectance spectroscopy. Shown, starting in the upper left and moving counterclockwise are: the WISE spatial distribution of main belt asteroids (MBAs); 0.8 - 2.5 μm spectra for 25 asteroids taken from the NASA/IRTF 3m on top of Mauna Kea; Bus-DeMeo [218] spectral templates for different classes of asteroids, referenced to laboratory measurements of meteorite samples; and in the upper right hand corner an detailed comparison of 3 closely related rocky asteroids, showing the subtle differences in the olivine and pyroxene absorption features that sets them apart. The dominant distinguishing spectral reflectance features observed are the 1.2 μm and 1.9 μm olivine absorptions, the 1.3 μm pyroxene absorption, and the broad shallow 0.8 - 2.5 μm continuum reddening due to carbonaceous material.

SPHEREx will return useful data on tens of thousands, and not $\sim 2 \times 10^5$ asteroids, as WISE has done. Even so, robust spectral characterization from 0.75-to-$\sim 5 \mu$m of tens of thousands of asteroids will be a major scientific advance over the $\sim$500 asteroids measured over the last 3 decades.

5.4 Trojan & Greek Asteroid Survey

In a similar fashion, SPHEREx will naturally observe and detect asteroidal bodies located in the L4 and L5 resonances of Jupiter, the so-called Greek and Trojan asteroids also known as "Jupiter Trojans". Characterizing these objects will be a natural offshoot of the main belt asteroid survey. Even though their total number is predicted to exceed the number of MBA's, only a fraction of these objects have been studied spectroscopically in the NIR. [219] studied 1742 Jupiter Trojan Asteroids

Trojan Asteroid NIR Spectroscopy
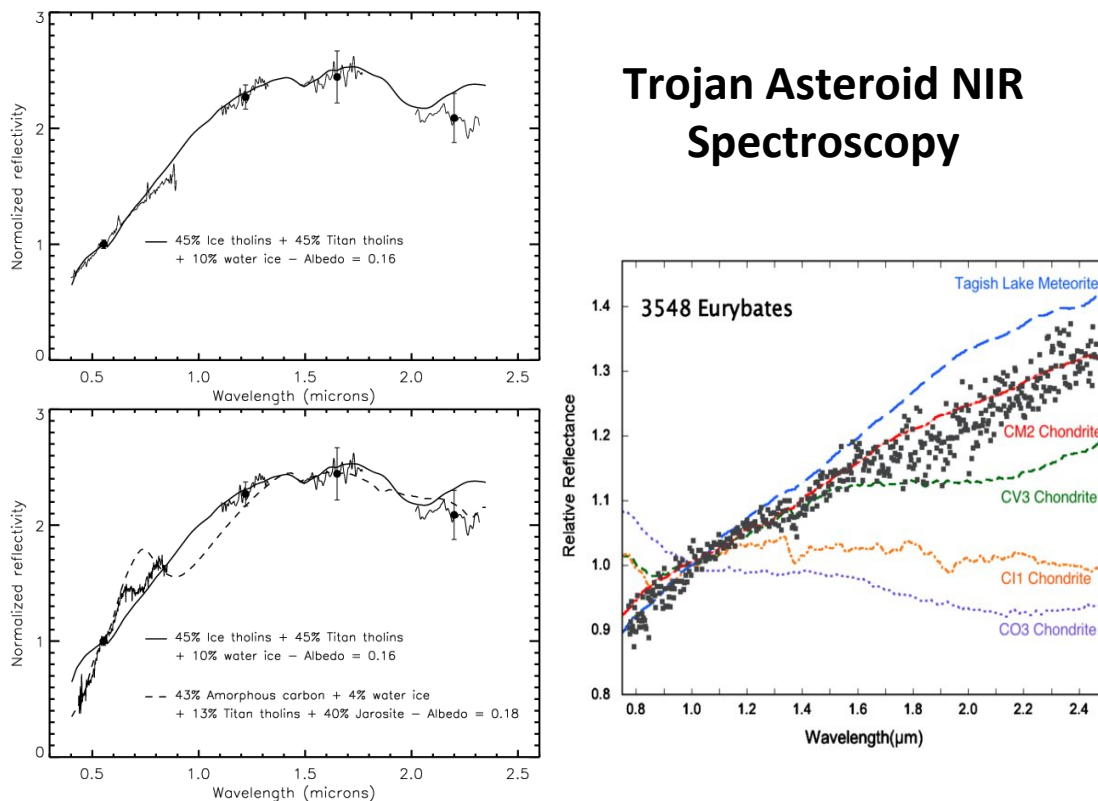
Figure 21. *Left*: Example of near-infrared spectral characterization of Trojan and Greek asteroid composition. The spectra are in some ways similar to the outer MBA spectra, as they are dominated by features due to large amounts of very primitive carbonaceous material (here modeled by laboratory grown "tholins"), but as they are located at ~ 5.2 AU outside the water ice line, they also show important features due to water ice and highly hydrated minerals (e.g., Jarosite, $\mathrm{KFe_3^{3+}(OH)_6(SO_4)_2}$) not seen in the MBAs. *Right:* Comparison of one of the larger Greek asteroids' reflectance spectrum, 3548 Eurybates, to meteorite fall spectra. The best match is to a CM2 spectrum, suggesting that like the Murchison meteorite, these objects are very primitive and carbon and organics rich ($\sim 20\%$ by weight) and have experienced extensive alteration by water-rich fluids ($\sim 10\%$ by weight).

using the WISE spacecraft broad-band photometry, and found 3.4 μm albedo differences between C & P-spectral-type and D-types. SPHEREx will provide a better understanding of the compositional causes of this color correlation. SPHEREx should be able to obtain good spectra of hundreds of Trojan and Greek asteroids; they move across the sky more slowly and predictably than the main belt asteroids and should present fewer observational problems.

The importance of SPHEREx information about the composition of these bodies is bound up in our current understanding of the migrational history of the solar system. The NICE model [220, 221] has predicted that the Kuiper Belt was disrupted some 600 - 800 Myrs after the CAI and iron meteorite formation, when Jupiter and Saturn moved into a 2:1 resonance which forced an inward

migration while Uranus and Neptune moved outward. This planetary migration greatly disrupted the orbits of the Kuiper Belt planetesimals, scattering some 99% of them inward or outward in the solar system and creating the system-wide Late Heavy Bombardment, while sweeping up a small fraction ($\sim$100 are known today) into mean motion resonances with Neptune (e.g., the Plutinos). It is thought that while this was happening, some of the KBOs scattered inward would be captured into the stable Lagrangian points around the giant planets. Thus comparing the makeup of the Jovian Trojan population to what is known about KBOs (and other purportedly captured KBOs, like Saturn's moon Phoebe and Neptune's moon Triton) is an important test of this model for solar system development. Other possibilities for the Trojans' sourcing are capture of outer main belt asteroids, or formation of the Trojans in situ from the PPD as Jupiter formed. SPHEREx will be able to test each of these hypotheses by comparing the Trojan spectral results to its MBA spectra catalogue. SPHEREx would also be able to compare these Jupiter Trojan spectra to spectra of more distant asteroidal bodies linked with the KBOs, like the Centaur and SDO populations. SPHEREx is likely to measure several of these bodies.

The nature of the Trojan and Greek asteroids is thought to be such an important issue that in 2015 NASA selected a proposed tour of 5 of these bodies for a Phase A Discovery mission study.

5.5 Comet Chemical Abundance Survey

Comets, formed within the first Myr of the solar system's lifetime, are thought to be the most primitive bodies left over from the Proto-Planetary Disk (PPD) era. They are leftover relics from the era of planetary formation that have failed to aggregate into a planet (or looked at another way, survived the era of violent early aggregation). There are two main reservoirs of comets known today in the solar system: the Kuiper Belt and the Oort Cloud. The Kuiper Belt comets are small icy bodies that formed at the outer edges of the PPD, where there was too little mass density to form another planet; looked at another way, the PPD had to end somewhere, and in its regions of lowest density planetesimals accretion was slow and truncated. These objects are relatively well clustered around the plane of the ecliptic with low inclinations (modulo the objects scattered by Neptune as it migrated outward during the LHB), and exist in a radial zone extending out to $\sim$50 AU from the Sun. We observe them when they become scattered inward into the giant planet region by galactic tides and passing stars, becoming first Centaurs and then finally short period comets. The Oort Cloud comets, found in a roughly spherical distribution from 10^3 to 10^5 AU, were counterintuitively formed inside the Kuiper Belt in the giant planet region, as the feedstock for the nascent giant planets; they represent the population of objects that had near misses to the growing giant oligarchs in the first 1-10 Myr of the solar system, and rather than accreting or being thrown into the Sun or out of the system entirely, they were scattered into highly elongated, barely bound, Myr orbits. One of the holy grails of comet science over the last 2 decades has been to search for compositional differences between the Kuiper Belt and Oort Cloud comets, as a signature of radial chemical gradation in the PPD. SPHEREx will observe large enough numbers of comets to start to fill this data gap, particularly if more than the expected number of Oort Cloud comets appear during its 2 year mission.

The search for PPD chemical signatures in comets has produced another very interesting result. Cometary bodies are composed of $\sim 1/2$ icy volatiles and $1/2$ rocky refractory materials, with the ices being dominated ($> 80\%$) by H_2O ice [222–225]. The most important ice species after water
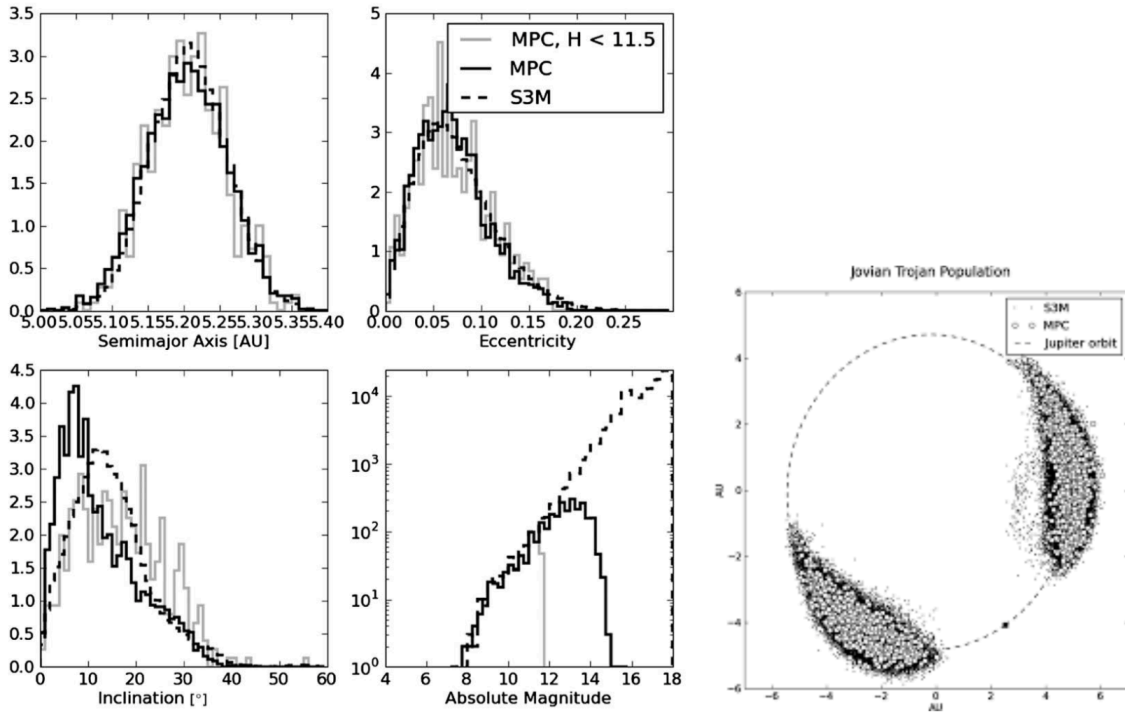
Figure 22. *Left:* Estimated brightness and orbital frequency distributions for the Trojan and Greek asteroids, after [219]. There are hundreds of known Trojan asteroids that SPHEREx will be able to characterize spectrally for the first time during its 2-year mission. *Right:* Spatial location of the Greek asteroids leading Jupiter in its orbit around the L4 resonance (∼60 deg. in the prograde direction) and of the Trojans trailing Jupiter in its orbit around the L5 resonance (∼ 60 deg. in the retrograde direction). Jupiter is the small dot at (2.3, -4.2) AU. Note that the Trojans and Greeks are safely removed from Jupiter and each other, so that there is no likelihood of scattered Jovian light causing problems with the SPHEREx measurements, while at the same time it will require a dedicated survey like SPHEREx to sample the spatially extended swarms well.

are CO and CO_2 [226], with minor flavoring due to methane, ethane, formaldehyde, methanol, and ammonia. Until 2012, when Ootsubo et al. used the Akari satellite to observe 18 comets from 1 - 5 μm at R∼50, it had long been thought that CO was the fundamental C-bearing icy reservoir; but we now know that while CO_2 ranges from 5 to 25% vs. water in abundance in comets, CO can vary from 0.1 to 30% [227, 228]. Thus CO_2 may be the true leader of the C-bearing family.

Much work has been done in the last 5 years to quantify the amount of C-bearing gas in comets. As emission lines from these species are best detected from space (and CO_2 is detectable only from space) owing to the Earth's atmospheric absorption, space-based platforms are the best-equipped facilities for characterizing their production by comets. In addition to Akari, WISE and Spitzer have undertaken campaigns to identify CO and CO_2 emission in comets (cf. [207, 229]), and to characterize their production as a function of distance from the Sun and of comet orbital class. However, since both spacecraft detect the molecules' presence through broad-band photometry, it is not possible to directly differentiate between CO and CO_2 production, as both lie in the same "4.5 μm" filter. Furthermore, regarding comparison to water production, because of the variable nature of comets and the lack of the ability of these space platforms to quantify water production simultaneously,
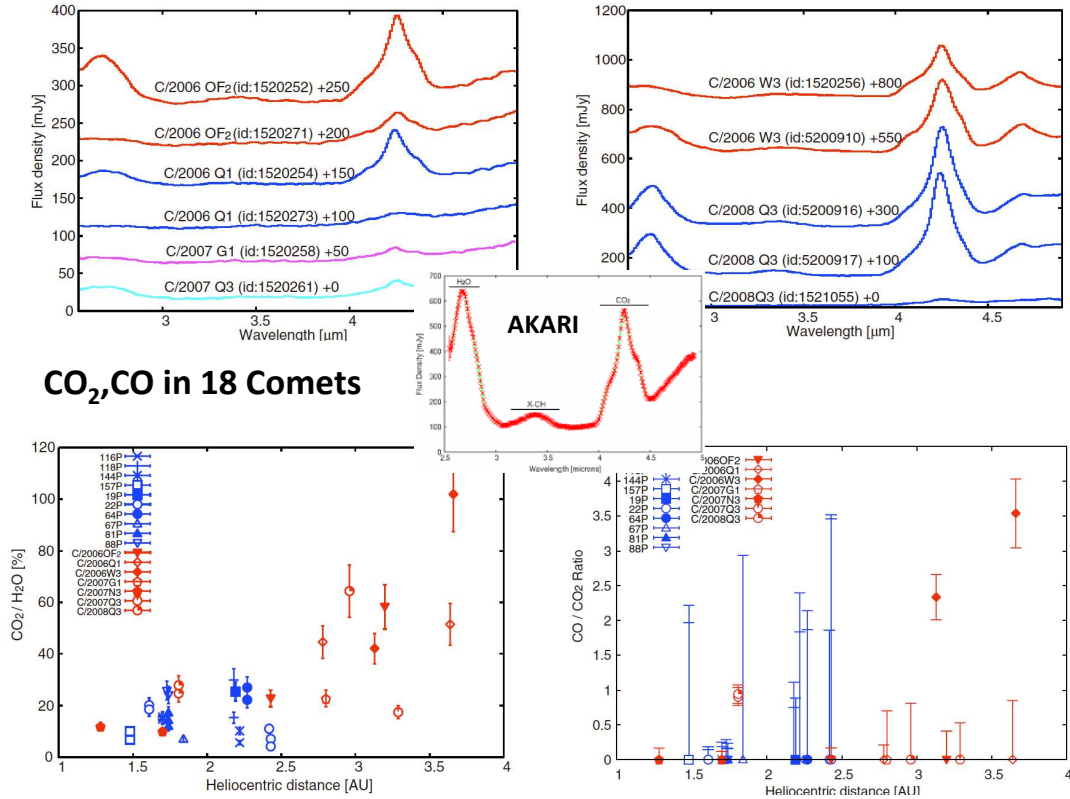
Figure 23. (*Top:*) Examples of the quality of cometary spectra from SPHEREx, after *Ootsubo et al. (2012)*. Shown are AKARI 1-5 μm R$\sim$50 spectra of 12 comets. The areas under each spectral feature are directly related to the total amount of the emitting species in the AKARI beam. The main features evinced are due to the O-H stretch in water and hydroxyl (2.4 - 2.8 μm), the aliphatic and aromatic C-H stretch in organics like CH_4, C_2H_6, H_3COH, H_2CO (methane, ethane methanol, and formaldehyde; 3.2 - 3.6 μm), the C=O stretch in CO_2 (carbon dioxide; the doublet from 4.0 - 4.5 μm centered around 4.25 μm), and the C=O stretch in CO at $\sim$4.7 μm (carbon monoxide). (*Bottom:*) Trends in the estimated CO_2/H_2O and CO/CO_2 ratios. A clear trend of rising CO_2 vs H_2O production is seen as the observed comets move outside the water ice line at $\sim$ 2.5 AU. However, trends in the CO_2/CO ratio are hard to distinguish. SPHEREx will be able to greatly improve over AKARI in the 4-5 μm range while observing $\sim$ 100 comets because of its much colder optics bench, which will remove the confusion in previous 4.5 um photometric surveys (e.g., WISE) between flux produced by CO_2 vs CO.

placing the combined production limits of CO and CO_2 in relation to the most plentiful species produced in the inner solar system by comets is not certain. Even though the water production may be characterized from the ground, the ground-based observations are rarely simultaneous. SPHEREx will be able to detect these C-bearing species separately, as well as simultaneously with water, and other volatiles such as methane or other organics. The imaging capabilities of the spacecraft will play a special role in more detailed investigations of particular species. For example, they will facilitate the accurate measure of the dissociative scale length of CO and CO_2, a feature of the emission which

remains ambiguous (cf. [207, 230]), and so investigate the presently unaccounted physical processes which cause the shortened scale.

By performing an unbiased spectral survey of ~ 100 comets (based on the WISE detection results, [207]) SPHEREx will be able to directly expand knowledge of the quantity of CO and CO_2 in comets relative to H_2O, and so provide compositional constraints on the PPD in which they formed. SPHEREx will further provide independent estimates or constraints on the size, albedo, and activity level of these comets. Finally, there is the potential for synergy with contemporaneous planetary surveys, such as NEOCam, which have bandpasses that encompass the 4 micron CO and CO_2 features, but with much greater sensitivity. Such surveys will cover many of the same comets several times, but at different times and while the comets are at different heliocentric distances. This vast quantity of comet detections will also yield size and albedo constraints, but SPHEREx will provide the "truth" data set for the CO and CO_2 fractions seen in the thousands of comets the NEOCam survey could likely detect, and will independently check the comet sizes and albedos for the overlap sample.

5.6 Spectral Mapping of the Zodiacal Cloud

SPHEREx can address the still unsettled question of the origin of the zodiacal dust cloud, which might have contributions from comets, asteroids, and Kuiper belt objects. Our solar system contains two known debris disk regions populated by relic planetesimals in collisional equilibrium, the Main Asteroid Belt and the Kuiper Belt [231–233]. (A third region, the Oort Cloud, while filled with relic comets from the era of giant planet formation, has yet to be shown to be producing dust due to comet collisions or activity.) Using infrared profiles of the zodiacal cloud, various groups have argued for the relative amount of dust produced by asteroid grinding and family formation in the main belt vs. dust emitted from active comets and Centaurs [233–237]. The recent passage of the New Horizons spacecraft carrying the Student Dust Counter Experiment into the Kuiper Belt has shown that dust is being created by KBO collisional grinding and impact spallation. While these debris disks in the solar system are relatively sparse and low density compared to some of the well known IRAS, Spitzer, Herschel, and WISE disks, likely due to the large number of surviving planets in our system [238], they arise from the same phenomena.

Studies of the zodiacal ("zodi") cloud emission by IRAS in 1984 and COBE/DIRBE spanning 1989 - 1992 showed that the brightness depends on the elongation, time of year, and wavelength of observation. We now understand these effects as due to our vantage point moving with the Earth along its slightly inclined and eccentric orbit through a zodiacal dust cloud with its own eccentricity and tilt. Both surveys also detected enhancements of the zodi, termed "bands", associated with asteroid collisional families in the main belt (E.g. [239]). Trails of heavy dust particles were also detected in association with cometary activity [240–243]. Cometary dust emission has been known for centuries, and dynamical estimates of the dust input to the zodi suggest that the largest amounts come from the highly gravitationally bound short period comets [233, 244, 245]. In the last few years, HST has directly imaged asteroid-asteroid collisions (e.g. [246]). ISOCAM MIR spectral measurements of the zodi emission show silicate emission features similar to those of cometary dust grains [247], while NIR CIBER rocket flight measurements show absorption features akin to stony asteroid surface reflection spectra ([248]).

The IRAS and COBE surveys were conducted using photometry at very coarse spatial resolution, while the ISOCAM and CIBER observations were taken for a few minutes over small patches of sky. SPHEREx will provide detailed maps of the zodi emission in unprecedented spatial and spectral detail over 2 years, allowing for in-depth searches of the sources of the cloud amongst the asteroid families and active comets. Like the asteroid survey described above, mapping the zodi is also a SPHEREx science goal of high priority, as measurements of diffuse emission from extra-solar system phenomena must contend with the zodiacal light foreground.

5.7 Follow the Water & Key Ices Throughout the Solar System

The final two SPHEREx solar system science programs we discuss involve taking an inventory of key astrobiological components (e.g. H_2O, CO, CO_2, Organics [CH_4, C_2H_6, HCN, CH_3OH, H_2CO, PAHs], NH_3) throughout the solar system. NASA has used the observation, that life as we know it on Earth is only freely metabilizing if liquid water is present, to motivate its "Follow the Water" methodology for searching for extraterrestrial life in the solar system. Similarly, sources of organic materials are required for life on Earth, as are sources of nitrogen; NH_3 is also explicitly broken out in the list above as it could possibly serve as a polar hydrogen-bonding alternative solvent to H_2O in other environments. This program is broad, in that it will attempt to find the relative abundances of these species on every body in the solar system. But it also contains some focused sub-programs where SPHEREx can greatly help as the most sensitive NIR spectrometer above the Earth's atmosphere, by specifically searching for the H_2O (e.g., the 2.7 μm complex), CO_2 (4.23 μm), CO (4.67 μm) and CH_4 (3.3 μm) signatures that are strongly blocked for ground based telescopes.

An example of the type of discovery which SPHEREx might make is provided by the discovery of water emission from the dwarf planet Ceres, reported by HST [227] and Herschel [249]. Results from the DAWN mission argue strongly that Ceres is a highly altered world, rich with water ice, ammonia, clays, and surface evaporites, but water has been seen only in the Ivo crater region, and it is not clear if Ceres is now a dead and frozen world. Evidence for the presence of water-bearing or water-altered species and organics are also found in a variety of other asteroid spectra, especially in the 2-4 μm region have been identified (cf. [250, 251]). SPHEREx, obtaining the spectrum of every body which crosses its path, has the potential to discover water and other astrobiologically interesting molecules in numerous asteroids, while it is also studying these same molecular species in comets. A thorough inventory of solar system ices and organics is of great scientific interest, and it also connects directly to one of SPHEREx main scientific goals, which is to study the evolution of icy materials from the interstellar medium into protoplanetary and planetary systems.

6 Synergies with other NASA programs

6.1 JWST and SPHEREx Synergies

The James Webb Space Telescope (JWST) is NASA's next major space observatory, and scientific, technical, and schedule considerations conspire to make SPHEREx an important synergistic partner. JWST is the perfect near–mid-IR sequel to HST and Spitzer [252]. SPHEREx will be the perfect 0.75-5 μm *all-sky* object finder for JWST, and play a critical role in the absolute flux calibration for JWST at 0.7–4.8 μm. SPHEREx' wavelength range is totally encompassed within that accessible to JWST, so the initial releases of the SPHEREx data (in 2021-22) and the all-sky catalogs (in

2023) will provide an invaluable catalog of scientifically interesting sources for full investigation with JWST. JWST observations are slated to begin in the Spring of 2019 with a planned five year lifetime; this already provides significant schedule overlap with SPHEREx, which will increase considerably if, as seems very probable, JWST operates beyond its current five year horizon.

At the cost of a SMEX mission, SPHEREx's all-sky 0.7-5.0 μm spectral coverage is a great bargain in preparation for JWST, and will result in truly maximizing the enormous investment already made in JWST: Any (rare) classes of objects that are discovered by SPHEREx which JWST must follow-up on during its expected lifetime, will be observed by JWST only if SPHEREx flies well before JWST expires. We give a couple of examples of such objects in this document, and discuss broad areas of scientific synergy.

6.1.1 JWST–SPHEREx Synergy: Ground-Truth Calibrations

As of 2016, the JWST Project is planning to use its four instruments for science parallels. This is currently being implemented for the most-used JWST instrument combinations. JWST will therefore be able to provide the perfect grism+imaging calibration data for SPHEREx (and also for WFIRST): JWST NIRCam 0.7–5 μm images to AB$\lesssim$29-31 mag and NIRISS 0.7–2 μm grism spectra to AB$\lesssim$27-28 mag will critically help to disentangle the multi-band SPHEREx database in crowded deep fields. Over very small FOV's at least (5–10$'$ after some mosaicking), JWST will therefore be able to provide the ground truth for faint-object broad-band photometry and slitless spectra about 10 mag deeper than what SPHEREx will routinely observe.

Why is this so important? Because with its 6.2" pixels, deep multi-band SPHEREx images will be confusion limited, so that an independent assessment of the exact level of object confusion is absolutely critical. JWST will provide that ground-truth in a number of very small-area but very deep and well-studied survey fields. The good news is that SPHEREx' object confusion is mathematically solvable. This is simply because the panchromatic normalized differential galaxy counts — measured over the range $10\lesssim$AB$\lesssim$30 mag and 0.2–2 μm [14], and recently also out to 500 μm [45] — converge with a sub-critical magnitude slope of $<$0.4 dex/mag in the flux range $18\lesssim$AB$\lesssim$21 mag. That is, at all wavelengths now measured with GALEX, HST, ground-based facilities, Spitzer, WISE, and Herschel, the normalized differential galaxy counts permanently reach a sub-Olbers slope for AB$\gtrsim$19 mag, or somewhat fainter. Stated differently, the 0.75–5.0 μm galaxy counts in the flux range $18\lesssim$AB$\lesssim$21 provide most of the measured integrated Extragalactic Background Light (iEBL). Hence, most discrete 0.7–5.0 μm object fluxes fainter than AB$\sim$19–21 mag add relatively little additional flux to the total Extragalactic Background Light. While 0.75–5.0 μm objects fainter than 19–21 mag will occasionally confuse the SPHEREx fluxes for brighter foreground objects, this will happen in a manner that is statistically correctable. In summary, [45] show that at all wavelengths 0.1–500 μm, the EBL integral clearly converges (*i.e.*, Olber's paradox is no longer relevant), and as a consequence, SPHEREx object confusion for unresolved background objects at AB$\gtrsim$19 mag can be statistically addressed and corrected for at 0.75–5.00 μm. JWST will add the essential ground-truth data to AB$\sim$29 mag from 0.75–5.0 μm in selected fields to test this in SPHEREx images of the same fields. The ultradeep JWST images can then simply be used to measure the converging integral in each SPHEREx beam beyond the SPHEREx detection limit, and verify that the statistical confusion correction is as computed from [45] and [14, 253].
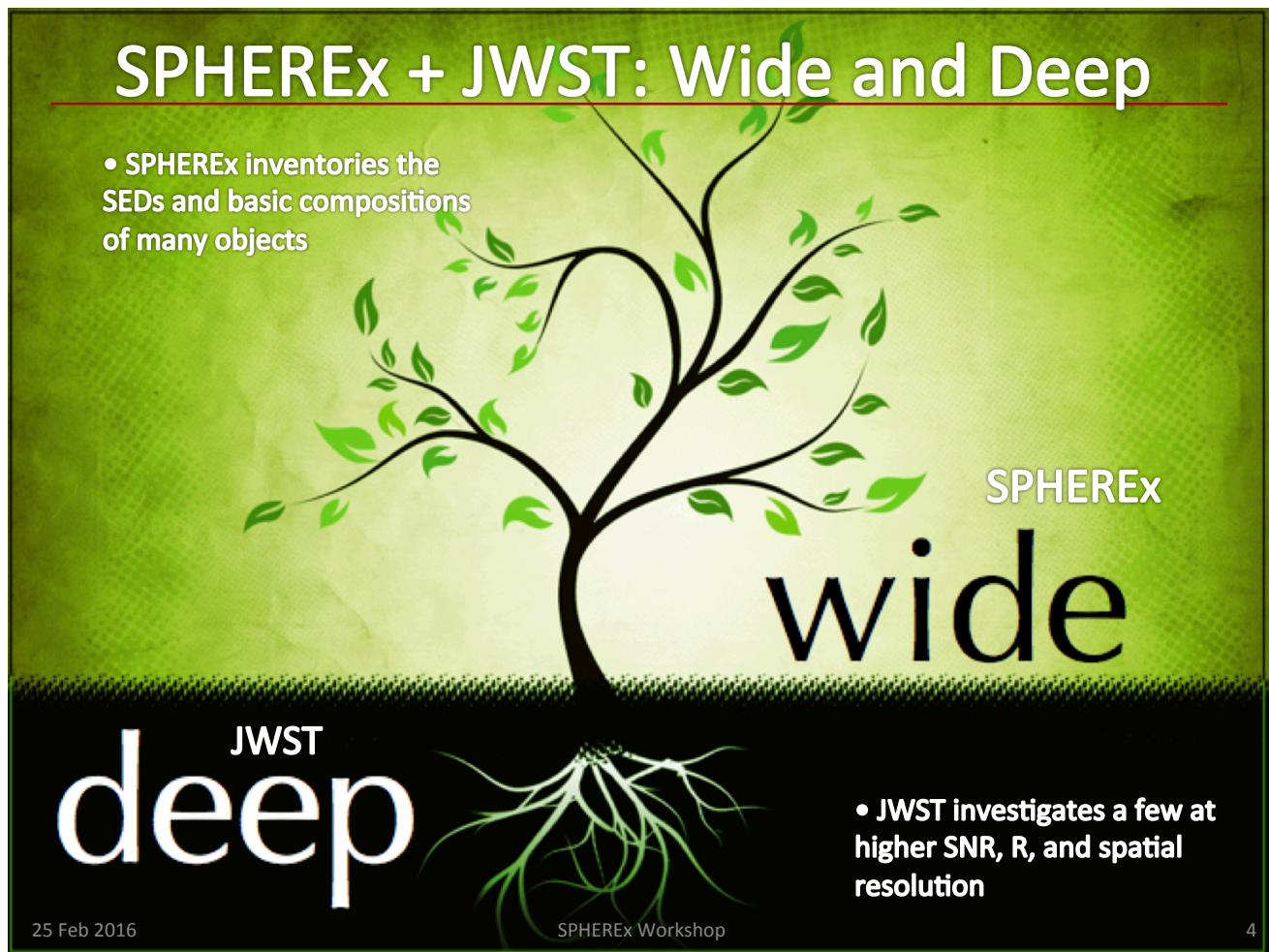
Figure 24. Illustration of the synergies between SPHEREx and JWST.

SPHEREx and JWST are two very different missions, but they will both play major roles in advancing our knowledge of galactic science, including JWST's two major galactic science themes: *Birth of Stars and Planetary Systems* and *Planets and the Origins of Life* [e.g., see 254].

Their differences also complement each other very well. SPHEREx is a moderate-aperture single-mode observatory that will provide R $\sim$ 50 resolution spectra over $\lambda = 0.75 - 5.0$ μm for every point in the sky JWST is a large-aperture observatory with 4 separate high sensitivity and high spatial resolution science instruments having specialized modes, each covering some part of JWST's 0.6 – 28 μm wavelength range. SPHEREx surveys the entire sky efficiently to moderate depth, while JWST is optimized for very deep exposures; its large overheads ($\sim$ 45 min for slew, guide star, and target acquisitions) make JWST observations inefficient for all but the faintest objects.

These characteristics produce a natural division: SPHEREx goes wide, inventorying the SEDs

and basic compositions of many objects in the galaxy and beyond. JWST goes deep, studying many fewer objects but with much higher spatial resolution, sensitivity, and spectral resolution as well. SPHEREx data will be used to evaluate statistically the bulk characteristics of whole classes of objects, while JWST data will give detailed insights into the physical and chemical workings of individual and modest groups of faint objects. JWST can also follow up on objects identified by SPHEREx as having unusual and intriguing characteristics. For example, JWST can obtain higher spectral and spatial resolution spectroscopy of objects with unusual ice spectra which might be suggestive of stronger than expected isotopically shifted species or atypical elemental abundance ratios.

Much galactic science would benefit from a complete SPHEREx $0.75 - 5.0\ \mu$m survey plus higher sensitivity and resolution JWST observations of a smaller number of select objects at SPHEREx or perhaps longer wavelengths. These include observations of dark cloud extinctions, Class 0 and I protostars, circumstellar protoplanetary and debris disks, interstellar radiation diagnostics (i.e., PAH emission), planetary nebulae, T-class field brown dwarfs, stellar populations, and potentially other objects as well. Table 2 illustrates the typical numbers and sizes of some of these objects. Although some sources seen by SPHEREx might saturate some JWST observing modes, SPHEREx' dynamic range is high enough, and JWST's instruments versatile enough, that millions of SPHEREx detections will be readily observable by JWST. The expected annual cadences of both JWST calls for proposals and SPHEREx data releases should allow SPHEREx follow up observations to be proposed during the first year of the SPHEREx mission and annually thereafter.

Table 2. Potential targets for SPHEREx + JWST Galactic Studies

Objects	Number	Size(")	Comments
Dark Cloud Cores	$\sim$50	$\sim$60	Extinction studies for structure and ices
Class 0/I Protostars	500	$0.5 - 2$	$F_\nu \sim 1$ mJy; extinctions and ices
Protoplanetary Disks	1000	< 1	$F_\nu \sim 10+$ mJy; SEDs and ices
Debris disks, PNe, BDs...	Many	pt. $- 60$	Many object types
Solar System Giant Planets	4	$4 - 50$	Full disk observations
Small Solar System Bodies	> 100	< 1	Surface compositions

6.1.3   The near–IR Spectral Energy Distribution of Galaxies

Fig. 25 shows examples from an array of combined Simple Stellar Population (SSP) Spectral Energy Distributions (SEDs) from [255] for different ages, solar metallicity, and zero extinction, as applicable for early-type galaxies in groups or clusters at z$\lesssim$0.5, which SPHEREx will observe in very large numbers all across the sky (see § 2). Note that irrespective of age, nearly all SEDs older than 10 Myr show a peak around $\lambda\sim$1.7 μm and a rapid decline at $\lambda\gtrsim$2.33 μm. The Zodiacal sky-brightness at L2 similarly declines rapidly at $\lambda\gtrsim$2.33 μm for a 5 Gyr old star (*i.e.*, the Sun). As a consequence, for any reasonable old lensing-galaxy SED, the black box indicates that the sweet spot in JWST NIRCam sensitivity to lensed First Light (z$\simeq$10–15) sources occurs at λ=2.5–4.5 μm, where the Zodiacal foreground from L2 is the lowest. The best lensing clusters to magnify First Light objects with JWST will be the most massive lenses at z$\lesssim$0.5, where the K-correction from the $\lambda\simeq$1.7 μm
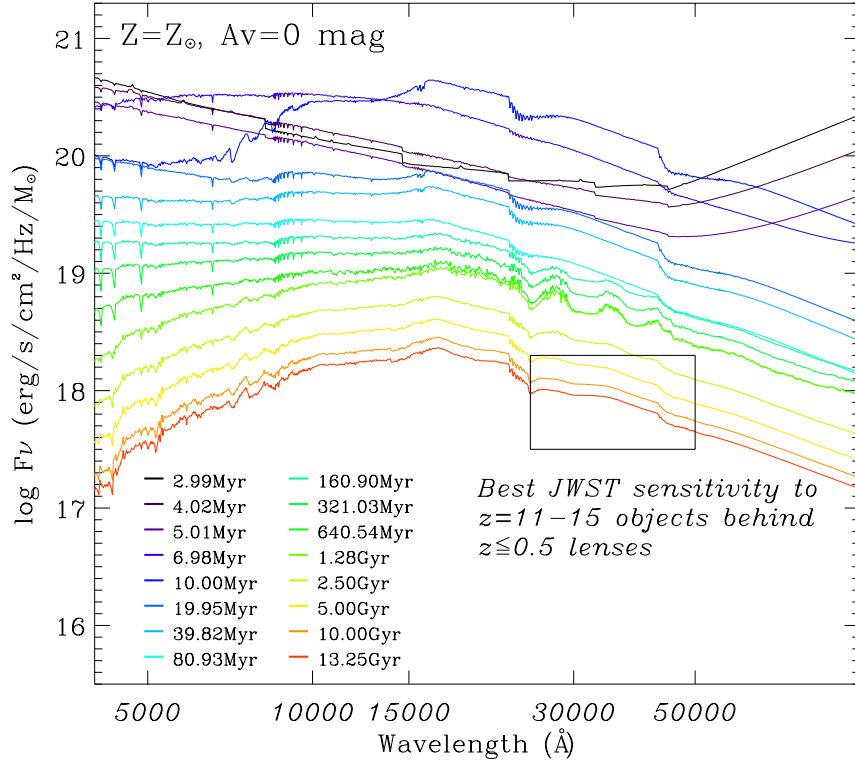
Figure 25. Examples from an array of combined Simple Stellar Population (SSP) Spectral Energy Distributions (SEDs) from [255] for sixteen different ages, fixed solar metallicity ($Z_\odot = 0.02$), and zero extinction. SED ages are indicated by the colored lines. Other examples of different metallicities and different extinction laws and AV-values are given by [255]. SPHEREx is ideal for measuring SEDs of foreground gravitational lenses ($z \lesssim 0.5$) that JWST will use to find First Light objects.

peak in the foreground lensing SEDs is still modest. The gain in foreground darkness of a $z \simeq 0.4$ cluster not being corrupted by the redshifted ICL beats the additional $(1 + z)^4$ dimming that one would get for a $z \simeq 1$ cluster. The latter generally also have by selection lower mass ($\sim 10^{14} \ M_\odot$), and are younger and dynamically less relaxed, making them less suited for optimal lensing of First Light ($z \gtrsim 10$–15) targets to be seen by JWST compared to more massive clusters at $z \simeq 0.4$. As discussed in Sec. 6.1.4 and 6.1.6, many of the best lensing clusters used by JWST will need an independent absolute measurement of the ICL, which may be complicated by rogue-path straylight seen by JWST, but can be provided by SPHEREx.

6.1.4 Absolute Flux Calibration: IntraGroup & IntraCluster Light Measurements

Our Galaxy is a bright IR source at $\lambda \simeq 1$–4 μm. Because of JWST's unavoidably open architecture, rogue-path straylight will hit the JWST secondary mirror from certain directions of the sky via its sunshield. We will not know precisely how large the amplitude of this straylight and its gradients are until JWST gets to its L2 orbit. Ray-tracing calculations suggest possible stray-light amplitudes of ~ 40–95% of Zodi with gradients of 2–5% (typical–worst case). Since this straylight doesn't go

through the optical path of JWST, it doesn't carry the PSF of the telescope, and so any JWST stray-light + gradients need to be disentangled from the astronomical targets: Galactic nebulae, stars, galaxies, galaxy groups, and galaxy clusters. If JWST rogue-path stray-light has a slight or complex gradient, it may be hard to separate these from the real IntraCluster Light (ICL) in gravitationally lensing clusters. As explained in Sec. 2.6, it will be critical for JWST to use the best gravitationally lensing clusters at z ≲ 0.5 to see First Light objects (z ≳ 10) in large numbers.

Since SPHEREx has a closed architecture [1, 248], it will suffer very little stray-light, and so SPHEREx will provide an absolute measurement of the IntraGroup Light (IGL) and the ICL for many tens of thousands of groups and clusters across the sky, as shown in Fig. 4. Galaxy groups contain most of the mass in the universe (rich, massive clusters are relatively rare), SPHEREx will be critical to measure the stellar masses of galaxy groups at z ≲ 0.5, including their diffuse baryonic IGL component. Similarly, since JWST will observe the best available gravitationally lensing clusters at z ≲ 0.5 (see Fig. 4) to detect the maximum number of First Light objects, and SPHEREx will be essential to measure the absolute value of the IGL at 0.75–5.0 μm, which provides a critical surface brightness-calibration for all JWST cluster work, including any diffuse mass component associated with their ICL.

As discussed above, stellar masses of galaxies, galaxy groups, and galaxy clusters will be directly estimated from JWST's 0.7–4.8 μm photometric measurements, but the absolute value of such estimates will be uncertain in groups and clusters if they indeed have a substantial amount of *diffuse* IGL and ICL, *i.e.*, the diffuse light from unresolved stars and perhaps unresolved globular clusters, which get dissociated from the individual galaxies in the group or cluster due to their substantial velocity dispersions. Indeed, ROSAT and Chandra X-ray observations have shown that both galaxy groups and galaxy clusters contain a substantial reservoir of hot X-ray gas [256, 257] that was torn from individual galaxies and escaped into the gravitational well of the group or the cluster, together with stars and globular clusters. It is known that this baryonic mass fraction of hot gas is substantial, but it is not known exactly how much mass is hidden in diffuse unresolved stars and globular clusters that are bound to the group or cluster as a whole, but *not bound to individual galaxies*. JWST will attempt to measure the IGL and ICL, but it is quite possible that this will require *accurate absolute* 0.7–4.8 μm flux measurements of the diffuse component in these groups and clusters. Spitzer will provide some anchor at 3.6 and 4.5 μm for the groups and clusters that it will have measured during its life-time, but SPHEREx will provide this anchor at 0.75-5.0 μm for *all* groups and clusters in the universe that have individual members visible to z ≲ 0.5 (see Fig. 4), thereby including *all* groups and clusters that JWST will observe during its lifetime.

To draw a comparison with radio astronomy: JWST will be the "high-resolution interferometer" at 0.7-4.8 μm that will map the First Galaxies in detail. SPHEREx will provide the absolutely critical "single-dish total-flux measurements" at 0.75–5.0 μm of *all* foreground objects to AB ≲ 19 mag and z ≲ 0.5, especially for low-SB structures such as IGL and ICL, for which JWST may not be able to accurately provide an absolute flux calibration.

6.1.5 Finding Dusty QSOs with SPHEREx' All-Sky Survey at z≃2–7

Fig. 26 left shows a Monte Carlo Markov-Chain model of the HST WFC3 PSF-star plus a host-galaxy Sersic light-profile for the first QSO host galaxy system detected at z≃6 [258, 259]. Careful contemporaneous orbital PSF-star subtraction removes most of the HST "OTA spacecraft breathing"
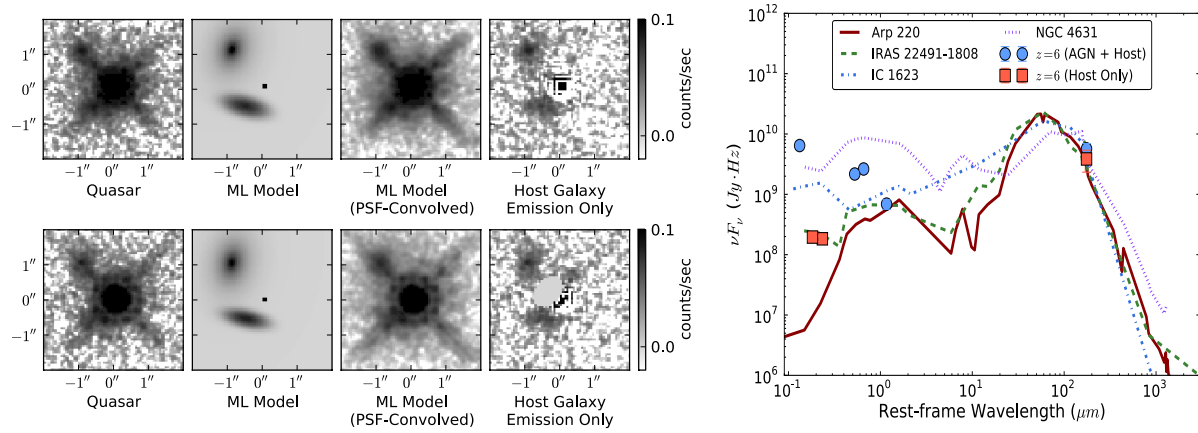
Figure 26. *Left:* HST WFC3 PSF+Sersic light-profile of the first QSO host galaxy system detected at z≃6 [258, 259]. The host has a giant merger morphology, plus very similar J (top) and H-band (bottom) structure. *Right:* Rest-frame far-UV—far-IR SED of its z≃5.85 QSO host system. Blue points show the total SED of the QSO+host galaxy. The red squares show the WFC3+submm SED of the z≃6 host galaxy only. The plotted range of local (U)LIRG SED models (Wang et al. 2011) show that the FIR/FUV flux ratio and UV-slope are consistent with local *dusty* starburst system with $A_{FUV}≃1$ mag and $M_{AB} ≲ -23.0$ mag, or ∼2 mag brighter than L^* at z≃6.

effects. For another QSO at z=6.42 with AB≃18.5 mag, *no* host galaxy was detected 100×fainter nearly to the noise limit, or at AB≳23.5 mag [258].

For the QSO at z≃5.85 in Fig. 26 left, however, a clear host system appears with a merger morphology, plus perhaps some tidal features, and a rather similar J- and H-band structure. Its UV-continuum slope is $\beta_\lambda≃-1.01$, which constrains its dust content. This rest-frame UV-color is significantly redder than LAEs and LBGs at z≃6, indicating significant internal reddening due to dust. Fig. 26 right shows the rest-frame far-UV—far-IR SED of this z≃6 QSO host system. Plotted are a range of fiducial local galaxy SEDs with starburst ages≲1 Gyr [260], normalized around ∼100 μm. The WFC3 data on the host galaxy rules out the unreddened spiral-like host galaxy SEDs (purple and blue curves), but allows starbursting (U)LIRGs & Arp 220-like SEDs [258, 259]. The FIR/FUV flux ratio and UV-slope are consistent with local *dusty* starburst systems with $A_{FUV}≃1$ mag and $M_{AB} ≲ -23.0$ mag, or ∼2 mag brighter than L^* at z≃6. Comparison to the surface density of bright LBGs at z≃6 then suggests that the duty cycle of this QSO may be ≲10^{-2} at z≃6 (*i.e.*, ≲10 Myrs), which would place it close to the Magorrian et al. relation [261].

Note how rapidly the z≃6 galaxy host SED gets brighter towards longer near-IR wavelengths. It is possible that close to half of the energy in the EBL comes from dust-obscured objects [45] and references therein), and that as a consequence, many QSOs will only show up in near–mid-IR selected surveys, which a combination of SPHEREx and WISE will provide at 0.7–24 μm for 1000's of QSO's at z≃2 to dozens of QSOs at z≃6–7. SPHEREx will thus provides all-sky samples of z≃2–7 QSOs for JWST, including these very dusty QSOs not selected in rest-frame UV–optical surveys. Careful JWST NIRCam+MIRI PSF-subtraction and/or Coronagraphy after 2018 will image the host galaxies of these z≃2–7 QSOs in the rest-frame optical–near-IR, constraining their stellar masses, and the M_{SMBH}–M_{bulge} relation of their host galaxies at the highest redshifts. SPHEREx is thus

the essential (dusty) object finder for JWST.

6.1.6 Galaxy Cluster Lensing with SPHEREx and JWST at $z \lesssim 0.5$

To see the largest number of First Light objects, JWST must cover the best lensing clusters. This is because the evolution of the Schechter UV luminosity Function (LF) is very rapid [262, 263]. While the faint-end LF-slope does not get much steeper than $\alpha \simeq -2$ for $z \gtrsim 6$ [264, 265], the characteristic density Φ^* and characteristic luminosity M^* potentially decline very rapidly with redshift. At $z \gtrsim 8$, we expect for JWST $\Phi^* \lesssim 10^{-3.5}$ (Mpc^{-3}) and that M^* may drop below –18 mag at $z \gtrsim 10$. If either one of these were not the case, then a much larger number of $z \simeq 9$–11 candidates would have been observed in the HUDF. This dramatic drop in Φ^* or M^* has significant consequences for the JWST survey strategy. Given the possible range in Schechter LF-parameter evolution with redshift for $z \gtrsim 8$–10, one can outline the optimal survey area and sensitivity covered per amount of JWST time to detect the maximum number of First Light ($z \gtrsim 10$–15) objects with JWST. These considerations imply that we will need to do a wedding-cake layered survey with JWST to see First Light, *e.g.*, $\gtrsim 10$ Webb Medium-Deep Fields to AB $\lesssim 29$ mag, several Webb Deep Fields to AB $\lesssim 31$ mag, and perhaps one Webb Ultra Deep Field to AB $\lesssim 32$ mag. In either case, the number of objects anticipated at $z \gtrsim 12$ will be very small, unless a significant number of Webb Deep Fields is pointed at the best gravitational lensing clusters.

For this reason, the community has started to gather a significant amount of data on the best lensing targets for JWST to detect $z \simeq 10$–15 objects. These clusters come from the ROSAT X-ray survey, the Planck and SPT SZ surveys, and various other cluster surveys such as CLASH, MaDCoWS, RedMapper and the Hubble Frontier Fields. As discussed in Sec. 6.1.4, the sweet spot for JWST lensing of First Light objects is for clusters at $0.3 \lesssim z \lesssim 0.5$ (see Fig. 25). To detect the largest number of lensed sources at $z \gtrsim 10$, these also need to have large masses of $10^{15-15.6}$ $M_\odot$, and high concentrations of $4.5 \lesssim C \lesssim 8.5$. The GAMA, SDSS, and WIGGLEz samples (see Fig. 4) are an excellent database to define such samples. The many available spectroscopic redshifts provide accurate dynamical masses [43, 44], and help remove chance projections. As discussed in Sec. 6.1.4, SPHEREx is needed to characterize the total stellar light for these best lensing $z \lesssim 0.5$ clusters that will be observed with JWST. This includes a careful absolute measurement of the diffuse light (ICL) in these clusters that JWST may not be able to disentangle from its anticipated rogue-path stray-light.

6.2 WFIRST and Euclid

NASA's Wide Field Infrared Survey Telescope (WFIRST; [266]) was the top ranked large space mission recommendation in the 2010 Decadal Survey. One of WFIRST's primary science goals is to determine the nature of the dark energy that is driving the current accelerated expansion of the Universe. WFIRST entered into Phase A in February 2016 in preparation for launch in ~ 2024. An existing 2.4 meter telescope will provide Hubble Space Telescope quality imaging, but over a field of view that is ~ 100 times that of Hubble. WFIRST will have a 6 year primary mission at L2, but there are no consumables that preclude a mission of 10 or more years. The Wide Field Instrument (WFI) on WFIRST will consist of 18 4k by 4k H4RG Near infrared detectors that will provide grism spectroscopy (1.35-1.89μm; R=461) and imaging (0.76-2μm) over 0.28 square degrees at a pixel scale of 0.11 arcsec. An Integral Field Unit spectroscopic channel designed for supernova follow up will

have a single 2k by 2k detector and provide spectroscopy at R=80 to 120 at 0.6-2 μm. WFIRST will perform a $\simeq$ 2300 square degree High Latitude Survey (HLS) in order to obtain weak lensing and galaxy clustering (BAO and RSD) measurements. A deeper survey of tens of square degrees will be used to find and follow up $\simeq$ 2700 supernovae. Thus, WFIRST measure both the expansion history of the Universe and the growth of structure using multiple techniques with a survey designed for very tight systematics control.

The European Space Agency (ESA) Euclid mission [267] will launch in 2020 for a 6 year mission at L2 to study dark energy using weak lensing and galaxy clustering. Euclid will have a 1.2 m primary mirror and two instruments. The visible instrument (VIS) will have 36 CCDs (4k by 4k) that will perform photometry for galaxy shape measurements using a single wide (Riz) filter. The Near Infrared Spectrometer and Photometer (NISP) instrument will use 16 2k by 2k near infrared (NIR) detectors (provided by NASA) to perform imaging and grism spectroscopy in the 1-2 μm range. Both instruments will survey the same 0.5 square degree piece of the sky simultaneously via a dichroic. Euclid will cover the lowest sky background 15,000 square degrees in Riz (single wide filer), Y, J and H filters and employ a simple grism spectrometer to perform a survey with an unprecedented combination of area and resolution.

Both WFIRST and Euclid are designed to do those portions of the dark energy experiment that can be done only from space. There are three such measurements:

1. Very accurate galaxy shape measurements for weak gravitational lensing enabled by the small, stable PSF of a space-based telescope.

2. Near infrared photometry for accurate photometric redshifts when combined with ground-based optical photometry.

3. Near infrared spectroscopy for accurate galaxy clustering measurements at redshifts $z > 1$.

There are a number of ways that the SPHEREx all sky infrared measurements will be synergistic with Euclid and WFIRST:

1. Filling in the low redshift (z<1) galaxy clustering field for baryon acoustic oscillations (BAO) and redshift-space distortions (RSD). Since both WFIRST and Euclid concentrate on z>1 for this cosmological probe, the combination with SPHEREx will allow for a full measurement of galaxy clustering over the full range at which the effects of dark energy are expected to begin to dominate the expansion history of the Universe.

2. SPHEREx will acquire a huge number of low redshift spectra to calibrate photometric redshifts. Every galaxy in the WFIRST and Euclid weak lensing surveys will require a distance measure and the vast majority of these will be calculated via photometric redshifts. Recent work has shown that up to 10^5 spectra may be needed to calibrate these photometric redshifts, and these spectra need to be a complete sample down to the magnitude used for weak lensing, 24.5 for Euclid and $\simeq$ 27 for WFIRST and LSST (see, e.g. [268]). While many of these spectra will need to be acquired with ten and thirty meter class telescopes, a great number of them will be readily available from SPHEREx, especially at z<1. Thus, SPHEREx will be a powerful resource in the required calibration of the photometric redshifts for WFIRST and Euclid.

3. Intrinsic galaxy alignments (see [269–271] for recent reviews) represent the largest astrophysical systematic for weak lensing measurements. Unmitigated, these intrinsic alignments can seriously bias cosmological inferences. However, Krause et al (2016) [272], have shown that if intrinsic alignments are controlled at $z < 1$, then the cosmological results for an LSST-like or Euclid-like survey will be virtually unbiased. Intrinsic alignment mitigation is best achieved via very accurate redshifts for the foreground galaxies; thus, the immense z<1 SPHEREx spectroscopic redshift sample will prove to be a boon for intrinsic alignment mitigation for future lensing experiments.

4. The same SPHEREx $z < 1$ spectroscopic redshift sample that will provide intrinsic alignment mitigation will provide very accurate distance measures for foreground galaxies used for galaxy-galaxy lensing measurements. Combining this with precision shape measurements of background galaxies via WFIRST and Euclid will allow for unprecedented galaxy-galaxy lensing measurements that will enable the study of the galaxy-halo connection as a function of luminosity, type and environment. This will also allow the study of baryonic feedback processes as a function of the above variables and enables higher order statistics such as galaxy-galaxy-galaxy lensing. This is detailed further below in Sec. 6.2.1

5. Both Euclid and WFIRST will have deep fields over several tens of square degrees that reach two or more magnitudes deeper than the wide cosmology surveys described above. Those fields will produce additional cosmology (for instance the SN survey for WFIRST), a huge amount of ancillary science, especially in galaxy evolution, and calibration. Subject to only the orbital constraints of WFIRST and Euclid at L2, these deep fields can be coordinated with the deepest areas of the SPHEREx survey, creating a lasting legacy data that will be exploited for multiple science goals for years to come. In fact the SPHEREx deep survey field at the SEP coincides with one of Euclid's deep fields.

6.2.1 Euclid and WFIRST Synergies with SPHEREx Example: Halo Masses for SPHEREx-selected galaxy populations

As an example of the powerful synergies between SPHEREx and other surveys such as Euclid and WFIRST, we detail below how we could measure better halo-masses using galaxy-galaxy lensing.

Motivation. SPHEREx will discover interesting galaxy populations as described in Sec. 2.2 and Sec. 2.3. Measuring the host halo mass scale for SPHEREx selected galaxy populations will facilitate the connection with broader galaxy evolution models, and will constrain galaxy evolution as a function of environment. Here we forecast the accuracy with which halo masses can be inferred via stacked galaxy-galaxy lensing, using the SPHEREx selected galaxies as the lens sample, and Euclid weak lensing source galaxies as the background sample.

Forecast Details. We consider a SPHEREx selected galaxy population with comoving density $n_{\rm g} = 10^{-5}(h/{\rm Mpc})^3$, i.e., a rather rare population, and assume a halo-mass – observable relation with characteristic mass scale M_0 and log-normal scatter $\sigma_{M|{\rm obs}} = 0.75$. The accuracy of the halo mass measurement also depends on the redshift of the SPHEREx selected galaxies, the redshift distribution of background galaxies, and the survey area for which imaging and galaxy shape measurements are available; we assume a Euclid-like survey for the source galaxy population.

Fig. 27 shows the uncertainty in the halo mass determination as a function of host halo mass (x axis; stronger lensing signal from more massive halos), and the lens redshift bin. At fixed comoving density, the signal-to-noise ratio of galaxy-galaxy lensing increases with halo mass, and the halo mass measurement uncertainty decreases with increasing halo mass. The dependence of mass uncertainty on lens redshift in this plot is a competition of two effects: for the choice of redshift bins in this plot, the volume per redshift bin (and hence the number of lens galaxies) increases with redshift, while the number of background galaxies decreases. These uncertainties are marginalized over cosmology, source redshift uncertainties, shear calibration and scatter of the mass–observable relation. For rare galaxy populations (i.e., in the shot-noise dominated regime), the mass uncertainty scales approximately as

$$\sigma\left(\lg(M)\right) \propto \sqrt{\frac{(10^{-5}(h/\mathrm{Mpc})^3)}{n_\mathrm{g}}}. \tag{6.1}$$

Stacked weak lensing using SPHEREx selected lensing galaxies and shapes of background galaxies from Euclid or WFIRST imaging will enable interesting constraints on host halo masses for a range of halo masses and lens redshifts. These halo mass measurements are complementary to halo masses inferred from galaxy clustering, and with the assumption of a halo mass – bias relation can be used to validate galaxy bias measurements. Note that this technique can be extended to higher lens redshift using deeper imaging surveys, such as LSST (see Sec. 6.3 below).
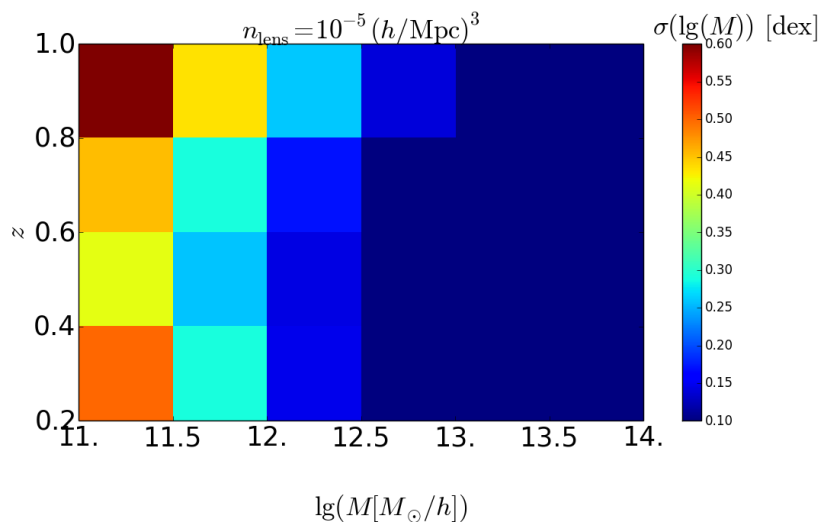
Figure 27. Statistical uncertainty of weak-lensing based halo mass estimates for a rare, SPHEREx-selected galaxy population as a function of halo mass and redshift. The color bar is capped at $\sigma(lg(M)) = 0.1$.

6.3 SPHEREx and the Large Synoptic Survey Telescope

As described earlier in Sec. 1, many of the major new astronomical facilities and capabilities that will come on-line in the 2020's will be dedicated to wide-field surveys of the sky. This is very much reflected in the priorities of the 2010 Decadal Survey: the highest-ranked space-based mission is the Wide-Field Infrared Survey Telescope (WFIRST), and the highest-ranked large ground-based

telescope is the Large Synoptic Survey Telescope (LSST). Much of the interest and excitement about such surveys is the tremendous breadth of the science they can carry out. This has been the lesson of the Sloan Digital Sky Survey (SDSS), which uses a modest 2.5m telescope with a large field of view to image and do follow-up spectroscopy of 1/4–1/3 of the celestial sphere. It was originally designed to make a three-dimensional map of the distribution of galaxies, but the data required to make that happen has led to breakthroughs in gravitational lensing, the structure of the Milky Way, the evolution of quasars, the nature of brown dwarfs, and many other fields unanticipated at the time the SDSS was designed. The success of the initial SDSS, and its utility to the community as a whole (at this writing, it has resulted in more than 7000 refereed papers, the vast majority written with publicly distributed data) has resulted in its operation being extended multiple times, with continually evolving scientific goals.

The LSST was in many ways inspired by the SDSS model: by gathering data designed for specific scientific goals, and analyzing those data as well as the laws of physics and statistics allow, one enables a broad (and to some extent, unanticipated) set of science outcomes. The LSST consists of a wide-field optical telescope with an effective diameter of 6.7 meters, and a 3.5 Gigapixel imaging camera with a field of view of 9.6 deg^2. The combination of the large telescope aperture and the enormous field of view means that the LSST is able to simultaneously survey the sky "Wide, Deep and Fast", i.e., to cover a large solid angle to faint magnitudes, and do so repeatedly over its 10-year lifetime, to study variable and transient phenomena of all sorts. The detailed characteristics of the survey may be found in the overview paper of [273], the LSST Science Book [54], and the LSST website, http://www.lsst.org.

The LSST main survey footprint will cover 18,000 deg^2 of high-latitude sky in the Southern hemisphere, in the declination range $-65° < \delta < +2°$. Ancillary programs will push further North and South, and to lower Galactic latitudes. Imaging will be done in six broad bands, $ugrizy$, carried out in 30-second "visits" (probably divided into two 15-second exposures). The 5-σ point-source depth in a single visit will be $r \sim 24.7$ in typical seeing (median 0.67"). Each field will be visited over 800 times (summed over the six filters) over the 10-year survey period, yielding a full-survey depth of $r = 27.5$ (and similarly in the other bands). The key science goals include the study of dark matter and dark energy via gravitational lensing, supernovae, and large-scale structure; the mapping of the halo of the Milky Way; the characterization of the variable and transient sky; and the distribution of asteroids in the Solar System, from those which come close to Earth to the outer reaches of the Kuiper Belt. However, as we stressed above, the LSST science impact will be much broader than that, and promises to influence essentially every area of observational astronomy.

Analyzing the resulting tens of petabytes of data is a major component of the LSST project [274]. The fully reduced and calibrated object catalogs will be made available using a sophisticated user interface. The data will have no proprietary period, but will be made public both on short timescales (all variable objects will be released worldwide as they are recognized by specialized software, following each exposure) and on long ones (yearly data releases of the data will be distributed to the US and Chilean communities).

The construction of the LSST system is supported by the US National Science Foundation and Department of Energy, as well as generous contributions from private donations. The telescope is currently under construction, and will see first engineering light in late 2019. After an extensive commissioning period, it will begin its 10-year survey in 2022.

At first glance, the synergy between SPHEREx and LSST is not obvious, as LSST is focused on the faint universe, pushing to 27.5, while SPHEREx reaches its 5-sigma limit at an AB magnitude of 18.5 for each 96 frequency elements. (The saturation limit of LSST will depend on the detailed properties of the sensors, but will probably be between 16 and 17 in the r band, bright enough for easy detection by SPHEREx). However, LSST is a purely imaging survey, and the spectroscopic capabilities of SPHEREx and the extension to the IR will be tremendously useful for characterizing the properties of the galaxies and stars it finds. LSST plans to use photometric redshifts to determine the distances of its galaxies. The combination of LSST and SPHEREx will give continuous wavelength coverage from the atmospheric cutoff at ~ 3200Å to 5 μm, allowing far more than redshifts to be determined; with such detailed spectral energy density distribution information, one can also determine stellar masses, star formation rates, dust extinction, the presence of an AGN, and perhaps metallicities as well. There is work ahead to determine specifically the impacts of the addition of LSST photometry to the SPHEREx spectroscopy will be, as a function of magnitude. This can be carried out for every galaxy above the SPHEREx 5-sigma limit, and can be done to much fainter magnitudes in the SPHEREx deep field at the South Ecliptic Pole. It will also be tremendously valuable to stack SPHEREx data at the positions of LSST-defined samples, to characterize their properties (see Padmanabhan et al. 2016, in preparation).

The three-dimensional map of the galaxy distribution that SPHEREx will produce can be used to measure *clustering redshifts*, following the techniques of [275] and [276]. This will allow exquisite calibration of the redshift distribution of any subsample of galaxies in the LSST sample, at least over the redshift range that SPHEREx will probe.

Another great synergy between SPHEREx and LSST will be in the search for and study of extremely red objects. Such red objects fall into several categories:

- Objects at extremely high redshift ($z > 6$), whose optical light is absorbed by neutral hydrogen in the intergalactic medium (the Gunn-Peterson trough). The most luminous quasars at these redshifts are brighter than the $5\,\sigma$ limit of SPHEREx, and binning further in wavelength will allow identification of candidates much fainter than this.

- Brown dwarfs, whose surface temperatures will be determined to high accuracy with SPHEREx spectral coverage (see Sec. 4.3).

- Highly reddened objects, whose spectra may show strong emission lines in the SPHEREx wavelength coverage.

Real work is needed in each of these cases to quantify what can be learned from the combination of LSST and SPHEREx data. Some particularly interesting objects identified this way will require detailed follow-up, e.g., with the James Webb Space Telescope as outlined above (Sec. 6.1), which wil be a powerful tool for characterizing unusual populations revealed from the LSST-SPHEREx synergy.

The fact that SPHEREx will survey the entire $4\,\pi$ steradians of the sky means that overlaps will occur with *all* the wide-field surveys of the 2020's. This means that much of SPHEREx science will depend on the mutual comparison of different datasets, and building the data structures to allow these comparisons to be carried out efficiently and consistently will be key to ensuring the SPHEREx scientific legacy.

6.4   SPHEREx and TESS

Direct and precise stellar masses and radii are essential for stellar astrophysics, as they enable the calibration of correlations between fundamental stellar properties, and tests of stellar evolutionary models. Additionally, the masses and radii of exoplanets discovered via the transit and radial velocity methods depend on the masses and radii of the host stars. The best sample to date – that of Torres [277] – has 94 double-lined eclipsing binaries (and αCen) with precise ($\leq 3\%$ fractional uncertainty), model-independent masses and radii. However, this sample contains only four stars with masses below half that of the Sun – a region in which measured radii differ significantly from radii predicted by models (typically a 10% discrepancy). Single M dwarfs also exhibit radius inflation, but the masses of these stars cannot be measured directly and are typically inferred from a mass-luminosity relation (cf. [278]). Furthermore, very few of the Torres systems have abundance measurements.

A much larger sample of single-lined eclipsing systems discovered by exoplanet transit surveys can – with radial velocity follow-up, well-constrained SEDs, and *Gaia* parallaxes – also yield model-independent masses and radii of both the primary and secondary stars. Many of these systems will have low-mass stellar secondaries, thereby filling in a relatively poorly populated region of parameter space of stars with directly measured parameters, given precise follow-up eclipse photometry and high-resolution radial velocity measurements.

The all-sky Transiting Exoplanet Survey Satellite (TESS) will target 200,000 bright ($I_C \leq 13$) stars with spectral types ranging from early F to late M for transiting exoplanets, with expected yields of 1,700 planetary systems and 1,150 eclipsing binaries [279]. Thus, TESS will observe many single-lined eclipsing binaries (including transiting exoplanets) which will have SPHEREx spectrophotometry as well as *Gaia* parallaxes and spectrophotometry and literature broad-band UV-NIR fluxes; high-resolution RV and precise follow-up photometry will also be possible. Fig. 28 illustrates the anticipated power of spectrophotometric information in constraining the radius of a typical TESS target. Reducing the uncertainty in the stars radius from $\sim 5\%$ [177] to $\sim 1\%$, as shown in Fig. 28 for KELT-3, will reduce the uncertainty in the radius of the exoplanet to $\sim 1\%$ as well. Applied to many systems, this precision will greatly increase our knowledge of exoplanet properties.

In particular, a large number of low-mass stars will have precisely determined masses and radii this way, both as eclipsing companions to more massive stars and as transiting exoplanet hosts, so the low-mass end of the mass-radius relation can be much more strongly anchored with the inclusion of these systems. Specifically, due to SPHEREx coverage of the SED peak for cooler stars, the radii (and thus masses) of M dwarf planet hosts *and* the planets around them will be known extremely well. Additionally, TESS is sensitive enough to detect $p-$mode oscillations for around 2,000 main-sequence and sub-giant stars with $V \leq 7.5$. For the subset of eclipsing systems for which TESS will obtain asteroseismic measurements of the primary star, the asteroseismic density places an additional constraint (albeit not an orthogonal one) on the primary's stellar parameters and tightens the uncertainties on the host star's mass and radius and, therefore, on the companion's mass and radius.

In addition, measuring spectroscopic parameters for stars in double-lined eclipsing systems requires accurate disentanglement of each star's spectral features from the composite spectra. TESS, however, can provide effective temperatures of the secondary directly from the secondary eclipse depths, given the primary's effective temperature as determined from spectrophotometric interferometry.
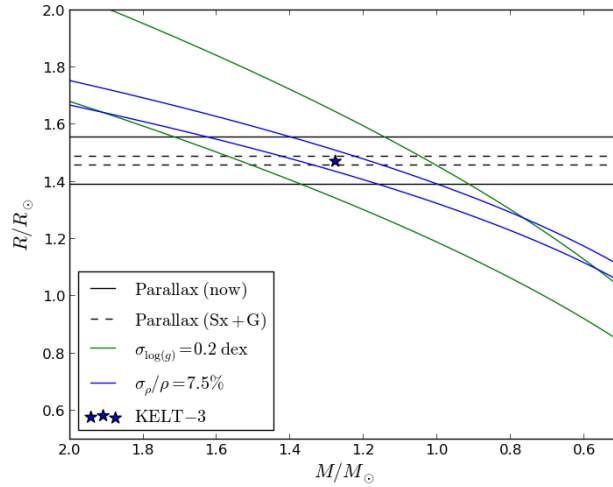
Figure 28. Constraints on the mass and radius of KELT-3 (star) from the transit density (blue), spectroscopic surface gravity (green), parallax with only broad-band flux measurements (black solid), and parallax with broad-band fluxes as well as estimated SPHEREx and *Gaia* spectrophotometry assuming Poisson-noise dominated errors (black dashed). Uncertainties are assumed typical values, and the KELT-3 parameters and broad-band flux measurements can be found in [177].

7 Conclusion

The SPHEREx Community Workshop identified and discussed many scientific investigations enabled by the unique 0.75-to-5 μm all sky spectral database which will be the legacy of SPHEREx. This scientific return from this legacy would make SPHEREx a worthy participant in the Decade of the Surveys, as the 2020s have been called. The Workshop also showed that SPHEREx is synergistic with numerous other major astronomical facilities - space and ground including GAIA, JWST, LSST, Kepler, eROSITA, TESS, Euclid and WFIRST. JWST and WFIRST users in particular could mine the SPHEREx data bases to select optimum targets for a range of General Observer investigations. For the case of JWST, this synergy relies on the temporal overlap of the two missions. Selection of SPHEREx for flight on the current schedule would lead to initial releases of SPHEREx data and catalogs in 2021-to-2022. This is well synchronized with JWST, which is planned to operate at least through 2024. While JWST is expected to operate well beyond 2024, delaying the selection of SPHEREx to a subsequent opportunity two or three years hence would undermine this valuable synergy. The scientific examples discussed above illuminate the power of an all-sky spectral survey, which would be a new scientific tool for astronomers. On the one hand, it would permit comprehensive studies of known classes of objects, providing spectra for thousands of brown dwarfs or hundreds of millions of galaxies, as an example. It would also identify and highlight for further study objects such as low metallicity stars or high redshift QSOs, known to exist but frequently difficult to identify on the basis of photometric surveys alone. Finally, of course, like other all sky surveys which open new parameter space, SPHEREx has the potential to yield new discoveries which change our view of the astronomical Universe.

Acknowledgments

References

[1] O. Dor et al., *Cosmology with the SPHEREX All-Sky Spectral Survey*, 1412.4872.

[2] N. P. Ross, A. D. Myers, E. S. Sheldon, C. Yèche, M. A. Strauss, J. Bovy et al., *The SDSS-III Baryon Oscillation Spectroscopic Survey: Quasar Target Selection for Data Release Nine*, *ApJS* **199** (Mar., 2012) 3, [1105.0606].

[3] J. E. Geach, D. N. A. Murphy and R. G. Bower, *4098 galaxy clusters to z=0.6 in the Sloan Digital Sky Survey equatorial Stripe 82*, *MNRAS* **413** (June, 2011) 3059–3067, [1101.4585].

[4] D. Calzetti, R. C. Kennicutt, C. W. Engelbracht, C. Leitherer, B. T. Draine, L. Kewley et al., *The Calibration of Mid-Infrared Star Formation Rate Indicators*, *ApJ* **666** (Sept., 2007) 870–895, [0705.3377].

[5] R. C. Kennicutt, Jr., C.-N. Hao, D. Calzetti, J. Moustakas, D. A. Dale, G. Bendo et al., *Dust-corrected Star Formation Rates of Galaxies. I. Combinations of Hα and Infrared Tracers*, *ApJ* **703** (Oct., 2009) 1672–1695, [0908.0203].

[6] N. Rahman, A. D. Bolatto, T. Wong, A. K. Leroy, F. Walter, E. Rosolowsky et al., *CARMA Survey Toward Infrared-bright Nearby Galaxies (STING): Molecular Gas Star Formation Law in NGC 4254*, *ApJ* **730** (Apr., 2011) 72, [1009.3272].

[7] G. Liu, J. Koda, D. Calzetti, M. Fukuhara and R. Momose, *The Super-linear Slope of the Spatially Resolved Star Formation Law in NGC 3521 and NGC 5194 (M51a)*, *ApJ* **735** (July, 2011) 63, [1104.4122].

[8] D. Calzetti, *Star Formation Rate Indicators*, 1208.2997.

[9] A. K. Leroy, F. Bigiel, W. J. G. de Blok, S. Boissier, A. Bolatto, E. Brinks et al., *Estimating the Star Formation Rate at 1 kpc Scales in nearby Galaxies*, *AJ* **144** (July, 2012) 3, [1202.2873].

[10] S. E. Meidt, E. Schinnerer, J. H. Knapen, A. Bosma, E. Athanassoula, K. Sheth et al., *Reconstructing the Stellar Mass Distributions of Galaxies Using S^4G IRAC 3.6 and 4.5 µm Images. I. Correcting for Contamination by Polycyclic Aromatic Hydrocarbons, Hot Dust, and Intermediate-age Stars*, *ApJ* **744** (Jan., 2012) 17, [1110.2683].

[11] M. Querejeta, S. E. Meidt, E. Schinnerer, M. Cisternas, J. C. Muñoz-Mateos, K. Sheth et al., *The Spitzer Survey of Stellar Structure in Galaxies (S^4G): Precise Stellar Mass Distributions from Automated Dust Correction at 3.6 µm*, *ApJS* **219** (July, 2015) 5, [1410.0009].

[12] S. Malhotra and J. E. Rhoads, *The volume fraction of ionized intergalactic gas at redshift z=6.5*, *Astrophys. J.* **647** (2006) L95–L98, [astro-ph/0511196].

[13] R. E. Skelton et al., *3D-HST WFC3-selected Photometric Catalogs in the Five CANDELS/3D-HST Fields: Photometry, Photometric Redshifts and Stellar Masses*, *Astrophys. J. Suppl.* **214** (2014) 24, [1403.3689].

[14] R. A. Windhorst, S. H. Cohen, N. P. Hathi, P. J. McCarthy, R. E. Ryan, Jr., H. Yan et al., *The Hubble Space Telescope Wide Field Camera 3 Early Release Science Data: Panchromatic Faint Object Counts for 0.2-2 µm Wavelength*, *ApJS* **193** (Apr., 2011) 27, [1005.2776].

[15] G. Bruzual and S. Charlot, *Stellar population synthesis at the resolution of 2003*, *Mon. Not. Roy. Astron. Soc.* **344** (2003) 1000, [astro-ph/0309134].

[16] R. J. Cool, J. Moustakas, M. R. Blanton, S. M. Burles, A. L. Coil, D. J. Eisenstein et al., *The PRIsm MUlti-object Survey (PRIMUS). II. Data Reduction and Redshift Fitting*, *ApJ* **767** (Apr., 2013) 118, [1303.2672].

[17] O. Ilbert, P. Capak, M. Salvato, H. Aussel, H. J. McCracken, D. B. Sanders et al., *Cosmos Photometric Redshifts with 30-Bands for 2-deg^2*, *ApJ* **690** (Jan., 2009) 1236–1249, [0809.2101].

[18] P. G. van Dokkum, I. Labbé, D. Marchesini, R. Quadri, G. Brammer, K. E. Whitaker et al., *The NEWFIRM Medium-Band Survey: Filter Definitions and First Results*, *PASP* **121** (Jan., 2009) 2–8, [0901.0551].

[19] A. Cava, P. G. Pérez-González, M. C. Eliche-Moral, E. Ricciardelli, A. Vidal-García, B. Alcalde Pampliega et al., *SHARDS: A Global View of the Star Formation Activity at z ˜ 0.84 and z ˜ 1.23*, *ApJ* **812** (Oct., 2015) 155, [1507.07939].

[20] M. Kriek, P. G. van Dokkum, K. E. Whitaker, I. Labbé, M. Franx and G. B. Brammer, *Hα and 4000 Å Break Measurements for ˜3500 K-selected Galaxies at 0.5 < z < 2.0*, *ApJ* **743** (Dec., 2011) 168, [1103.0279].

[21] M. C. Cooper, J. A. Newman, D. S. Madgwick, B. F. Gerke, R. Yan and M. Davis, *Measuring Galaxy Environments with Deep Redshift Surveys*, *ApJ* **634** (Dec., 2005) 833–848, [astro-ph/0506518].

[22] K. Kovač, S. J. Lilly, O. Cucciati, C. Porciani, A. Iovino, G. Zamorani et al., *The Density Field of the 10k zCOSMOS Galaxies*, *ApJ* **708** (Jan., 2010) 505–533, [0903.3409].

[23] P. Erwin, L. Gutiérrez and J. E. Beckman, *A Strong Dichotomy in S0 Disk Profiles between the Virgo Cluster and the Field*, *ApJ* **744** (Jan., 2012) L11, [1111.5027].

[24] Y.-C. Chen, S. Ho, P. E. Freeman, C. R. Genovese and L. Wasserman, *Cosmic web reconstruction through density ridges: method and algorithm*, *MNRAS* **454** (Nov., 2015) 1140–1156, [1501.05303].

[25] G. Kauffmann, C. Li, W. Zhang and S. Weinmann, *A re-examination of galactic conformity and a comparison with semi-analytic models of galaxy formation*, *MNRAS* **430** (Apr., 2013) 1447–1456, [1209.3306].

[26] J. Kormendy and L. C. Ho, *Coevolution (Or Not) of Supermassive Black Holes and Host Galaxies*, *ARA&A* **51** (Aug., 2013) 511–653, [1304.7762].

[27] W. Voges, B. Aschenbach, T. Boller, H. Bräuninger, U. Briel, W. Burkert et al., *The ROSAT all-sky survey bright source catalogue*, *A&A* **349** (Sept., 1999) 389–405, [astro-ph/9909315].

[28] T. Boller, M. J. Freyberg, J. Trümper, F. Haberl, W. Voges and K. Nandra, *Second ROSAT all-sky survey (2RXS) source catalogue*, *A&A* **588** (Apr., 2016) A103.

[29] M. Brusa, G. Zamorani, A. Comastri, G. Hasinger, N. Cappelluti, F. Civano et al., *The XMM-Newton Wide-Field Survey in the COSMOS Field. III. Optical Identification and Multiwavelength Properties*

of a Large Sample of X-Ray-Selected Sources, *ApJS* **172** (Sept., 2007) 353–367, [`astro-ph/0612358`].

[30] T. Budavári and A. S. Szalay, *Probabilistic Cross-Identification of Astronomical Sources*, *ApJ* **679** (May, 2008) 301–309, [`0707.1611`].

[31] D. Stern, R. J. Assef, D. J. Benford, A. Blain, R. Cutri, A. Dey et al., *Mid-infrared Selection of Active Galactic Nuclei with the Wide-Field Infrared Survey Explorer. I. Characterizing WISE-selected Active Galactic Nuclei in COSMOS*, *ApJ* **753** (July, 2012) 30, [`1205.0811`].

[32] N. Benítez, M. Moles, J. A. L. Aguerri, E. Alfaro, T. Broadhurst, J. Cabrera-Caño et al., *Optimal Filter Systems for Photometric Redshift Estimation*, *ApJ* **692** (Feb., 2009) L5–L8, [`0812.3568`].

[33] C. Wolf, K. Meisenheimer, M. Kleinheinrich, A. Borch, S. Dye, M. Gray et al., *A catalogue of the Chandra Deep Field South with multi-colour classification and photometric redshifts from COMBO-17*, *A&A* **421** (July, 2004) 913–936, [`astro-ph/0403666`].

[34] Y. Taniguchi, N. Z. Scoville, D. B. Sanders, B. Mobasher, H. Aussel, P. Capak et al., *The HST Cosmos Project: Contribution from the Subaru Telescope*, *Journal of Korean Astronomical Society* **38** (June, 2005) 187–190, [`astro-ph/0503645`].

[35] M. Salvato, G. Hasinger, O. Ilbert, G. Zamorani, M. Brusa, N. Z. Scoville et al., *Photometric Redshift and Classification for the XMM-COSMOS Sources*, *ApJ* **690** (Jan., 2009) 1250–1263, [`0809.2098`].

[36] C. N. Cardamone, P. G. van Dokkum, C. M. Urry, Y. Taniguchi, E. Gawiser, G. Brammer et al., *The Multiwavelength Survey by Yale-Chile (MUSYC): Deep Medium-band Optical Imaging and High-quality 32-band Photometric Redshifts in the ECDF-S*, *ApJS* **189** (Aug., 2010) 270–285, [`1008.2974`].

[37] M. Salvato, O. Ilbert, G. Hasinger, A. Rau, F. Civano, G. Zamorani et al., *Dissecting Photometric Redshift for Active Galactic Nucleus Using XMM- and Chandra-COSMOS Samples*, *ApJ* **742** (Dec., 2011) 61, [`1108.6061`].

[38] S. Fotopoulou, M. Salvato, G. Hasinger, E. Rovilos, M. Brusa, E. Egami et al., *Photometry and Photometric Redshift Catalogs for the Lockman Hole Deep Field*, *ApJS* **198** (Jan., 2012) 1, [`1110.0960`].

[39] L.-T. Hsu, M. Salvato, K. Nandra, M. Brusa, R. Bender, J. Buchner et al., *CANDELS/GOODS-S, CDFS, and ECDFS: Photometric Redshifts for Normal and X-Ray-Detected Galaxies*, *ApJ* **796** (Nov., 2014) 60, [`1409.7119`].

[40] S. Marchesi, F. Civano, M. Elvis, M. Salvato, M. Brusa, A. Comastri et al., *The Chandra COSMOS Legacy survey: optical/IR identifications*, *ApJ* **817** (Jan., 2016) 34, [`1512.01105`].

[41] F. Civano, M. Brusa, A. Comastri, M. Elvis, M. Salvato, G. Zamorani et al., *The Population of High-redshift Active Galactic Nuclei in the Chandra-COSMOS Survey*, *ApJ* **741** (Nov., 2011) 91, [`1103.2570`].

[42] A. Georgakakis, J. Aird, J. Buchner, M. Salvato, M.-L. Menzel, W. N. Brandt et al., *The X-ray luminosity function of active galactic nuclei in the redshift interval z=3-5*, *MNRAS* **453** (Oct., 2015) 1946–1964, [`1507.07558`].

[43] X. Yang, H. J. Mo, F. C. van den Bosch, A. Pasquali, C. Li and M. Barden, *Galaxy Groups in the SDSS DR4. I. The Catalog and Basic Properties*, *ApJ* **671** (Dec., 2007) 153–170, [`0707.4640`].

[44] A. S. G. Robotham, P. Norberg, S. P. Driver, I. K. Baldry, S. P. Bamford, A. M. Hopkins et al., *Galaxy and Mass Assembly (GAMA): the GAMA galaxy group catalogue (G³Cv1)*, *MNRAS* **416**

(Oct., 2011) 2640–2668, [1106.1994].

[45] S. P. Driver, A. H. Wright, S. K. Andrews, L. J. Davies, P. R. Kafle, R. Lange et al., *Galaxy And Mass Assembly (GAMA): Panchromatic Data Release (far-UV-far-IR) and the low-z energy budget*, *MNRAS* **455** (Feb., 2016) 3911–3942, [1508.02076].

[46] M. J. Drinkwater, R. J. Jurek, C. Blake, D. Woods, K. A. Pimbblet, K. Glazebrook et al., *The WiggleZ Dark Energy Survey: survey design and first data release*, *MNRAS* **401** (Jan., 2010) 1429–1452, [0911.4246].

[47] E. S. Rykoff, E. Rozo, M. T. Busha, C. E. Cunha, A. Finoguenov, A. Evrard et al., *redMaPPer. I. Algorithm and SDSS DR8 Catalog*, *ApJ* **785** (Apr., 2014) 104, [1303.3562].

[48] Z. L. Wen, J. L. Han and F. S. Liu, *A Catalog of 132,684 Clusters of Galaxies Identified from Sloan Digital Sky Survey III*, *ApJS* **199** (Apr., 2012) 34, [1202.6424].

[49] B. A. Benson, P. A. R. Ade, Z. Ahmed, S. W. Allen, K. Arnold, J. E. Austermann et al., *SPT-3G: a next-generation cosmic microwave background polarization experiment on the South Pole telescope*, in *Millimeter, Submillimeter, and Far-Infrared Detectors and Instrumentation for Astronomy VII*, vol. 9153 of *Proc. SPIE*, p. 91531P, July, 2014. 1407.2973. DOI.

[50] S. W. Henderson, R. Allison, J. Austermann, T. Baildon, N. Battaglia, J. A. Beall et al., *Advanced ACTPol Cryogenic Detector Arrays and Readout*, *Journal of Low Temperature Physics* (Mar., 2016) , [1510.02809].

[51] A. Merloni, P. Predehl, W. Becker, H. Böhringer, T. Boller, H. Brunner et al., *eROSITA Science Book: Mapping the Structure of the Energetic Universe*, *ArXiv e-prints* (Sept., 2012) , [1209.3114].

[52] DES collaboration, T. Abbott et al., *The Dark Energy Survey: more than dark energy - an overview*, *Mon. Not. Roy. Astron. Soc.* (2016) , [1601.00329].

[53] N. Kaiser, H. Aussel, B. E. Burke, H. Boesgaard, K. Chambers, M. R. Chun et al., *Pan-STARRS: A Large Synoptic Survey Telescope Array*, in *Survey and Other Telescope Technologies and Discoveries* (J. A. Tyson and S. Wolff, eds.), vol. 4836 of *Proc. SPIE*, pp. 154–164, Dec., 2002. DOI.

[54] LSST Science Collaboration, P. A. Abell, J. Allison, S. F. Anderson, J. R. Andrew, J. R. P. Angel et al., *LSST Science Book, Version 2.0*, *ArXiv e-prints* (Dec., 2009) , [0912.0201].

[55] M. D. Gladders and H. K. C. Yee, *The Red-Sequence Cluster Survey. I. The Survey and Cluster Catalogs for Patches RCS 0926+37 and RCS 1327+29*, *ApJS* **157** (Mar., 2005) 1–29, [astro-ph/0411075].

[56] B. P. Koester, T. A. McKay, J. Annis, R. H. Wechsler, A. Evrard, L. Bleem et al., *A MaxBCG Catalog of 13,823 Galaxy Clusters from the Sloan Digital Sky Survey*, *ApJ* **660** (May, 2007) 239–255, [astro-ph/0701265].

[57] L. E. Bleem, B. Stalder, M. Brodwin, M. T. Busha, M. D. Gladders, F. W. High et al., *A New Reduction of the Blanco Cosmology Survey: An Optically Selected Galaxy Cluster Catalog and a Public Release of Optical Data Products*, *ApJS* **216** (Jan., 2015) 20, [1403.7186].

[58] E. S. Rykoff, E. Rozo, D. Hollowood, A. Bermeo-Hernandez, T. Jeltema, J. Mayers et al., *The redMaPPer Galaxy Cluster Catalog From DES Science Verification Data*, *ArXiv e-prints* (Jan., 2016) , [1601.00621].

[59] C. Bonnett, M. A. Troxel, W. Hartley, A. Amara, B. Leistedt, M. R. Becker et al., *Redshift distributions of galaxies in the DES Science Verification shear catalogue and implications for weak*

lensing, ArXiv e-prints (July, 2015) , [1507.05909].

[60] D. Huterer, A. Kim, L. M. Krauss and T. Broderick, *Redshift Accuracy Requirements for Future Supernova and Number Count Surveys, ApJ* **615** (Nov., 2004) 595–602, [astro-ph/0402002].

[61] M. Lima and W. Hu, *Photometric redshift requirements for self-calibration of cluster dark energy studies, Phys. Rev. D* **76** (Dec., 2007) 123013, [0709.2871].

[62] J. Shao, P. Zhang, W. Lin and Y. Jing, *The Thermal Sunyaev-Zel'dovich Tomography, ApJ* **730** (Apr., 2011) 127, [0903.5317].

[63] A. Hajian, N. Battaglia, D. N. Spergel, J. R. Bond, C. Pfrommer and J. L. Sievers, *Measuring the thermal Sunyaev-Zel'dovich effect through the cross correlation of Planck and WMAP maps with ROSAT galaxy cluster catalogs, JCAP* **11** (Nov., 2013) 64, [1309.3282].

[64] J. L. Sievers, R. A. Hlozek, M. R. Nolta, V. Acquaviva, G. E. Addison, P. A. R. Ade et al., *The Atacama Cosmology Telescope: cosmological parameters from three seasons of data, JCAP* **10** (Oct., 2013) 60, [1301.0824].

[65] E. M. George, C. L. Reichardt, K. A. Aird, B. A. Benson, L. E. Bleem, J. E. Carlstrom et al., *A Measurement of Secondary Cosmic Microwave Background Anisotropies from the 2500 Square-degree SPT-SZ Survey, ApJ* **799** (Feb., 2015) 177, [1408.3161].

[66] Planck Collaboration, N. Aghanim, M. Arnaud, M. Ashdown, J. Aumont, C. Baccigalupi et al., *Planck 2015 results. XXII. A map of the thermal Sunyaev-Zeldovich effect, ArXiv:1502.01596* (Feb., 2015) , [1502.01596].

[67] M. J. Wilson, B. D. Sherwin, J. C. Hill, G. Addison, N. Battaglia, J. R. Bond et al., *Atacama Cosmology Telescope: A measurement of the thermal Sunyaev-Zel'dovich effect using the skewness of the CMB temperature distribution, Phys. Rev. D* **86** (Dec., 2012) 122005, [1203.6633].

[68] T. M. Crawford, K. K. Schaffer, S. Bhattacharya, K. A. Aird, B. A. Benson, L. E. Bleem et al., *A Measurement of the Secondary-CMB and Millimeter-wave-foreground Bispectrum using 800 deg^2 of South Pole Telescope Data, ApJ* **784** (Apr., 2014) 143, [1303.3535].

[69] J. C. Hill, B. D. Sherwin, K. M. Smith, G. E. Addison, N. Battaglia, E. S. Battistelli et al., *The Atacama Cosmology Telescope: A Measurement of the Thermal Sunyaev-Zel'dovich One-Point PDF, ArXiv:1411.8004* (Nov., 2014) , [1411.8004].

[70] N. Battaglia, J. R. Bond, C. Pfrommer, J. L. Sievers and D. Sijacki, *Simulations of the Sunyaev-Zel'dovich Power Spectrum with Active Galactic Nucleus Feedback, ApJ* **725** (Dec., 2010) 91–99, [1003.4256].

[71] J. C. Hill and E. Pajer, *Cosmology from the thermal Sunyaev-Zel'dovich power spectrum: Primordial non-Gaussianity and massive neutrinos, Phys. Rev. D* **88** (Sept., 2013) 063526, [1303.4726].

[72] I. G. McCarthy, A. M. C. Le Brun, J. Schaye and G. P. Holder, *The thermal Sunyaev-Zel'dovich effect power spectrum in light of Planck, MNRAS* **440** (June, 2014) 3645–3657, [1312.5341].

[73] M. Fukugita and P. J. E. Peebles, *The Cosmic Energy Inventory, ApJ* **616** (Dec., 2004) 643–668, [astro-ph/0406095].

[74] K. Osato, M. Shirasaki and N. Yoshida, *Impact of Baryonic Processes on Weak-lensing Cosmology: Power Spectrum, Nonlocal Statistics, and Parameter Bias, ApJ* **806** (June, 2015) 186, [1501.02055].

[75] T. Eifler, E. Krause, S. Dodelson, A. R. Zentner, A. P. Hearin and N. Y. Gnedin, *Accounting for baryonic effects in cosmic shear tomography: determining a minimal set of nuisance parameters using*

PCA, *MNRAS* **454** (Dec., 2015) 2451–2471, [`1405.7423`].

[76] R. A. Sunyaev and Y. B. Zeldovich, *The Observations of Relic Radiation as a Test of the Nature of X-Ray Radiation from the Clusters of Galaxies*, *Comments on Astrophysics and Space Physics* **4** (Nov., 1972) 173.

[77] J. P. Ostriker and E. T. Vishniac, *Generation of microwave background fluctuations from nonlinear perturbations at the ERA of galaxy formation*, *ApJ* **306** (July, 1986) L51–L54.

[78] S. Ho, S. Dedeo and D. Spergel, *Finding the Missing Baryons Using CMB as a Backlight*, *ArXiv e-prints* (Mar., 2009) , [`0903.2845`].

[79] J. Shao, P. Zhang, W. Lin, Y. Jing and J. Pan, *Kinetic Sunyaev-Zel'dovich tomography with spectroscopic redshift surveys*, *MNRAS* **413** (May, 2011) 628–642, [`1004.1301`].

[80] M. Li, R. E. Angulo, S. D. M. White and J. Jasche, *Matched filter optimization of kSZ measurements with a reconstructed cosmological flow field*, *MNRAS* **443** (Sept., 2014) 2311–2326, [`1404.0007`].

[81] P. G. Ferreira, R. Juszkiewicz, H. A. Feldman, M. Davis and A. H. Jaffe, *Streaming Velocities as a Dynamical Estimator of* Ω, *ApJ* **515** (Apr., 1999) L1–L4, [`astro-ph/9812456`].

[82] S. Bhattacharya and A. Kosowsky, *Dark energy constraints from galaxy cluster peculiar velocities*, *Phys. Rev. D* **77** (Apr., 2008) 083004, [`0712.0034`].

[83] E. Schaan, S. Ferraro, M. Vargas-Magaña, K. M. Smith, S. Ho, S. Aiola et al., *Evidence for the kinematic Sunyaev-Zel'dovich effect with ACTPol and velocity reconstruction from BOSS*, *ArXiv e-prints* (Oct., 2015) , [`1510.06442`].

[84] O. Doré, J. Bock, M. Ashby, P. Capak, A. Cooray, R. de Putter et al., *Cosmology with the SPHEREX All-Sky Spectral Survey*, *ArXiv e-prints* (Dec., 2014) , [`1412.4872`].

[85] N. Hand, G. E. Addison, E. Aubourg, N. Battaglia, E. S. Battistelli, D. Bizyaev et al., *Evidence of Galaxy Cluster Motions with the Kinematic Sunyaev-Zel'dovich Effect*, *Physical Review Letters* **109** (July, 2012) 041101, [`1203.4219`].

[86] Planck Collaboration, P. A. R. Ade, N. Aghanim, M. Arnaud, M. Ashdown, E. Aubourg et al., *Planck intermediate results. XXXVII. Evidence of unbound gas from the kinetic Sunyaev-Zeldovich effect*, *A&A* **586** (Feb., 2016) A140, [`1504.03339`].

[87] B. Soergel, S. Flender, K. T. Story, L. Bleem, T. Giannantonio, G. Efstathiou et al., *Detection of the kinematic Sunyaev-Zel'dovich effect with DES Year 1 and SPT*, *ArXiv e-prints* (Mar., 2016) , [`1603.03904`].

[88] O. Doré, J. F. Hennawi and D. N. Spergel, *Beyond the Damping Tail: Cross-Correlating the Kinetic Sunyaev-Zel'dovich Effect with Cosmic Shear*, *ApJ* **606** (May, 2004) 46–57, [`astro-ph/0309337`].

[89] J. C. Hill, S. Ferraro, N. Battaglia, J. Liu and D. N. Spergel, *The Kinematic Sunyaev-Zel'dovich Effect with Projected Fields: A Novel Probe of the Baryon Distribution with Planck, WMAP, and WISE Data*, *ArXiv e-prints* (Mar., 2016) , [`1603.01608`].

[90] S. Ferraro, J. C. Hill, N. Battaglia, J. Liu and D. N. Spergel, *The Kinematic Sunyaev-Zel'dovich Effect with Projected Fields II: prospects, challenges, and comparison with simulations*, *ArXiv e-prints* (May, 2016) , [`1605.02722`].

[91] Planck Collaboration, P. A. R. Ade, N. Aghanim, M. Arnaud, M. Ashdown, J. Aumont et al., *Planck 2015 results. XV. Gravitational lensing*, *ArXiv e-prints* (Feb., 2015) , [`1502.01591`].

[92] R. Caldwell, A. Cooray and A. Melchiorri, *Constraints on a New Post-General Relativity*

Cosmological Parameter, *Phys. Rev.* **D76** (2007) 023507, [`astro-ph/0703375`].

[93] E. Bertschinger, *On the Growth of Perturbations as a Test of Dark Energy*, *Astrophys. J.* **648** (2006) 797–806, [`astro-ph/0604485`].

[94] J.-P. Uzan and F. Bernardeau, *Lensing at cosmological scales: A test of higher dimensional gravity*, *Phys. Rev. D* **64** (Sep, 2001) 083004.

[95] W. Hu, *Dark synergy: Gravitational lensing and the cmb*, *Phys. Rev. D* **65** (Dec, 2001) 023003.

[96] T. Clifton, P. G. Ferreira, A. Padilla and C. Skordis, *Modified gravity and cosmology*, *Phys. Rep.* **513** (Mar., 2012) 1–189, [`1106.2476`].

[97] E. Bertschinger and P. Zukin, *Distinguishing modified gravity from dark energy*, *Phys. Rev. D* **78** (July, 2008) 024015, [`0801.2431`].

[98] W. J. Percival, L. Samushia, A. J. Ross, C. Shapiro and A. Raccanelli, *Redshift-space distortions*, *Philosophical Transactions of the Royal Society of London Series A* **369** (Dec., 2011) 5058–5067.

[99] J. Yoo, A. L. Fitzpatrick and M. Zaldarriaga, *New perspective on galaxy clustering as a cosmological probe: General relativistic effects*, *Phys. Rev. D* **80** (Oct., 2009) 083514, [`0907.0707`].

[100] E. Villa, L. Verde and S. Matarrese, *General relativistic corrections and non-Gaussianity in large-scale structure*, *Classical and Quantum Gravity* **31** (Dec., 2014) 234005, [`1409.4738`].

[101] D. Alonso, P. Bull, P. G. Ferreira, R. Maartens and M. G. Santos, *Ultra-large-scale Cosmology in Next-generation Experiments with Single Tracers*, *ApJ* **814** (Dec., 2015) 145, [`1505.07596`].

[102] A. Raccanelli, F. Montanari, D. Bertacca, O. Doré and R. Durrer, *Cosmological measurements with general relativistic galaxy correlations*, *JCAP* **5** (May, 2016) 009, [`1505.06179`].

[103] L. Lombriser, J. Yoo and K. Koyama, *Relativistic effects in galaxy clustering in a parametrized post-Friedmann universe*, *Phys. Rev. D* **87** (May, 2013) 104019, [`1301.3132`].

[104] T. Baker and P. Bull, *Observational Signatures of Modified Gravity on Ultra-large Scales*, *ApJ* **811** (Oct., 2015) 116, [`1506.00641`].

[105] J. Renk, M. Zumalacarregui and F. Montanari, *Gravity at the horizon: on relativistic effects, CMB-LSS correlations and ultra-large scales in Horndeski's theory*, *ArXiv e-prints* (Apr., 2016) , [`1604.03487`].

[106] S. J. Tingay, R. Goeke, J. D. Bowman, D. Emrich, S. M. Ord, D. A. Mitchell et al., *The murchison widefield array: The square kilometre array precursor at low radio frequencies*, *PASA* **30** (1, 2013) .

[107] Z. S. Ali, A. R. Parsons, H. Zheng, J. C. Pober, A. Liu, J. E. Aguirre et al., *PAPER-64 Constraints on Reionization: The 21 cm Power Spectrum at z = 8.4*, *ApJ* **809** (Aug., 2015) 61, [`1502.06016`].

[108] M. P. van Haarlem, M. W. Wise, A. W. Gunst, G. Heald, J. P. McKean, J. W. T. Hessels et al., *LOFAR: The LOw-Frequency ARray*, *A&A* **556** (Aug., 2013) A2, [`1305.3550`].

[109] G. Paciga, T.-C. Chang, Y. Gupta, R. Nityanada, J. Odegova, U.-L. Pen et al., *The gmrt epoch of reionization experiment: a new upper limit on the neutral hydrogen power spectrum at z??? 8.6*, *MNRAS* **413** (2011) 1174–1183, [`http://mnras.oxfordjournals.org/content/413/2/1174.full.pdf+html`].

[110] J. C. Pober, A. Liu, J. S. Dillon, J. E. Aguirre, J. D. Bowman, R. F. Bradley et al., *What next-generation 21 cm power spectrum measurements can teach us about the epoch of reionization*, *ApJ* **782** (2014) 66.

[111] A. R. Neben, R. F. Bradley, J. N. Hewitt, D. R. DeBoer, A. R. Parsons, J. E. Aguirre et al., *The Hydrogen Epoch of Reionization Array Dish I: Beam Pattern Measurements and Science Implications*, *ArXiv e-prints* (Feb., 2016) , [1602.03887].

[112] A. Ewall-Wice, R. Bradley, D. DeBoer, J. Hewitt, A. Parsons, J. Aguirre et al., *The HERA Dish II: Electromagnetic Simulations and Science Implications*, *ArXiv e-prints* (Feb., 2016) , [1602.06277].

[113] M. B. Silva, M. G. Santos, Y. Gong, A. Cooray and J. Bock, *Intensity Mapping of Lyα Emission during the Epoch of Reionization*, *ApJ* **763** (Feb., 2013) 132, [1205.1493].

[114] E. R. Fernandez, S. Zaroubi, I. T. Iliev, G. Mellema and V. Jelić, *Stars and reionization: the cross-correlation of the 21 cm line and the near-infrared background*, *MNRAS* **440** (May, 2014) 298–306, [1312.3549].

[115] X.-C. Mao, *Probing Reionization with the Cross-power Spectrum of 21 cm and Near-infrared Radiation Backgrounds*, *ApJ* **790** (Aug., 2014) 148, [1406.4215].

[116] A. Kashlinsky, R. G. Arendt, J. Mather and S. H. Moseley, *Tracing the first stars with fluctuations of the cosmic infrared background*, *Nature* **438** (Nov., 2005) 45–50, [astro-ph/0511105].

[117] A. Kashlinsky, R. G. Arendt, J. Mather and S. H. Moseley, *New Measurements of Cosmic Infrared Background Fluctuations from Early Epochs*, *ApJ* **657** (Mar., 2007) L131–L131, [astro-ph/0612445].

[118] A. Kashlinsky, R. G. Arendt, M. L. N. Ashby, G. G. Fazio, J. Mather and S. H. Moseley, *New Measurements of the Cosmic Infrared Background Fluctuations in Deep Spitzer/IRAC Survey Data and Their Cosmological Implications*, *ApJ* **753** (July, 2012) 63, [1201.5617].

[119] K. Helgason, M. Ricotti, A. Kashlinsky and V. Bromm, *On the physical requirements for a pre-reionization origin of the unresolved near-infrared background*, *MNRAS* **455** (Jan., 2016) 282–294, [1505.07226].

[120] A. Cooray, J. Smidt, F. De Bernardis, Y. Gong, D. Stern, M. L. N. Ashby et al., *A measurement of the intrahalo light fraction with near-infrared background anisotropies*, *ArXiv e-prints* (Oct., 2012) , [1210.6031].

[121] M. Zemcov, J. Smidt, T. Arai, J. Bock, A. Cooray, Y. Gong et al., *On the origin of near-infrared extragalactic background light anisotropy*, *Science* **346** (Nov., 2014) 732–735, [1411.1411].

[122] A. Beardsley, *The Murchison Widefield Array 21cm Epoch of Reionization Experiment: Design, Construction, and First Season Results.* PhD thesis, University of Washington, 2015.

[123] W. Li, A. V. Filippenko, R. Chornock, E. Berger, P. Berlind, M. L. Calkins et al., *SN 2002cx: The Most Peculiar Known Type Ia Supernova*, *PASP* **115** (Apr., 2003) 453–473, [astro-ph/0301428].

[124] M. Sullivan, A. Conley, D. A. Howell, J. D. Neill, P. Astier, C. Balland et al., *The dependence of Type Ia Supernovae luminosities on their host galaxies*, *MNRAS* **406** (Aug., 2010) 782–802, [1003.5119].

[125] E. Cappellaro, M. T. Botticella, G. Pignata, A. Grado, L. Greggio, L. Limatola et al., *Supernova rates from the SUDARE VST-OmegaCAM search. I. Rates per unit volume*, *A&A* **584** (Dec., 2015) A62, [1509.04496].

[126] E. Y. Hsiao, A. Conley, D. A. Howell, M. Sullivan, C. J. Pritchet, R. G. Carlberg et al., *K-Corrections and Spectral Templates of Type Ia Supernovae*, *ApJ* **663** (July, 2007) 1187–1200, [astro-ph/0703529].

[127] P. Hoeflich, A. M. Khokhlov and J. C. Wheeler, *Delayed detonation models for normal and subluminous type IA sueprnovae: Absolute brightness, light curves, and molecule formation*, *ApJ* **444**

(May, 1995) 831–847.

[128] D. Kasen, *Secondary Maximum in the Near-Infrared Light Curves of Type Ia Supernovae*, *ApJ* **649** (Oct., 2006) 939–953, [`astro-ph/0606449`].

[129] C. L. Gerardy, W. P. S. Meikle, R. Kotak, P. Höflich, D. Farrah, A. V. Filippenko et al., *Signatures of Delayed Detonation, Asymmetry, and Electron Capture in the Mid-Infrared Spectra of Supernovae 2003hv and 2005df*, *ApJ* **661** (June, 2007) 995–1012, [`astro-ph/0702117`].

[130] C. M. Telesco, P. Höflich, D. Li, C. Álvarez, C. M. Wright, P. J. Barnes et al., *Mid-IR Spectra of Type Ia SN 2014J in M82 Spanning the First 4 Months*, *ApJ* **798** (Jan., 2015) 93, [`1409.2125`].

[131] C. M. Sharp and P. Hoeflich, *Molecular bands of supernova 1987 A*, *Ap&SS* **171** (Sept., 1990) 213–216.

[132] C. L. Gerardy, R. A. Fesen, P. Höflich and J. C. Wheeler, *Detection of CO and Dust Emission in Near-Infrared Spectra of SN 1998S*, *AJ* **119** (June, 2000) 2968–2981, [`astro-ph/9912433`].

[133] M. Stritzinger et al., *Optical photometry of the type ia supernova 1999ee and the type ib/c supernova 1999ex in ic 5179*, AJ **124** (2002) 2100.

[134] M. D. Stritzinger, M. M. Phillips, L. N. Boldt, C. Burns, A. Campillay, C. Contreras et al., *The Carnegie Supernova Project: Second Photometry Data Release of Low-redshift Type Ia Supernovae*, *AJ* **142** (Nov., 2011) 156, [`1108.3108`].

[135] M. D. Stritzinger, S. Valenti, P. Hoeflich, E. Baron, M. M. Phillips, F. Taddia et al., *Comprehensive observations of the bright and energetic Type Iax SN 2012Z: Interpretation as a Chandrasekhar mass white dwarf explosion*, *A&A* **573** (Jan., 2015) A2, [`1408.1093`].

[136] T. P. Robitaille, E. Churchwell, R. A. Benjamin, B. A. Whitney, K. Wood, B. L. Babler et al., *A self-consistent model of Galactic stellar and dust infrared emission and the abundance of polycyclic aromatic hydrocarbons*, *A&A* **545** (Sept., 2012) A39, [`1208.4606`].

[137] E. Churchwell, M. S. Povich, D. Allen, M. G. Taylor, M. R. Meade, B. L. Babler et al., *The Bubbling Galactic Disk*, *ApJ* **649** (Oct., 2006) 759–778.

[138] E. Churchwell, B. L. Babler, M. R. Meade, B. A. Whitney, R. Benjamin, R. Indebetouw et al., *The Spitzer/GLIMPSE Surveys: A New View of the Milky Way*, *PASP* **121** (Mar., 2009) 213–230.

[139] E. Peeters, L. J. Allamandola, C. W. Bauschlicher, Jr., D. M. Hudgins, S. A. Sandford and A. G. G. M. Tielens, *Deuterated Interstellar Polycyclic Aromatic Hydrocarbons*, *ApJ* **604** (Mar., 2004) 252–257.

[140] B. T. Draine, *Can Dust Explain Variations in the D/H Ratio?*, in *Astrophysics in the Far Ultraviolet: Five Years of Discovery with FUSE* (G. Sonneborn, H. W. Moos and B.-G. Andersson, eds.), vol. 348 of *Astronomical Society of the Pacific Conference Series*, p. 58, June, 2006.

[141] G. Hébrard, *Deuterium variations in the interstellar medium of the Milky Way*, in *Astrophysics in the Far Ultraviolet: Five Years of Discovery with FUSE* (G. Sonneborn, H. W. Moos and B.-G. Andersson, eds.), vol. 348 of *Astronomical Society of the Pacific Conference Series*, p. 47, June, 2006.

[142] K. D. Doney, A. Candian, T. Mori, T. Onaka and A. G. G. M. Tielens, *Deuterated polycyclic aromatic hydrocarbons: Revisited*, *A&A* **586** (Feb., 2016) A65, [`1512.02874`].

[143] A. J. Adamson, D. C. B. Whittet, A. Chrysostomou, J. H. Hough, D. K. Aitken, G. S. Wright et al., *Spectropolarimetric Constraints on the Nature of the 3.4 Micron Absorber in the Interstellar Medium*, *ApJ* **512** (Feb., 1999) 224–229.

[144] J. E. Chiar, A. J. Adamson, D. C. B. Whittet, A. Chrysostomou, J. H. Hough, T. H. Kerr et al., *Spectropolarimetry of the 3.4 µm Feature in the Diffuse ISM toward the Galactic Center Quintuplet Cluster*, *ApJ* **651** (Nov., 2006) 268–271, [`astro-ph/0607245`].

[145] J. E. Chiar, Y. J. Pendleton, T. R. Geballe and A. G. G. M. Tielens, *Near-Infrared Spectroscopy of the Proto-Planetary Nebula CRL 618 and the Origin of the Hydrocarbon Dust Component in the Interstellar Medium*, *ApJ* **507** (Nov., 1998) 281–286.

[146] E. L. O. Bakes and A. G. G. M. Tielens, *The Effects of Polycyclic Aromatic Hydrocarbons on the Chemistry of Photodissociation Regions*, *ApJ* **499** (May, 1998) 258–266.

[147] M. G. Wolfire, A. G. G. M. Tielens, D. Hollenbach and M. J. Kaufman, *Chemical Rates on Small Grains and PAHs: C^+ Recombination and H_2 Formation*, *ApJ* **680** (June, 2008) 384–397, [`0803.0138`].

[148] V. Le Page, T. P. Snow and V. M. Bierbaum, *Molecular Hydrogen Formation Catalyzed by Polycyclic Aromatic Hydrocarbons in the Interstellar Medium*, *ApJ* **704** (Oct., 2009) 274–280.

[149] E. L. O. Bakes and A. G. G. M. Tielens, *The photoelectric heating mechanism for very small graphitic grains and polycyclic aromatic hydrocarbons*, *ApJ* **427** (June, 1994) 822–838.

[150] M. G. Wolfire, D. Hollenbach, C. F. McKee, A. G. G. M. Tielens and E. L. O. Bakes, *The neutral atomic phases of the interstellar medium*, *ApJ* **443** (Apr., 1995) 152–168.

[151] J. D. T. Smith, B. T. Draine, D. A. Dale, J. Moustakas, R. C. Kennicutt, Jr., G. Helou et al., *The Mid-Infrared Spectrum of Star-forming Galaxies: Global Properties of Polycyclic Aromatic Hydrocarbon Emission*, *ApJ* **656** (Feb., 2007) 770–791, [`astro-ph/0610913`].

[152] A. G. G. M. Tielens, *Interstellar Polycyclic Aromatic Hydrocarbon Molecules*, *ARA&A* **46** (Sept., 2008) 289–337.

[153] K. V. Croxall, J. D. Smith, M. G. Wolfire, H. Roussel, K. M. Sandstrom, B. T. Draine et al., *Resolving the Far-IR Line Deficit: Photoelectric Heating and Far-IR Line Cooling in NGC 1097 and NGC 4559*, *ApJ* **747** (Mar., 2012) 81, [`1201.1016`].

[154] P. Beirão, L. Armus, G. Helou, P. N. Appleton, J.-D. T. Smith, K. V. Croxall et al., *A Study of Heating and Cooling of the ISM in NGC 1097 with Herschel-PACS and Spitzer-IRS*, *ApJ* **751** (June, 2012) 144, [`1204.0554`].

[155] K. M. Sandstrom, A. D. Bolatto, C. Bot, B. T. Draine, J. G. Ingalls, F. P. Israel et al., *The Spitzer Spectroscopic Survey of the Small Magellanic Cloud (S^4MC): Probing the Physical State of Polycyclic Aromatic Hydrocarbons in a Low-metallicity Environment*, *ApJ* **744** (Jan., 2012) 20, [`1109.0999`].

[156] B. T. Draine and A. Li, *Infrared Emission from Interstellar Dust. IV. The Silicate-Graphite-PAH Model in the Post-Spitzer Era*, *ApJ* **657** (Mar., 2007) 810–837, [`astro-ph/0608003`].

[157] C. W. Engelbracht, K. D. Gordon, G. H. Rieke, M. W. Werner, D. A. Dale and W. B. Latter, *Metallicity Effects on Mid-Infrared Colors and the 8 µm PAH Emission in Galaxies*, *ApJ* **628** (July, 2005) L29–L32, [`astro-ph/0506214`].

[158] S. C. Madden, F. Galliano, A. P. Jones and M. Sauvage, *ISM properties in low-metallicity environments*, *A&A* **446** (Feb., 2006) 877–896, [`astro-ph/0510086`].

[159] C. W. Engelbracht, G. H. Rieke, K. D. Gordon, J.-D. T. Smith, M. W. Werner, J. Moustakas et al., *Metallicity Effects on Dust Properties in Starbursting Galaxies*, *ApJ* **678** (May, 2008) 804–827, [`0801.1700`].

[160] K. M. Sandstrom, A. D. Bolatto, B. T. Draine, C. Bot and S. Stanimirović, *The Spitzer Survey of the Small Magellanic Cloud (S^3MC): Insights into the Life Cycle of Polycyclic Aromatic Hydrocarbons*, *ApJ* **715** (June, 2010) 701–723, [1003.4516].

[161] C. J. Cyganowski, B. A. Whitney, E. Holden, E. Braden, C. L. Brogan, E. Churchwell et al., *A Catalog of Extended Green Objects in the GLIMPSE Survey: A New Sample of Massive Young Stellar Object Outflow Candidates*, *AJ* **136** (Dec., 2008) 2391–2412, [0810.0530].

[162] H.-T. Lee, M. Takami, H.-Y. Duan, J. Karr, Y.-N. Su, S.-Y. Liu et al., *Near-infrared H_2 and Continuum Survey of Extended Green Objects*, *ApJS* **200** (May, 2012) 2, [1203.2416].

[163] D. Froebrich, S. V. Makin, C. J. Davis, T. M. Gledhill, Y. Kim, B.-C. Koo et al., *Extended H_2 emission line sources from UWISH2*, *MNRAS* **454** (Dec., 2015) 2586–2605.

[164] J.-J. Lee, B.-C. Koo, Y.-H. Lee, H.-G. Lee, J.-H. Shinn, H.-J. Kim et al., *UKIRT Widefield Infrared Survey for Fe^+*, *MNRAS* **443** (Sept., 2014) 2650–2660, [1406.4271].

[165] D. R. Mizuno, K. E. Kraemer, N. Flagey, N. Billot, S. Shenoy, R. Paladini et al., *A Catalog of MIPSGAL Disk and Ring Sources*, *AJ* **139** (Apr., 2010) 1542–1552, [1002.4421].

[166] N. Flagey, A. Noriega-Crespo, A. Petric and T. R. Geballe, *Palomar/TripleSpec Observations of Spitzer/MIPSGAL 24 μm Circumstellar Shells: Unveiling the Natures of Their Central Sources*, *AJ* **148** (Aug., 2014) 34, [1405.4023].

[167] C. R. Kerton, G. Wolf-Chase, K. Arvidsson, C. J. Lintott and R. J. Simpson, *The Milky Way Project: What are Yellowballs?*, *ApJ* **799** (Feb., 2015) 153.

[168] G. M. Green, E. F. Schlafly, D. P. Finkbeiner, H.-W. Rix, N. Martin, W. Burgett et al., *A Three-dimensional Map of Milky Way Dust*, *ApJ* **810** (Sept., 2015) 25, [1507.01005].

[169] A. C. A. Boogert, T. L. Huard, A. M. Cook, J. E. Chiar, C. Knez, L. Decin et al., *Ice and Dust in the Quiescent Medium of Isolated Dense Cores*, *ApJ* **729** (Mar., 2011) 92, [1101.2486].

[170] J. C. Weingartner and B. T. Draine, *Dust Grain-Size Distributions and Extinction in the Milky Way, Large Magellanic Cloud, and Small Magellanic Cloud*, *ApJ* **548** (Feb., 2001) 296–309, [astro-ph/0008146].

[171] M. Xue, B. Jiang, J. Gao, J. Liu, S. Wang and A. Li, *A Precise Determination of the Mid-Infrared Interstellar Extinction Law Based on the APOGEE Spectroscopic Survey*, *ArXiv e-prints* (Feb., 2016) , [1602.02928].

[172] S. Wang, A. Li and B. W. Jiang, *The interstellar oxygen crisis, or where have all the oxygen atoms gone?*, *MNRAS* **454** (Nov., 2015) 569–575, [1508.03404].

[173] S. Wang, A. Li and B. W. Jiang, *Very Large Interstellar Grains as Evidenced by the Mid-infrared Extinction*, *ApJ* **811** (Sept., 2015) 38, [1508.03403].

[174] L. Pagani, J. Steinacker, A. Bacmann, A. Stutz and T. Henning, *The Ubiquity of Micrometer-Sized Dust Grains in the Dense Interstellar Medium*, *Science* **329** (Sept., 2010) 1622, [1110.4180].

[175] R. F. Knacke, S. McCorkle, R. C. Puetter, E. F. Erickson and W. Kraetschmer, *Observation of interstellar ammonia ice*, *ApJ* **260** (Sept., 1982) 141–146.

[176] Y. J. Pendleton, A. G. G. M. Tielens and M. W. Werner, *Studies of dust grain properties in infrared reflection nebulae*, *ApJ* **349** (Jan., 1990) 107–119.

[177] J. Pepper, R. J. Siverd, T. G. Beatty, B. S. Gaudi, K. G. Stassun, J. Eastman et al., *KELT-3b: A Hot Jupiter Transiting a V = 9.8 Late-F Star*, *ApJ* **773** (Aug., 2013) 64, [1211.1031].

[178] T. S. Boyajian, K. von Braun, G. van Belle, C. Farrington, G. Schaefer, J. Jones et al., *Stellar Diameters and Temperatures. III. Main-sequence A, F, G, and K Stars: Additional High-precision Measurements and Empirical Relations*, *ApJ* **771** (July, 2013) 40, [1306.2974].

[179] N. Yoshida, K. Omukai, L. Hernquist and T. Abel, *Formation of Primordial Stars in a ΛCDM Universe*, *ApJ* **652** (Nov., 2006) 6–25, [astro-ph/0606106].

[180] A. Heger and S. E. Woosley, *Nucleosynthesis and Evolution of Massive Metal-free Stars*, *ApJ* **724** (Nov., 2010) 341–373, [0803.3161].

[181] S. G. Ryan, J. E. Norris and T. C. Beers, *The Spite Lithium Plateau: Ultrathin but Postprimordial*, *ApJ* **523** (Oct., 1999) 654–677, [astro-ph/9903059].

[182] R. Cayrel, E. Depagne, M. Spite, V. Hill, F. Spite, P. François et al., *First stars V - Abundance patterns from C to Zn and supernova yields in the early Galaxy*, *A&A* **416** (Mar., 2004) 1117–1138, [astro-ph/0311082].

[183] K. C. Schlaufman and A. R. Casey, *The Best and Brightest Metal-poor Stars*, *ApJ* **797** (Dec., 2014) 13, [1409.4775].

[184] J. Tumlinson, *Chemical Evolution in Hierarchical Models of Cosmic Structure. II. The Formation of the Milky Way Stellar Halo and the Distribution of the Oldest Stars*, *ApJ* **708** (Jan., 2010) 1398–1418, [0911.1786].

[185] A. R. Casey and K. C. Schlaufman, *Chemistry of the Most Metal-poor Stars in the Bulge and the z gsim 10 Universe*, *ApJ* **809** (Aug., 2015) 110, [1509.01252].

[186] I. Brott and P. H. Hauschildt, *A PHOENIX Model Atmosphere Grid for Gaia*, in *The Three-Dimensional Universe with Gaia* (C. Turon, K. S. O'Flaherty and M. A. C. Perryman, eds.), vol. 576 of *ESA Special Publication*, p. 565, Jan., 2005. astro-ph/0503395.

[187] M. C. Cushing, T. L. Roellig, M. S. Marley, D. Saumon, S. K. Leggett, J. D. Kirkpatrick et al., *A Spitzer Infrared Spectrograph Spectral Sequence of M, L, and T Dwarfs*, *ApJ* **648** (Sept., 2006) 614–628, [astro-ph/0605639].

[188] T. J. Dupuy and A. L. Kraus, *Distances, Luminosities, and Temperatures of the Coldest Known Substellar Objects*, *Science* **341** (Sept., 2013) 1492–1495, [1309.1422].

[189] P. Tremblin, D. S. Amundsen, G. Chabrier, I. Baraffe, B. Drummond, S. Hinkley et al., *Cloudless Atmospheres for L/T Dwarfs and Extrasolar Giant Planets*, *ApJ* **817** (Feb., 2016) L19, [1601.03652].

[190] D. Saumon, M. S. Marley and K. Lodders, *The Mid-Infrared Spectra of Brown Dwarfs*, *ArXiv Astrophysics e-prints* (Oct., 2003) , [astro-ph/0310805].

[191] S. Sorahana, I. Yamamura and H. Murakami, *On the Radii of Brown Dwarfs Measured with AKARI Near-infrared Spectroscopy*, *ApJ* **767** (Apr., 2013) 77, [1304.1259].

[192] J. D. Kirkpatrick, A. Schneider, S. Fajardo-Acosta, C. R. Gelino, G. N. Mace, E. L. Wright et al., *The AllWISE Motion Survey and the Quest for Cold Subdwarfs*, *ApJ* **783** (Mar., 2014) 122, [1402.0661].

[193] J. D. Kirkpatrick, K. Kellogg, A. C. Schneider, S. Fajardo-Acosta, M. C. Cushing, J. Greco et al., *The AllWISE Motion Survey, Part 2*, *ArXiv e-prints* (Mar., 2016) , [1603.08040].

[194] J. K. Faherty, E. L. Rice, K. L. Cruz, E. E. Mamajek and A. Núñez, *2MASS J035523.37+113343.7: A Young, Dusty, Nearby, Isolated Brown Dwarf Resembling a Giant Exoplanet*, *AJ* **145** (Jan., 2013) 2, [1206.5519].

[195] K. L. Luhman, *Discovery of a ˜250 K Brown Dwarf at 2 pc from the Sun*, *ApJ* **786** (May, 2014) L18,

[1404.6501].

[196] H. Y. A. Meng, K. Y. L. Su, G. H. Rieke, W. Rujopakarn, G. Myers, M. Cook et al., *Planetary Collisions Outside the Solar System: Time Domain Characterization of Extreme Debris Disks*, *ApJ* **805** (May, 2015) 77, [1503.05610].

[197] C. M. Lisse, C. H. Chen, M. C. Wyatt, A. Morlok, I. Song, G. Bryden et al., *Abundant Circumstellar Silica Dust and SiO Gas Created by a Giant Hypervelocity Collision in the ˜12 Myr HD172555 System*, *ApJ* **701** (Aug., 2009) 2019–2032, [0906.2536].

[198] B. C. Johnson, C. M. Lisse, C. H. Chen, H. J. Melosh, M. C. Wyatt, P. Thebault et al., *A Self-consistent Model of the Circumstellar Debris Created by a Giant Hypervelocity Impact in the HD 172555 System*, *ApJ* **761** (Dec., 2012) 45, [1210.6258].

[199] M. C. Wyatt, J. S. Greaves, W. R. F. Dent and I. M. Coulson, *Submillimeter Images of a Dusty Kuiper Belt around η Corvi*, *ApJ* **620** (Feb., 2005) 492–500, [astro-ph/0411061].

[200] C. M. Lisse, M. C. Wyatt, C. H. Chen, A. Morlok, D. M. Watson, P. Manoj et al., *Spitzer Evidence for a Late-heavy Bombardment and the Formation of Ureilites in η Corvi at ˜1 Gyr*, *ApJ* **747** (Mar., 2012) 93, [1110.4172].

[201] T. Boyajian, K. von Braun, G. A. Feiden, D. Huber, S. Basu, P. Demarque et al., *Stellar diameters and temperatures - VI. High angular resolution measurements of the transiting exoplanet host stars HD 189733 and HD 209458 and implications for models of cool dwarfs*, *MNRAS* **447** (Feb., 2015) 846–857, [1411.5638].

[202] M. Marengo, A. Hulsebus and S. Willis, *KIC 8462852: The Infrared Flux*, *ApJ* **814** (Nov., 2015) L15, [1511.07908].

[203] C. M. Lisse, M. L. Sitko and M. Marengo, *IRTF/SPeX Observations of the Unusual Kepler Light Curve System KIC8462852*, *ApJ* **815** (Dec., 2015) L27, [1512.00121].

[204] G. M. Kennedy and M. C. Wyatt, *The bright end of the exo-Zodi luminosity function: disc evolution and implications for exo-Earth detectability*, *MNRAS* **433** (Aug., 2013) 2334–2356.

[205] C. M. Lisse, M. L. Sitko, D. J. Christian, C. Melis and C. Chen, *First Results From an IRTF Near-Infrared SPeX Debris Disk Spectral Survey*, in *American Astronomical Society Meeting Abstracts #221*, vol. 221 of *American Astronomical Society Meeting Abstracts*, p. 325.04, Jan., 2013.

[206] J. M. Bauer, T. Grav, E. Blauvelt, A. K. Mainzer, J. R. Masiero, R. Stevenson et al., *Centaurs and Scattered Disk Objects in the Thermal Infrared: Analysis of WISE/NEOWISE Observations*, *ApJ* **773** (Aug., 2013) 22, [1306.1862].

[207] J. M. Bauer, R. Stevenson, E. Kramer, A. K. Mainzer, T. Grav, J. R. Masiero et al., *The NEOWISE-Discovered Comet Population and the CO + CO$_2$ Production Rates*, *ApJ* **814** (Dec., 2015) 85, [1509.08446].

[208] A. Mainzer, J. Bauer, T. Grav, J. Masiero, R. M. Cutri, J. Dailey et al., *Preliminary Results from NEOWISE: An Enhancement to the Wide-field Infrared Survey Explorer for Solar System Science*, *ApJ* **731** (Apr., 2011) 53, [1102.1996].

[209] A. Mainzer, T. Grav, J. Masiero, J. Bauer, R. M. Cutri, R. S. McMillan et al., *Physical Parameters of Asteroids Estimated from the WISE 3-Band Data and NEOWISE Post-Cryogenic Survey*, *ApJ* **760** (Nov., 2012) L12, [1210.0502].

[210] A. Mainzer, J. Bauer, R. M. Cutri, T. Grav, J. Masiero, R. Beck et al., *Initial Performance of the*

NEOWISE Reactivation Mission, *ApJ* **792** (Sept., 2014) 30, [`1406.6025`].

[211] J. R. Masiero, A. K. Mainzer, T. Grav, J. M. Bauer, R. M. Cutri, J. Dailey et al., *Main Belt Asteroids with WISE/NEOWISE. I. Preliminary Albedos and Diameters*, *ApJ* **741** (Nov., 2011) 68, [`1109.4096`].

[212] J. R. Masiero, A. K. Mainzer, T. Grav, J. M. Bauer and R. Jedicke, *Revising the Age for the Baptistina Asteroid Family Using WISE/NEOWISE Data*, *ApJ* **759** (Nov., 2012) 14, [`1209.1430`].

[213] C. R. Nugent, A. Mainzer, J. Masiero, J. Bauer, R. M. Cutri, T. Grav et al., *NEOWISE Reactivation Mission Year One: Preliminary Asteroid Diameters and Albedos*, *ApJ* **814** (Dec., 2015) 117, [`1509.02522`].

[214] B. A. Franz, W. T. Reach, T. Kelsall and J. L. Weiland, *Inversion of the DIRBE photometry to derive the three dimensional distribution of the interplanetary dust.*, in *American Institute of Physics Conference Series* (E. Dwek, ed.), vol. 348 of *American Institute of Physics Conference Series*, pp. 296–300, 1996.

[215] T. Kelsall, J. L. Weiland, B. A. Franz, W. T. Reach, R. G. Arendt, E. Dwek et al., *The COBE Diffuse Infrared Background Experiment Search for the Cosmic Infrared Background. II. Model of the Interplanetary Dust Cloud*, *ApJ* **508** (Nov., 1998) 44–73, [`astro-ph/9806250`].

[216] W. T. Reach, B. A. Franz and J. L. Weiland, *The Three-Dimensional Structure of the Zodiacal Dust Bands*, *Icarus* **127** (June, 1997) 461–484.

[217] F. E. DeMeo, R. P. Binzel and M. Lockhart, *Mars encounters cause fresh surfaces on some near-Earth asteroids*, *Icarus* **227** (Jan., 2014) 112–122, [`1309.4839`].

[218] F. E. DeMeo, R. P. Binzel, S. M. Slivan and S. J. Bus, *An extension of the Bus asteroid taxonomy into the near-infrared*, *Icarus* **202** (July, 2009) 160–180.

[219] T. Grav, A. K. Mainzer, J. M. Bauer, R. Cutri, J. Masiero, R. S. McMillan et al., *WISE Observations of the Jupiter Trojan Clouds*, in *AAS/Division for Planetary Sciences Meeting Abstracts #42*, vol. 42 of *Bulletin of the American Astronomical Society*, p. 1072, Oct., 2010.

[220] R. Gomes, H. F. Levison, K. Tsiganis and A. Morbidelli, *Origin of the cataclysmic Late Heavy Bombardment period of the terrestrial planets*, *Nature* **435** (May, 2005) 466–469.

[221] H. F. Levison, M. J. Duncan, L. Dones and B. J. Gladman, *The scattered disk as a source of Halley-type comets*, *Icarus* **184** (Oct., 2006) 619–633.

[222] J. Crovisier, D. Bockelée-Morvan, P. Colom, N. Biver, D. Despois, D. C. Lis et al., *The composition of ices in comet C/1995 O1 (Hale-Bopp) from radio spectroscopy. Further results and upper limits on undetected species*, *A&A* **418** (May, 2004) 1141–1157.

[223] M. J. Mumma and S. B. Charnley, *The Chemical Composition of Comets: Emerging Taxonomies and Natal Heritage*, *ARA&A* **49** (Sept., 2011) 471–524.

[224] T. Ootsubo, H. Kawakita, S. Hamada, H. Kobayashi, M. Yamaguchi, F. Usui et al., *AKARI Near-infrared Spectroscopic Survey for CO_2 in 18 Comets*, *ApJ* **752** (June, 2012) 15.

[225] N. Dello Russo, R. J. Vervack, H. Kawakita, H. Kobayashi, H. A. Weaver, W. M. Harris et al., *The volatile composition of 81P/Wild 2 from ground-based high-resolution infrared spectroscopy*, *Icarus* **238** (Aug., 2014) 125–136.

[226] D. Bockelée-Morvan, J. Crovisier, M. J. Mumma and H. A. Weaver, *The composition of cometary volatiles*, pp. 391–423. 2004.

[227] M. F. A'Hearn and P. D. Feldman, *Water vaporization on Ceres*, *Icarus* **98** (July, 1992) 54–60.

[228] M. F. A'Hearn, L. M. Feaga, H. U. Keller, H. Kawakita, D. L. Hampton, J. Kissel et al., *Cometary Volatiles and the Origin of Comets*, *ApJ* **758** (Oct., 2012) 29.

[229] W. T. Reach, M. S. Kelley and J. Vaubaillon, *Survey of cometary CO_2, CO, and particulate emissions using the Spitzer Space Telescope*, *Icarus* **226** (Sept., 2013) 777–797, [1306.2381].

[230] J. Pittichová, C. E. Woodward, M. S. Kelley and W. T. Reach, *Ground-Based Optical and Spitzer Infrared Imaging Observations of Comet 21P/GIACOBINI-ZINNER*, *AJ* **136** (Sept., 2008) 1127–1136, [0806.3582].

[231] P. Farinella and D. R. Davis, *Short-Period Comets: Primordial Bodies or Collisional Fragments?*, *Science* **273** (Aug., 1996) 938–941.

[232] S. A. Stern, *On the Collisional Environment, Accretion Time Scales, and Architecture of the Massive, Primordial Kuiper Belt.*, *AJ* **112** (Sept., 1996) 1203.

[233] D. Nesvorný, P. Jenniskens, H. F. Levison, W. F. Bottke, D. Vokrouhlický and M. Gounelle, *Cometary Origin of the Zodiacal Cloud and Carbonaceous Micrometeorites. Implications for Hot Debris Disks*, *ApJ* **713** (Apr., 2010) 816–836, [0909.4322].

[234] S. F. Dermott, K. Grogan, E. Holmes and S. Kortenkamp, *Dynamical structure of the Zodiacal cloud*, in *NATO Advanced Science Institutes (ASI) Series C* (J. M. Greenberg and A. Li, eds.), vol. 523 of *NATO Advanced Science Institutes (ASI) Series C*, p. 565, 1999.

[235] D. D. Durda and S. F. Dermott, *The Collisional Evolution of the Asteroid Belt and Its Contribution to the Zodiacal Cloud*, *Icarus* **130** (Nov., 1997) 140–164.

[236] J. C. Liou, S. F. Dermott and Y. L. Xu, *The contribution of cometary dust to the zodiacal cloud*, *Planet. Space Sci.* **43** (June, 1995) 717–722.

[237] M. Rowan-Robinson and B. May, *An improved model for the infrared emission from the zodiacal dust cloud: cometary, asteroidal and interstellar dust*, *MNRAS* **429** (Mar., 2013) 2894–2902, [1212.4759].

[238] J. S. Greaves and M. C. Wyatt, *Debris discs and comet populations around Sun-like stars: the Solar system in context*, *MNRAS* **404** (June, 2010) 1944–1951, [1001.5177].

[239] A. J. Espy, S. F. Dermott and T. J. J. Kehoe, *Dynamical Effects of Mars on Asteroidal Dust Particles*, *Earth Moon and Planets* **102** (June, 2008) 199–203.

[240] M. V. Sykes and P. D. Moynihan, *Asteroid Motions*, *Icarus* **124** (Dec., 1996) 399–406.

[241] M. V. Sykes, ed., *The Future of Solar System Exploration (2003-2013) – Community Contributions to the NRC Solar System Exploration Decadal Survey*, vol. 272 of *Astronomical Society of the Pacific Conference Series*, Aug., 2002.

[242] C. M. Lisse, C. H. Chen, M. C. Wyatt and A. Morlok, *Circumstellar Dust Created by Terrestrial Planet Formation in HD 113766*, *ApJ* **673** (Feb., 2008) 1106–1122, [0710.0839].

[243] R. G. Arendt, *DIRBE Comet Trails*, *AJ* **148** (Dec., 2014) 135, [1408.1466].

[244] L. Kresak and M. Kresakova, *The mass loss rates of periodic comets*, in *Diversity and Similarity of Comets* (E. J. Rolfe and B. Battrick, eds.), vol. 278 of *ESA Special Publication*, Sept., 1987.

[245] C. M. Lisse, M. F. A'Hearn, M. G. Hauser, T. Kelsall, D. J. Lien, S. H. Moseley et al., *Infrared Observations of Comets by COBE*, *ApJ* **496** (Mar., 1998) 971–991.

[246] D. Jewitt, H. Weaver, J. Agarwal, M. Mutchler and M. Drahus, *A recent disruption of the main-belt*

asteroid P/2010A2, *Nature* **467** (Oct., 2010) 817–819.

[247] W. T. Reach, J. Rho, A. Tappe, T. G. Pannuti, C. L. Brogan, E. B. Churchwell et al., *A Spitzer Space Telescope Infrared Survey of Supernova Remnants in the Inner Galaxy*, *AJ* **131** (Mar., 2006) 1479–1500, [astro-ph/0510630].

[248] J. Bock, I. Sullivan, T. Arai, J. Battle, A. Cooray, V. Hristov et al., *The Cosmic Infrared Background Experiment (CIBER): The Wide-field Imagers*, *ApJS* **207** (Aug., 2013) 32, [1206.4702].

[249] M. Küppers, L. O'Rourke, D. Bockelee-Morvan, J. Crovisier, B. Carry, D. Teyssier et al., *Search for Water Vapour Emission from DAWN target (1) Ceres with HERSCHEL*, in *European Planetary Science Congress 2012*, pp. EPSC2012–417, Sept., 2012.

[250] D. Takir, J. P. Emery, H. Y. McSween, C. A. Hibbitts, R. N. Clark, N. Pearson et al., *Nature and degree of aqueous alteration in CM and CI carbonaceous chondrites*, *Meteoritics and Planetary Science* **48** (Sept., 2013) 1618–1637.

[251] A. S. Rivkin, H. Campins, J. P. Emery, E. S. Howell, J. Licandro, D. Takir et al., *Astronomical Observations of Volatiles on Asteroids*, pp. 65–87. 2015.

[252] J. P. Gardner, J. C. Mather, M. Clampin, R. Doyon, M. A. Greenhouse, H. B. Hammel et al., *The James Webb Space Telescope*, *Space Sci. Rev.* **123** (Apr., 2006) 485–606, [astro-ph/0606175].

[253] R. A. Windhorst, N. P. Hathi, S. H. Cohen, R. A. Jansen, D. Kawata, S. P. Driver et al., *High resolution science with high redshift galaxies*, *Advances in Space Research* **41** (2008) 1965–1971, [astro-ph/0703171].

[254] J. P. Gardner, J. C. Mather, M. Clampin, R. Doyon, M. A. Greenhouse, H. B. Hammel et al., *The James Webb Space Telescope*, *Space Sci. Rev.* **123** (Apr., 2006) 485–606, [astro-ph/0606175].

[255] D. Kim, R. A. Jansen and R. A. Windhorst, *Analysis of the Intrinsic Mid-Infrared L-band to Visible–Near-Infrared Flux Ratios in Spectral Synthesis Models of Composite Stellar Populations*, *ArXiv e-prints* (Mar., 2016) , [1603.07764].

[256] J. S. Mulchaey, A. S. Wilson and Z. Tsvetanov, *An Emission-Line Imaging Survey of Early-Type Seyfert Galaxies. II. Implications for Unified Schemes*, *ApJ* **467** (Aug., 1996) 197.

[257] H. Ebeling, A. C. Edge, H. Bohringer, S. W. Allen, C. S. Crawford, A. C. Fabian et al., *The ROSAT Brightest Cluster Sample - I. The compilation of the sample and the cluster log N-log S distribution*, *MNRAS* **301** (Dec., 1998) 881–914, [astro-ph/9812394].

[258] M. Mechtley, R. A. Windhorst, R. E. Ryan, G. Schneider, S. H. Cohen, R. A. Jansen et al., *Near-infrared Imaging of a z = 6.42 Quasar Host Galaxy with the Hubble Space Telescope Wide Field Camera 3*, *ApJ* **756** (Sept., 2012) L38, [1207.3283].

[259] M. Mechtley, K. Jahnke, R. A. Windhorst, R. Andrae, M. Cisternas, S. H. Cohen et al., *Do the Most Massive Black Holes at z = 2 Grow via Major Mergers?*, *ArXiv e-prints* (Oct., 2015) , [1510.08461].

[260] J. Wang, G. Kauffmann, R. Overzier, B. Catinella, D. Schiminovich, T. M. Heckman et al., *The GALEX Arecibo SDSS survey - III. Evidence for the inside-out formation of Galactic discs*, *MNRAS* **412** (Apr., 2011) 1081–1097, [1011.0829].

[261] J. Magorrian et al., *The Demography of massive dark objects in galaxy centers*, *Astron. J.* **115** (1998) 2285, [astro-ph/9708072].

[262] R. J. Bouwens, G. D. Illingworth, P. A. Oesch, M. Trenti, I. Labbé, L. Bradley et al., *UV Luminosity Functions at Redshifts z ∼ 4 to z ∼ 10: 10,000 Galaxies from HST Legacy Fields*, *ApJ* **803** (Apr.,

2015) 34, [`1403.4295`].

[263] P. A. Oesch, R. J. Bouwens, G. D. Illingworth, M. Franx, S. M. Ammons, P. G. van Dokkum et al., *First Frontier Field Constraints on the Cosmic Star-Formation Rate Density at z∼10 - The Impact of Lensing Shear on Completeness of High-Redshift Galaxy Samples*, *Astrophys. J.* **808** (2015) 104, [`1409.1228`].

[264] H. Yan and R. A. Windhorst, *Candidates of z ˜= 5.5-7 Galaxies in the Hubble Space Telescope Ultra Deep Field*, *ApJ* **612** (Sept., 2004) L93–L96, [`astro-ph/0407493`].

[265] R. J. Morgan, R. A. Windhorst, E. Scannapieco and R. J. Thacker, *"Observing and Analyzing" Images from a Simulated High-Redshift Universe*, *PASP* **127** (Sept., 2015) 803–824, [`1507.07538`].

[266] D. Spergel et al., *Wide-Field InfrarRed Survey Telescope-Astrophysics Focused Telescope Assets WFIRST-AFTA 2015 Report*, `1503.03757`.

[267] EUCLID collaboration, R. Laureijs et al., *Euclid Definition Study Report*, `1110.3193`.

[268] Convener: J. Newman collaboration, J. A. Newman et al., *Spectroscopic needs for imaging dark energy experiments*, *Astropart. Phys.* **63** (2015) 81–100.

[269] D. Kirk et al., *Galaxy alignments: Observations and impact on cosmology*, *Space Sci. Rev.* **193** (2015) 139–211, [`1504.05465`].

[270] A. Kiessling et al., *Galaxy Alignments: Theory, Modelling & Simulations*, *Space Sci. Rev.* **193** (2015) 67–136, [`1504.05546`].

[271] B. Joachimi et al., *Galaxy alignments: An overview*, *Space Sci. Rev.* **193** (2015) 1–65, [`1504.05456`].

[272] E. Krause, T. Eifler and J. Blazek, *The impact of intrinsic alignment on current and future cosmic shear surveys*, *Mon. Not. Roy. Astron. Soc.* **456** (2016) 207–222, [`1506.08730`].

[273] Z. Ivezic, J. A. Tyson, B. Abel, E. Acosta, R. Allsman, Y. AlSayyad et al., *LSST: from Science Drivers to Reference Design and Anticipated Data Products*, *ArXiv e-prints* (May, 2008) , [`0805.2366`].

[274] M. Jurić, J. Kantor, K. Lim, R. H. Lupton, G. Dubois-Felsmann, T. Jenness et al., *The LSST Data Management System*, *ArXiv e-prints* (Dec., 2015) , [`1512.07914`].

[275] J. A. Newman, *Calibrating Redshift Distributions beyond Spectroscopic Limits with Cross-Correlations*, *ApJ* **684** (Sept., 2008) 88–101, [`0805.1409`].

[276] M. Rahman, B. Ménard, R. Scranton, S. J. Schmidt and C. B. Morrison, *Clustering-based redshift estimation: comparison to spectroscopic redshifts*, *MNRAS* **447** (Mar., 2015) 3500–3511, [`1407.7860`].

[277] G. Torres, J. Andersen and A. Giménez, *Accurate masses and radii of normal stars: modern results and applications*, *A&A Rev.* **18** (Feb., 2010) 67–126, [`0908.2624`].

[278] A. W. Mann, G. A. Feiden, E. Gaidos, T. Boyajian and K. von Braun, *How to Constrain Your M Dwarf: Measuring Effective Temperature, Bolometric Luminosity, Mass, and Radius*, *ApJ* **804** (May, 2015) 64, [`1501.01635`].

[279] P. W. Sullivan, J. N. Winn, Z. K. Berta-Thompson, D. Charbonneau, D. Deming, C. D. Dressing et al., *The Transiting Exoplanet Survey Satellite: Simulations of Planet Detections and Astrophysical False Positives*, *ApJ* **809** (Aug., 2015) 77, [`1506.03845`].